Photoacoustic Imaging in Acoustically Heterogeneous Media

Hans-Martin Schwab

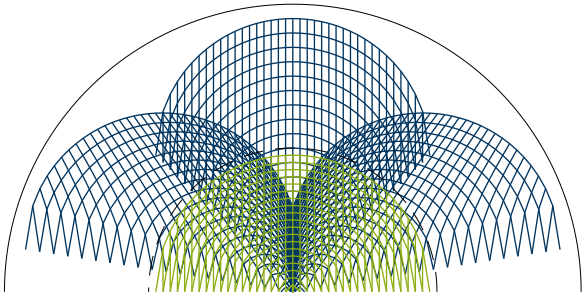

Photoacoustic Imaging in Acoustically Heterogeneous Media

Dissertation

zur Erlangung des Grades eines
Doktor-Ingenieurs
der
Fakultät für Elektrotechnik und Informationstechnik
an der Ruhr-Universität Bochum

Hans-Martin Schwab
Bayreuth

Bochum, 2019

Berichter:	Prof. Dr.-Ing. Georg Schmitz
	Prof. Dr. rer. nat. Martin R. Hofmann
Mündliche Prüfung:	11. Oktober 2018

To my father

Acknowledgments

This thesis is the result of my research at the chair for Medical Engineering at the Ruhr-University Bochum. I would like to express my graditude to my adviser Prof. Georg Schmitz. His intellect and reasoning have always inspired me. I enjoyed our long and thorough discussions just as much as the amiable times at project meetings and conferences in which we participated. I also thank Prof. Martin Hofmann for co-revising this dissertation and for the easy access to tools and instruments from his laboratories.

Moreover, I would like to thank all my current and former coworkers in our research group. It was a great pleasure to work, eat, travel and laugh with all of you! I am glad for having made so many friends and I will always remember our conferences and vacations together. Special thanks are owed to my long-term project partner Martin Beckmann, who introduced me to the exciting field of photoacoustics and who always took the time to discuss any matters with me. I also thank the whole Fullphase/CVENT consortium for a productive and enjoyable cooperation and the wonderful times at the project meetings.

Beyond that, I am really grateful for my friends in Bochum and from my hometown. From long nights to hilarious Whats-app conversations they provided great distractions from the stressful time, in which this thesis was developed. Special thanks go out to my family, especially my parents, who have always been very supportive and who have guided and accompanied me with

enthusiasm and dedication. Finally, I express my deepest gratitude to my wife Catherine, who was my strongest moral support during the writing process, for all her efforts to lift me up and for all her encouragement during all four years of my PhD.

Abstract

As a relatively new imaging modality, photoacoustic imaging is on the verge of being established as a clinical diagnosis tool. One promising application is the characterization of atherosclerotic plaques to identify an optimal treatment. While sound-scattering medium heterogeneities of biological tissues are the foundation of ultrasound imaging, the same kinds of tissues are usually assumed to be acoustically homogeneous in photoacoustic imaging. Ignoring these heterogeneities in a photoacoustic reconstruction causes artifacts. In this dissertation, a model based reconstruction algorithm is introduced that considers acoustic scattering. The method returns accurate results but also requires exact background information. In the progress of the dissertation, artifacts associated with heterogeneous media are classified as either aberration artifacts, which blur the image and are caused by refraction, or as clutter artifacts, which appear as disturbing structures in the image and are caused by reflection. A reconstruction algorithm based on a paraxial wave propagation model is introduced that compensates for aberration artifacts. The algorithm requires knowledge about the underlying heterogeneity distribution, but it is shown that imperfect heterogeneity data derived from reflection mode ultrasound imaging are sufficient. To address the suppression of clutter, a third algorithm is introduced, which derives information about the heterogeneities directly from reflection mode ultrasound measurements. Combining the two methods results in a powerful and yet computationally efficient reconstruction.

Contents

List of Figures

List of Tables

Nomenclature

Abbreviations

Shortcut	Description
PA	photoacoustic
US	ultrasound
SOS	speed of sound
Nd:YAG	Neodymium-doped yttrium aluminum garnet
Q-switch	quality factor switch
SNR	signal to noise ratio
FWHM	full width half maximum
PED	photoacoustics enabling device
OPO	optical parametric oscillator
LED	light emitting diode
SNR	signal-to-noise ration
DAS	delay and sum
UBP	universal back propagation
FFT	fast Fourier transform
FSAFT	Fourier synthetic aperture focusing technique
NUFFT	non-uniform fast Fourier transform

Shortcut	Description
IVUS	intra-vascular ultrasound
OCT	optical coherence tomography
MRI	magnetic resonance imaging
CT	computed tomography
DCA	displacement compensated averaging
LOVIT	localized vibration tagging
PAFUSion	photoacoustic-guided focussed ultrasound
FWHM	full width at half maximum
PSNR	peak signal-to-noise ratio
ROI	region of interest
PBP	paraxial back propagation
iDAS	individual delay and sum
EIMI	European Institute for Molecular Imaging
CUTE	computed ultrasound tomography in echo-mode
PW	plane wave
PWUS	plane wave ultrasound
PAUS	photoacoustic and ultrasound

Symbols

Symbol	Description
μ_s	scattering coefficient
$\mu_s^{'}$	reduced scattering coefficient
n_s	volumetric scatterer density
σ_s	scattering cross section
g	anisotropy factor
μ_a	absorption coefficient
n_s	volumetric absorber density
σ_s	absorption cross section
I	light intensity
μ_{eff}	effective attenuation coefficient
τ_{th}	thermal relaxation time
α_{th}	diffusivity
H	heating function

Symbol	Description
η	normalized laser power
p_0	initial pressure distribution
Γ	Grüneisen coefficient
β	coefficient for volume expansion
c	speed of sound
C	heat capacity
$\boldsymbol{u}$	particle displacement
p	acoustic pressure
κ	compressibility
ρ	mass density
T	temperature
γ_ρ	mass density variation
γ_κ	compressibility variation
g	Green function
g_0	free-field Green function
p_m	measured acoustic pressure
$k_{z,x,t}$	wave number
$\kappa_{z,t}$	artificial wave number
q	photoacoustic source term
V_γ	scatter operator
$\Box$	homogeneous wave operator
$\Box_\gamma$	heterogeneous wave operator
g_γ	full-wave Green function for heterog. media
p_h	pressure field without scattering
p_{sc}	scattered pressure field
G_0	Green function operator
Ω	half-space
Ω'	solution domain
R	photoacoustic measurement operator
L^2	space of square-integrable functions
α	relaxation parameter
Z	auxiliary “pressure-like” field
H_W	Wiener deconvolution filter
$P_{s,n}$	spectral signal/noise density
e	normalized reconstruction error

Symbol	Description
γ_c	speed-of-sound variation
u	envelope transform of pressure
$T^{+/-}$	transmission factor in positive/negative direction
p_{in}	incoming wave
$\eta_{us,pa}$	ultrasound/photoacoustic impulse response
ϑ	angle of incoming wave
G_{BP}	back propagation operator
$\mathscr{C}$	conjugate operator
w	linear interpolation weight
f_s	temporal sampling frequency
γ	general scatterer distribution

1 Introduction

Photoacoustic (PA) imaging takes advantage of the photoacoustic effect for the visualization of optical object properties by the detection of acoustic waves. Alexander Graham Bell was the first person to report the photoacoustic effect in 1881, when he observed the generation of sound during the modulated exposure of a metal plate to direct sun light [25].

If an optically absorbing object is exposed to temporally varying light intensities, the absorption forces an expansion, depending on the thermal properties of the object and the expansion is followed by a compression after the exposure. This deformation is passed to the surrounding medium and propagates as an acoustic wave, where the amplitude of the wave reflects the optical absorption properties of the object.

In the last decades, photoacoustic imaging has evolved as one of the fastest developing imaging techniques in biomedical imaging, with various applications and techniques [110]. The huge interest in this modality is usually explained by the fact that photoacoustic imaging manages to comprise the benefits of optical imaging in terms of image contrast and the benefits of ultrasound imaging in terms of penetration depth [119, 125].

Overviews about modern photoacoustic setups, methods and algorithms can be found in [19, 92, 177, 178, 186]. Clinical applications range over a large set of disciplines, such as oncology [52, 61, 72, 106, 123, 166], rheumatology [117, 175, 184], ophthalmology [39, 113, 197], dermatology [56, 135, 140] and, on a preclinical level, neurology [66, 112, 189]. In this dissertation, another application will be addressed that has recently drawn a strong interest in PA

research: the detection and classification of arteriosclerosis in the carotid artery [12, 50, 104]. Exploiting the spectroscopic property of PA imaging by applying different laser wavelengths for excitation, there is a high potential of determining compositions of atherosclerotic plaques, which is believed to provide evident information about the probability of plaque to rupture and to cause severe brain damage [65]. A major challenge of carotid artery imaging is the required penetration depth [12, 50, 104]. Besides hardware based system optimization, very accurate reconstruction algorithms are substantial to achieve this goal.

PA imaging is often described as a modality that benefits from the low impact of ultrasound scattering. This assumption is usually taken as axiomatic and most standard reconstruction algorithms assume constant acoustic properties [16, 33, 101, 185]. Compared to pure optical methods, which definitely suffer from diffuse scattering more than ultrasound generated by the PA effect, this assumption might be correct. Ultrasound scattering is reported to be up to three orders of magnitude weaker than optical scattering [186, p. 2]. However, in the light of ultrasound imaging being a modality that intrinsically depends on the presence of acoustic heterogeneities in biological tissue and which particularly images these heterogeneities, the question arises, if the neglection of acoustic scattering in PA imaging is always justified.

Most of the image distortions and artifacts related to acoustically heterogeneous media using a linear array PA systems can be classified as “clutter”, reflection artifacts, and as “aberration”, or refraction artifacts. Clutter, or backscatter artifacts, arise from PA waves that propagate into the tissue and are back-reflected by acoustic heterogeneities. The skin is a crucial source of clutter as the light intensity at the skin surface is very strong and, simultaneously, the absorption in skin is usually higher than for most other tissues [73, 143]. Adjacent to clutter, aberrations are artifacts associated with wave refraction during the transmission of PA waves through acoustic heterogeneities towards the sensor. This process can be assigned to variations in the speed of sound (SOS), which cause wave front distortions. As a result, the structures in the PA reconstruction are misplaced and deformed [44, 182].

The main goal of this thesis is to establish a thorough understanding of the physical processes related to artifacts that are caused by acoustically heterogeneous media in PA imaging and to introduce novel methods to reduce them. This can also be viewed as the task to consider the acoustic medium properties in the forward imaging model in order to account for these properties during the inversion of the model. All considerations in this dissertation refer to applications using linear array sensors. While PA imaging in full-view systems

with a sensor area enclosing the imaged object have already been investigated (see [10] for an overview), the impact of heterogeneities for linear arrays have barely been addressed, even though most clinical applications require a setup in reflection mode using linear arrays. The drawback of linear arrays compared to a full-view sensor lies in the fact that the inversion is always associated with an ill-posed problem due to a mathematically incomplete measurement data set. Methods like time reversal [76–78] or half-time integration [11], which are often employed for full-view inversions in heterogeneous media, do not return exact results.

Besides the aim to conquer the issue of reconstruction in heterogeneous media by employing an accurate wave model, an engineering-orientated view will be taken on the topic in terms of applicability to actual imaging systems that can operate in real time and do not provide any a-priori knowledge about the heterogeneities. The problem of heterogeneous media is divided into the main causes that actually harm image quality, which are clutter and aberrations. Dedicated methods to account for the individual problems are introduced that are designed to be accurate enough to account for the respective source of problem but are still simple enough to be implemented in fast algorithms.

The dissertation is organized as follows: Chapter 2 introduces into the physical basics of the photoacoustic effect and common imaging methods. Also, state-of-the-art photoacoustic reconstruction methods in homogeneous media are presented. In addition, the topic of atherosclerotic diseases is stressed as a high impact application that will be dealt with throughout the dissertation and to which most experiments and simulations refer. While chapter 2 only discusses reconstruction algorithms that assume acoustically homogeneous media, chapter 3 addresses the impact of acoustically heterogeneous propagation media by a physical description of several PA wave propagation models in the presence of scattering potentials. Based on a literature research, the two major impacts of the acoustic heterogeneities, which are clutter and aberrations are identified. Prior approaches in literature that address these causes of artifacts are discussed. In chapter 4, a novel full wave inversion for PA measurements in heterogeneous media is introduced. Afterwards, the advantages and disadvantages of a full wave inversion are discussed and two approaches to account for specific artifacts of heterogeneous media in PA imaging are presented, one for clutter and one for aberrations. Artifacts that are associated with aberrations are discussed in chapter 5 and a novel approach is introduced to account for speed-of-sound variations in the medium during back propagation in an efficient way, which is based on a paraxial wave propagation. The method is applied to simulation data and experimental data and its accuracy compared

to conventional methods is discussed. A dedicated in-plane clutter reduction is derived in chapter 6 as a numeric least-squares solution to the inversion of a scatter model. Also, a simplified scatter estimation and subtraction method is introduced. The performance of the clutter reduction approach is assessed for both simulation data and experimental data and approaches to reduce the computation time and to broaden the range of applicability are presented. Finally, all results are summarized in chapter 7 and explicit conclusions are drawn.

2

Fundamental Photoacoustic Imaging Principles

Generally speaking, the photoacoustic (PA) effect, or thermoacoustic effect, describes the generation of an acoustic wave during the thermo-elastic expansion of matter due to the absorption of modulated electromagnetic radiation. The photoacoustic effect was discovered by Alexander Graham Bell in 1880 [25]. Bell observed that chopped sunlight generates sound waves when being directed at optically absorbing materials. The first applications were in the field of communication, where he used the PA effect to transmit voice wirelessly [119]. After a long period with few publications in that topic, Veingerov revived photoacoustic research in 1946 [176], when he determined the composition of gases using the PA effect. The first time photoacoustics were exploited for imaging was in 1994, when Kruger et al. [103] located the sources of PA waves in a volume containing a lipid emulsion. Apart from thermo-elastic expansion, other processes can also generate acoustic waves in response to electromagnetic exposure, such as radiation force, vaporization and material ablation [157]. However, since these effects play a minor role in PA imaging [20, 157], they are neglected here.

In clinical PA imaging, the photoacoustic effect is employed to create tomographic images of biological tissue by detecting an ultrasound wave that is excited by the irradiation of pulsed, or sometimes modulated, laser light. While irradiating the tissue, the light is scattered and absorbed. Due to diffuse scattering in the tissue, the light is distributed throughout the image area. If

the light is absorbed by certain tissue components, the instantaneous heating due to absorption forces an expansion of the absorbing component, according to its thermo-elastic properties. This expansion leads to a local pressure rise, the PA source, which initiates an acoustic wave. The amplitude of the acoustic source is directly connected to the light intensity, the thermo-elastic properties of the medium and the absorption coefficient of the absorbing component. Detecting the sound wave as a function of time at multiple positions at the surface of the observed tissue produces a set of measurement data that contains information about the source distribution. The aim of photoacoustic imaging is to retrieve the source distribution by finding an inverse description of this measurement process.

In this chapter, the physical basics of optical light propagation, thermo-elastic expansion and photoacoustic wave propagation are introduced, followed by a discussion on the number of dimensions required for simulations and reconstructions in photoacoustic imaging with linear arrays. Then, an introduction into photoacoustic imaging principles and an overview of common systems are given. In the end of the chapter, atherosclerosis in the carotid artery is presented as a high impact application that will be dealt with throughout this dissertation and the high potential of PA imaging in this field is emphasized.

2.1 The Photoacoustic Effect and Wave Propagation

The process of converting radiation into mechanical waves is referred to as thermo-elastic energy conversion. Besides the possibility of employing microwaves in the field of thermo-acoustics, the most common radiation is within the visible or infrared light spectrum. This dissertation deals with pulsed laser light emission in the near infrared range, as it is most applicable for imaging biological tissue. Especially in the range between 700 nm and 900 nm, light can penetrate deeply into the tissue. This wavelength range is also referred to as the optical window of biological tissue [186]. On exposure to pulsed laser light, biological tissue generates sound waves by the photoacoustic effect, whose strength depends on the absorption properties of the respective tissue components. This chapter will briefly address the optical path but will focus on the acoustic part as it is more relevant for this dissertation. A more detailed explanation of all involved optical processes can be found in [20].

2.1.1 Relevant Optical Processes

Photoacoustic imaging can generally be divided into a purely optical part describing the light generation, light propagation and absorption that generates a temperature increase, and a purely acoustic part that consists of instant acoustic sources due to the temperature rise generating acoustic waves, which can be detected. This section deals with the optical part. The light propagation is mainly determined by the tissue dependent scattering and absorption properties, where scattering is the dominant process. In biological tissue, the mean free path length for scattering of infrared light is in the order of 0.1 mm, while the mean free path length for absorption can reach up to 10-100 mm [178, p.2]. Absorption, however, is the relevant process for the photoacoustic effect as it characterizes the amount of converted optical energy.

Light Generation One main characteristic of a photoacoustic imaging system is the employed source of light. To convert optical energy into acoustic energy via thermo-elastic expansion, the absorbed light is required to exhibit a temporally varying intensity. Due to a low energy conversion efficiency of the photoacoustic effect, a high light power is required to attain a sufficient signal-to-noise ratio (SNR) of the detected acoustic signal. As a suitable solution to produce high intensity modulated light, pulsed lasers are the most common light source in PA imaging. Other light sources that produce light of modulated intensity are less common, but have also been employed [6, 53, 138, 148]. Besides pulsed light, chirps have also been applied in combination with pulse compression techniques to obtain a certain bandwidth, providing a spatial resolution in the image [53, 138, 169]. However, short light pulses with a high ratio of the generated acoustic signal amplitude to the applied optical energy are most promising for biomedical applications. Therefore, this dissertation focuses on pulsed lasers for light excitation.

Lasers are a special class of light sources that are mainly distinguished from other light sources in their monochromacity, coherence length, beam quality or intensity [97]. A basic laser setup consists of a coherent optical amplifier that is embedded into an optical resonator. In the optical amplifier, atoms are excited by the absorption of light. Besides absorption, two other major interactions between atoms and photons exist, which are spontaneous emission and stimulated emission. In case of a population inversion, which occurs when the amount of excited atoms exceeds the amount of unexcited atoms, stimulated emission becomes the dominant effect over absorption and the medium acts as an amplifier. To achieve population inversion, external

energy needs to be deposited, which is called pumping. Common pumping sources are other lasers, gas discharges or flash lamps. The optical resonator stabilizes the laser light in terms of monochromacity and coherence. In the simple case of a Fabry Perot Etatlon, it consists of two mirrors, between which one specific mode can create a standing wave [125, 146].

Common laser sources for PA imaging are solid state lasers, such as Q-switched Nd:Yag lasers, which exhibit pulse energies of several joules at pulse durations in the range of 5 ns [20, p.45]. However, Nd:Yag lasers operate at a fixed wavelength of 1064 nm, which does not allow for spectral PA imaging. For that reason they are often combined with optical parametric oscillators (OPO). An OPO consists of an optically nonlinear crystal, which is embedded into an optical resonator and can be seen as a laser system that is pumped by another laser. Once the pump beam illuminates the nonlinear crystal, it interacts with random fluctuations (quantum noise) of two other wavelengths that are amplified by the resonator. The wavelengths of the generated light beams can be tuned by the orientation of the nonlinear crystal within the resonator [125, p.39f]. Besides Nd:Yag lasers, other laser sources have been employed for photoacoustic imaging. Ti:Sapphire lasers [136, 161], for example, exhibit a low conversion efficiency but have the advantage to be tunable in the range of 700-1050 nm. Alexandrite lasers [52], moreover, are also tunable in a certain wavelength range and can be Q-switched to produce pulses of equal energy as Q-switched Nd:Yag lasers. The largest spectral range can be achieved by dye lasers, which have also been employed for PA imaging [180, 195]. However, the specific dyes only cover a small range of wavelengths and need to be exchanged to sweep through a larger spectral range [125].

Semiconductor lasers have recently been established as a cost and space efficient alternative to the above mentioned lasers. In a semiconductor, light is emitted when electrons in the conduction band recombine with holes in the valence band. Even though semiconductor lasers cannot generally be tuned over large wavelength ranges, their compactness and low costs allow for the possibility to combine several laser diodes of different wavelengths. While, initially, the pulse energy ranged within a few microjoules [58, p.25], recent developments show that pulse energies beyond 1 mJ are actually feasible [36, 37]. In combination with very high pulse repetition frequencies that can be attained, high amounts of light energy can be delivered in a short time and the results of multiple pulses can be averaged. Even though, in terms of laser safety regulations, it is more eligible to apply a small number of high energetic pulses than to apply many low energetic pulses, diode lasers can be employed for PA imaging even in vivo [100]. Another advantage of the

use of laser diodes is the ability to simultaneously apply multiple wavelengths, which, in combination with coding strategies, can be exploited to increase the signal-to-noise ratio (SNR) [21, 22, 24].

Recently, the use of light emitting diodes (LED) has been investigated in the context of PA imaging [1–4]. While LEDs exhibit even lower pulse energies than semiconductor lasers, they are even more cost efficient and can easily be combined in LED arrays, which allows for a large illumination surface. This concept has already been integrated in a commercial PA system by PreXion [1].

In most PA systems, the light is delivered to the tissue surface by optical wave guides. In the case of laser diodes or LEDs, the light source can also directly be attached to the skin [1], or can be integrated in the ultrasound transducer [36]. The general aim in the design of the optical path is to maximize the amount of light delivered into the tissue, which depends on many factors, such as the angle of incidence, optical refractive index of the optical components, the illuminated area and distance to the image plane. The influence of such factors has been investigated in [20].

Scattering While the light beam irradiates the tissue, it undergoes strong scattering. On the one hand, this is beneficial in terms of distributing the light all over the image area. On the other hand, strong scattering causes light to be scattered out of the image plane. In most biological tissues, scattering is the most dominant effect. The mean free path length is in the order of 0.1 mm. The strongest scattering appears for structures of a size in the order of the wavelength that have a strong mismatch in refractive index to the background. The average refractive index varies between 1.34 to 1.62. The most exact description of the scattering behavior of a spherical particle is provided by Mie theory. However, for particles sizes that are significantly smaller than the wavelength, Rayleigh theory becomes very accurate [178, p.17ff].

The most common quantity to describe the scattering behavior of a material is the scattering coefficient μ_s, which is usually expressed in 1/cm. It can be seen as total scatter cross sectional area per unit volume and relates to the scattering cross section σ_s by [178]:

$$\mu_s = n_s \sigma_s, \tag{2.1.1}$$

where n_S is the volumetric scatterer density. Generally, μ_s only quantifies the probability for a scattering event for a certain traveling distance, but does not take into account the propagation direction. Hence, it is not sufficient to estimate the scattering over depth, especially because scattering in biological

tissue is not isotropic in general. Hence, for rough estimations and light simulations, the reduced scatter coefficient μ_s' is usually employed, which provides the probability of a scattering event over depth by reducing the scatter coefficient by an anisotropy factor g, which is also material dependent [20]:

$$\mu_s' = \mu_s(1-g). \tag{2.1.2}$$

The anisotropy factor takes into account the material's scattering directivity and is negative, if back scattering is the dominant process, and positive, if forward scattering is the dominant process. If g equals 0, the scattering is isotropic and the reduced scattering coefficient equals the scattering coefficient. For biological tissue in the near infrared region, typical values for $\mu_s$are around $100\,\mathrm{cm}^{-1}$ and g is around 0.9 [186].

Absorption Apart from scattering, light incident on matter can also be absorbed, which means the light energy is transferred to other kinds of energy such as thermal energy. While optical absorption is indispensable to generate photoacoustic waves, strong absorption in the upper tissue layers is not desired, because it can attenuate the light too much, such that lower structures are not exposed to sufficient amounts of light.

The absorption quality of a certain material is usually quantified by the absorption coefficient μ_a, which reflects the probability of photon absorption per unit path lengths and can be referred to the particle's cross section for absorption σ_a by [178, p.5]:

$$\mu_a = n_a\sigma_a, \tag{2.1.3}$$

where n_a is the absorber density.

When light passes through absorbing material, it is attenuated and the light intensity decreases with depth. The intensity profile over depth $I(z)$ is usually described by Beer's law [178, p.5]:

$$I(z) = I_0\exp(-\mu_a z), \tag{2.1.4}$$

where I_0 is the initial intensity at $z=0$ and μ_a is assumed constant within $[0,z]$. If the material is both scattering and absorbing, the intensity decays with the effective attenuation coefficient μ_{eff}. A common approximation for the effective attenuation coefficient in biological tissue is given by [162]:

$$\mu_{eff} = \sqrt{3\mu_a(\mu_a+\mu_s')} \tag{2.1.5}$$

and can be derived by diffusion theory. Replacing μ_a by μ_{eff} in 2.1.4 yields an appropriate estimation of the light attenuation over depths in a homogeneous medium.

So far it has been neglected that both μ_a and μ_s' are actually functions of the wavelength λ. The wavelength dependence of the absorption coefficient can be exploited to characterize the tissue in multispectral PA imaging. However, the pressure generated by the photoacoustic effect depends on two factors, the absorption coefficient and the light intensity. The light intensity might be estimated based on general tissue properties, but these can vary strongly between different individuals, different locations in the body and even over time [18, 84]. Nevertheless, quantitative imaging and tissue characterization are popular topics in PA research [193]. The most common approach is the determination of blood oxygenation, which is feasible due to the strong variations of the absorption spectrum of blood at different oxygenation levels. Oxygenation is of high importance in diagnostics, for example in oncology, because it reflects the metabolic state of lesions [59, 107, 186].

The mean free path length for absorption in biological tissue in the near infrared region is about 10-100 mm and thus, absorption is generally less likely than scattering. The strongest absorbers are hemoglobin, melanin and, with increasing wavelengths, water [178].

2.1.2 Thermo-Elastic Energy Conversion

As mentioned before, absorption is the key interaction for photoacoustic energy conversion. Absorbed light is converted into acoustic energy by thermo-elastic expansion, which is elaborated in this chapter. For the following relations to hold, two conditions regarding the light pulse lengths must be met, thermal confinement and stress confinement. The entire physical model used in this dissertation relies on short light pulses that are within thermal confinement and stress confinement.

Thermal confinement requires the pulse length to be distinctly smaller than the thermal relaxation time τ_{th}, which quantifies the thermal diffusion process:

$$\tau_{th} = \frac{d_c^2}{\alpha_{th}}, \tag{2.1.6}$$

where d_c is the characteristic size of the heated region in m and α_{th} is the thermal diffusivity in $\frac{m^2}{s}$. Stress confinement, on the other hand, requires the light pulse lengths to be distinctly smaller than the respective stress relaxation

time τ_s, which quantifies the pressure propagation and is given by:

$$\tau_s = \frac{d_c}{c_0} \tag{2.1.7}$$

with c_0 as speed of sound of the heated region. In principle, PA imaging is also feasible with longer light exposure, if the light intensity varies, as described in section 2.1.1, but for this, more complex thermodynamic processes need to be considered in the imaging model. If the light pulse length is significantly smaller than the thermal and stress relaxation time, the absorption of light causes an instantaneous heating. The amount of light energy that is converted into heat is characterized by the heating function $H(\boldsymbol{r}, t)$ in $\frac{J}{m^d s}$, where $\boldsymbol{r}$ is the spatial coordinate in a generally d-dimensional space and t is the temporal coordinate. The heating function can also be described as absorbed energy density and is dependent on the optical properties of the tissue by

$$H(\boldsymbol{r}, t) = \mu_a(\boldsymbol{r}) I(\boldsymbol{r}, t). \tag{2.1.8}$$

This becomes obvious considering that the energy that is gained by absorption is exactly the energy that the light radiation loses. For a plane light wave, the absorbed energy density can be seen as the negative spatial derivative of the light intensity in z-direction:

$$H = -\partial_z I = \mu_a I_0 \exp(-\mu_a z) = \mu_a I. \tag{2.1.9}$$

Since the speed of light is several orders of magnitudes higher than the speed of sound, the optical propagation occurs on time scales that are irrelevant for the acoustic propagation. Thus, the light distribution is usually assumed instantaneous and the light intensity $I(\boldsymbol{r}, t)$ can be separated into a spatial part $I_r(\boldsymbol{r})$ and a temporal part $\eta(t)$:

$$I(\boldsymbol{r}, t) = I_r(\boldsymbol{r}) \eta(t) \tag{2.1.10}$$

with $\int \eta dt = 1$, such as in [177, p.29]. As $\eta(t)$ describes a pulse it also vanishes for $t < 0$ and after a finite value T_p, such that $\eta(t) = 0$, $t \notin [0, T_p]$. The heating function can likewise be separated:

$$H(\boldsymbol{r}, t) = H_r(\boldsymbol{r}) \eta(t). \tag{2.1.11}$$

For infinitely short laser pulses, the heating function can be modeled as $\eta(t) = \delta(t)$ with δ being the delta distribution. In that case, the heating function is directly proportional to an instantaneous pressure increase, which is also

referred to as initial pressure distribution p_0 and is the quantity of interest in PA imaging [181, p.311]:

$$p_0(\boldsymbol{r}) = \Gamma H_r(\boldsymbol{r}). \tag{2.1.12}$$

The proportionality coefficient Γ is called Grüneisen parameter and is defined as:

$$\Gamma = \frac{\beta c_0^2}{C} \tag{2.1.13}$$

with β being the coefficient for thermal volume expansion, c_0 being the background speed of sound and C being the heat capacity . The Grüneisen parameter, in general, also depends on space, which further complicates quantitative imaging of μ_a. However, in contrast to the other tissue properties, Γ is also temperature dependent. This fact has been exploited in several setups for tissue characterization [155, 170, 171].

In summary, the instant pressure rise due to the absorption of short light pulses can be related to the light properties and the tissue properties by:

$$\boxed{p_0(\boldsymbol{r}) = \Gamma \mu_a(\boldsymbol{r}) I_r(\boldsymbol{r})}$$

With a given initial pressure distribution $p_0(\boldsymbol{r})$, the entire model reduces to a completely acoustic model. Hence, if quantitative imaging of the actual tissue parameters is not aimed for, the issue of reconstruction is an entirely acoustic inverse problem that aims for retrieving an initial value to the pressure wavefield that is characterized by $p_0(\boldsymbol{r})$.

2.1.3 The Photoacoustic Wave Equation

This chapter aims for the derivation of a very general photoacoustic wave equation considering various wave properties. However, an exhaustive description of all involved processes will not be given. Only wave properties that play a role in this dissertation will be taken into account. Therefore, the acoustic medium properties are reduced to heterogeneous scattering potentials. Acoustic attenuation is not considered, which can be justified by the limited penetration depth of PA imaging and, apart from small animal imaging applications, by relatively low acoustic frequencies. Also, visco-elastic effects and nonlinear sound propagation will not be considered, such that the wavefield can be expressed by the scalar pressure and linearized differential equations can be used. The neglection of attenuation, nonlinear sound propagation and viscosity are also discussed in [177, p.28].

The photoacoustic wave equation originates in two first order differential equations. The first one is the linear invicid force equation, which is also refereed to as Euler equation and reflects a conservation of momentum [178, p.288]:

$$\partial_{tt}\boldsymbol{u}(\boldsymbol{r},t) = -\rho(\boldsymbol{r})^{-1}\nabla p(\boldsymbol{r},t). \tag{2.1.14}$$

Here, $\boldsymbol{u} \in \mathbb{R}^d$ is the particle displacement with d being the number of considered space dimensions, $\rho(\boldsymbol{r})$ is the space dependent mass density and $p(\boldsymbol{r},t)$ is the acoustic pressure. The second first order equation is the thermal expansion equation, which is sometimes referred to as generalized Hooke's law [178, p.287]:

$$\nabla \cdot \boldsymbol{u}(\boldsymbol{r},t) = -\kappa(\boldsymbol{r})p(\boldsymbol{r},t) + \beta T(\boldsymbol{r},t) \tag{2.1.15}$$

with κ being the medium's compressiblity, β being the thermal coefficient of volume expansion and T being the medium's temperature.

Applying $\nabla\cdot$ to (2.1.14) and ∂_{tt} to (2.1.15), the redundant term $\nabla \cdot \partial_{tt}\boldsymbol{u}$ can be substituted yielding the photoacoustic wave equation with respect to a spatially varying compressiblity and mass density:

$$\nabla \cdot (\rho(\boldsymbol{r})\nabla p(\boldsymbol{r},t)) - \kappa(\boldsymbol{r})\,\partial_{tt}p(\boldsymbol{r},t) = -\beta\,\partial_{tt}T(\boldsymbol{r},t). \tag{2.1.16}$$

It can be very useful to express the scattering potentials compressiblity κ and mass density ρ by their respective variations γ_κ and γ_ρ, which are defined as percental deviations from the respective steady parts κ_0 and ρ_0:

$$\begin{aligned} \gamma_\kappa &= (\kappa(\boldsymbol{r}) - \kappa_0)/\kappa_0 \\ \gamma_\rho &= (\rho(\boldsymbol{r}) - \rho_0)/\rho(\boldsymbol{r}) \end{aligned}. \tag{2.1.17}$$

Note that γ_κ is normalized by the respective steady part, whereas γ_ρ is normalized by the respective alternating part, which ensures good readability of the wave equation. The right hand side of (2.1.16) can be expressed in terms of the heating function $H(\boldsymbol{r},t)$, which has been introduced in section 2.1.2, because the heating function is directly proportional to the temperature variation in time [178, p.287]:

$$H(\boldsymbol{r},t) = \rho_0 C\,\partial_t T(\boldsymbol{r},t) \tag{2.1.18}$$

with C being the heat capacity. Substituting (2.1.17) and (2.1.18) into (2.1.16) and using the steady part of the speed of sound c_0 as:

$$c_0 = (\kappa_0\rho_0)^{-1/2} \tag{2.1.19}$$

the general photoacoustic wave equation in heterogeneous media reads as:

$$\begin{aligned}\left(\Delta - c_0^{-2}\partial_{tt}\right)p(\boldsymbol{r},t) = \quad & -\beta C^{-1}\partial_t H(\boldsymbol{r},t) \\ & +\nabla\cdot\left(\gamma_\rho(\boldsymbol{r})\nabla p(\boldsymbol{r},t)\right) \\ & +c_0^{-1}\gamma_\kappa(\boldsymbol{r})\partial_{tt}p(\boldsymbol{r},t).\end{aligned} \tag{2.1.20}$$

In this notation, the equation appears as a wave equation with three source terms, where the first source term reflects photoacoustic sources, which do not depend on the acoustic wavefield p, but the two other source terms are scattering sources according to compressiblity variations and mass density variations, whose strength does depend on p.

To relate the photoacoustic wavefield p to the initial pressure distribution p_0, (2.1.12) is substituted into (2.1.20), yielding:

$$\boxed{\begin{aligned}\left(\Delta - c_0^{-2}\partial_{tt}\right)p(\boldsymbol{r},t) = \quad & -c_0^{-2}\partial_t\eta(t)p_0(\boldsymbol{r}) \\ & +\nabla\cdot\left(\gamma_\rho(\boldsymbol{r})\nabla p(\boldsymbol{r},t)\right) \\ & +c_0^{-2}\gamma_\kappa(\boldsymbol{r})\partial_{tt}p(\boldsymbol{r},t).\end{aligned}} \tag{2.1.21}$$

To be exact, if H_t is not delta-like, meaning the laser pulse length is in the order of the measured frequencies of the photoacoustic wave, p_0 is not exactly an initial source distribution, since the source is not an instantaneous source. Therefore, p_0 will from now on be referred to as photoacoustic source distribution, reflecting the spatial distribution of a temporally varying acoustic source.

In the frame of this thesis, this is the most general version of the photoacoustic wave equation. Subsequent chapters will deal with simplifications for this wave equation that are supposed to be accurate enough to solve a certain problem. In section 2.2 of this chapter, conventional reconstruction algorithms neglecting scattering are presented. This can be a valid assumption in some cases and is essential if low computational complexity is the most crucial factor for an application. However, it is accordingly shown in chapter 3 that this simplification can also harm image quality severely for strongly scattering media, large source contrasts and for high penetration depths. Hence the adjacent chapters deal with approaches to consider more accurate representations of the wave equation. In the end, the final aim of this dissertation is to assess the required trade off between accuracy of the underlying model and the complexity of computation and accuracy of reconstruction.

2.1.4 The Number of Space Dimensions

In the previous sections, the general case of d space dimensions was always considered. Most of the theorems in this dissertation basically apply to an arbitrary positive number of considered dimensions higher than or often even equal to one. The only requirement is that the hyperplane, on which the signal is measured, is always defined in a space that has one dimension less than the wavefield space. For the three-dimensional case, this would imply a measurement on an area. In fact, two dimensional ultrasound detection arrays exist and are a popular research topic [83]. The single elements of two dimensional arrays can usually not be accessed simultaneously, due to the huge amount of required cables. A two dimensional array with 256×256 elements, for example, would require 65536 coaxial connections to the ultrasound front end electronics. A common way to circumvent this, is to apply pre-beamforming where elements are already connected in groups [111]. Obviously, this implies less flexibility in signal processing. Furthermore, as state of the art, most imaging devices and setups exhibit one dimensional arrays, such as linear arrays and many algorithms, even if applicable on three dimensions, only run sufficiently fast on in two dimensions. For those reasons, this dissertation will be restricted to the use of commonly used one-dimensional linear arrays. This evokes the question, if an imaging model derived in two dimensions is suitable for a sound propagation in three dimensions that is evaluated in one slice. Obviously, this is not exactly the case. A two dimensional model matches a three dimensional space, in which all quantities on the third dimension are constant. In contrast, the acoustic wave in a linear-array excitation travels in a three dimensional space with an elevational focus. Multiple effects, such as effective attenuation, out-of plane scattering and elevational focus effects cannot be considered in a two dimensional model. However, if the impact of out-of-plane interactions with the imaging plane is small, a complete neglection of the third dimension will significantly simplify the derivation of imaging algorithms. Thus, the impact of a model that is derived in two dimensions and applied to three dimensional acquisitions using an elevationally focused linear array will be discussed in this chapter and an idea of the impact on the image accuracy will be provided. In general, it can be stated that in most of the cases, the simplification to a two dimensional model will yield a reconstruction result that does not perfectly reflect the actual distribution, but most of the algorithms should still return adequate data. Since, in the frame of this dissertation, quantitative imaging is not aimed for, the problems associated with the two dimensional modeling should generally be negligible.

An extensive discussion on two dimensional modeling of PA imaging with linear arrays can be found in [101].

The Impact of the Wave Front Shape

The shape of the wavefront that originates in a point source in time and space is significantly different for three than for two space dimensions. The function characterizing such a system response to a point source is called Green function and can be employed to compute the solution to wavefields with arbitrary source distributions. For the homogeneous wave equation, which implies the left hand side of (2.1.21) equaling zero, the two dimensional free-field Green function in time and space domain writes as [17]:

$$g_0^{(2D)} = \frac{\Theta(tc_0 - |\boldsymbol{r}|)}{2\pi\sqrt{(tc_0)^2 - |\boldsymbol{r}|^2}} \tag{2.1.22}$$

with Θ being the Heaviside function defined as $\Theta(\xi) = \begin{cases} 0 & , \xi < 0 \\ 1 & , \xi \geq 0 \end{cases}$. The respective three dimensional Green function writes as [17]:

$$g_0^{(3D)} = \frac{\delta(tc_0 - |\boldsymbol{r}|)}{4\pi|\boldsymbol{r}|}, \tag{2.1.23}$$

where δ signifies the delta-distribution with $\delta(\xi) = \partial_\xi \Theta(\xi)$. Both Green functions equal zero for $tc_0 < |\boldsymbol{r}|$, equal infinity for $tc_0 = |\boldsymbol{r}|$ and disappear for $(tc_0 - |\boldsymbol{r}|) \to \infty$. Still, there are two major differences. At first, the amplitude of a solution according to $g_0^{(3D)}$ scales differently with distance from the source position to the observing position than $g_0^{(2D)}$. This is due to energy conservation, since the energy is distributed either over a sphere or over a circle. Secondly, $g_0^{(3D)}$ is instantly zero for $tc > |\boldsymbol{r}|$, while $g_0^{(2D)}$ converges to zero but never actually equals zero. This effects, for example, the mathematical validity of time reversal algorithms, since waves that exist until infinity cannot correctly be temporally reversed, since they cannot completely be measured [76].

The effect of deriving the model in two dimensions and applying it to a measurement on one line in a three-dimensional space creates two effects related to the wave fronts: The strength of sources in higher depths and the spatial extent of these sources are both overestimated. The overestimated amplitude could approximately be solved by a weighting of the reconstructed sources. The overestimation in spatial extent might be mitigated by inverse

filtering. However, this effect is less crucial for realistic band limited data, as shown in Figure 2.1.1, where the wave fronts of a point source with Gaussian pulse excitation of 10 MHz center frequency and 50% fractional bandwidth are compared for a 2D and a 3D Green function.

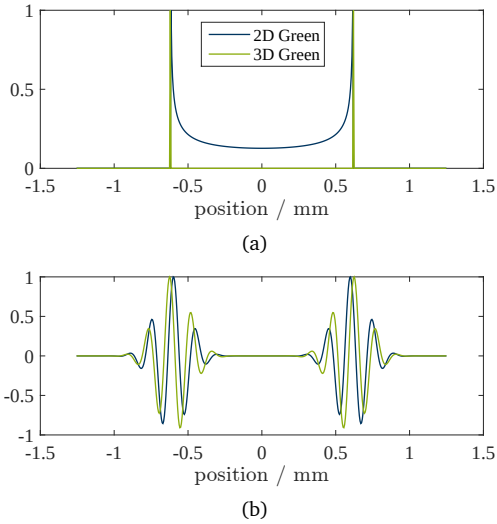

Figure 2.1.1: Comparison of 2D and 3D Green functions where all functions are normed to a maximum value of one; Green functions in 2D and 3D (a), bandlimited Green functions with center frequency of 10 MHz and a fractional bandwidth of 50%

The Impact of Elevational Directivity

An acoustic sensor with infinitely small extent into the neglected dimension would have a constant directivity into this dimension. In the following, this dimension will be referred to as the elevational dimension. To enable imaging in one image plane and to increase sensitivity, an actual acoustic sensor exhibits a large elevational extent and is usually combined with an acoustic lens, that causes a focus effect into the image plane. This implies that at a specific depth, most of the signal that can be detected actually originates from the image plane. Apart from this focus depth, however, sources out of the plane

can also contribute to the measured signal. For structures that are constant along the respective wave fronts, this does not make a difference to a perfect image slice. For structures that are differently shaped into elevational direction, however, this implies that the reconstructed sources will always differ from the actual distribution in the slice defining the image plane. A very important problem associated with such out-of-plane sources in PA imaging is called "direct clutter". Direct clutter primarily occurs, when the incident light is absorbed in the skin apart from the image plane and creates a wave traveling elevationally towards the transducer, which is then misinterpreted as a source from a certain depth in axial direction. Furthermore, the illumination can have an impact on the sensitivity distribution in elevational direction. In [23], a bending of the image plane towards the light source was observed for a single sided illumination, which is due to the fact that higher fluences can overcome the sensitivity decrease due to elevational focusing.

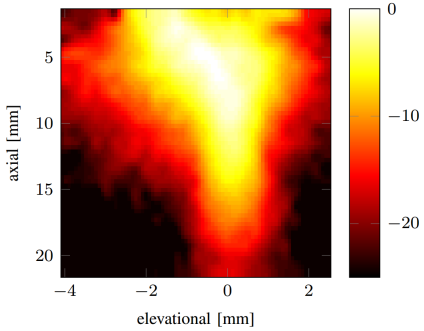

Figure 2.1.2: Sensitivity map of Fullphase transdcuer in dB [23] © 2017 IEEE

The same problem that was described here for acoustic sources holds for acoustic scatterers. The effect of the elevational directivity cannot completely be reversed, if no additional information about the elevational distribution of sources or scatterers is provided. However, assuming a decently designed acoustic lens and moderate variations of the source and scatterer distributions in elevational direction close to the image plane, these effects can be assumed not to affect the reconstructed image too much.

2.2 Conventional Photoacoustic Reconstruction

Most PA reconstruction algorithms do not account for heterogeneous medium properties. While the investigation of the impact of this simplification and a demonstration of methods to conquer this problem will be the main purpose of this dissertation, this chapter gives a quick overview over such standard reconstruction algorithms that neglect acoustic heterogeneities. All listed methods refer to a linear array imaging setup as depicted in Figure 2.2.1 and are here generally described for an infinite aperture. They are divided into algorithms in the time and space domain and algorithms in the frequency domain.

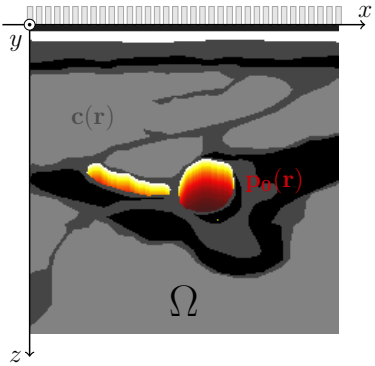

Figure 2.2.1: Imaging geometry with linear array sensor at $z = 0$ indicated by gray rectangles, speed of sound distribution (gray) overlayed by colored PA source distribution

2.2.1 Time-Space Domain Methods

The probably most intuitive and least model based approach to perform a PA reconstruction is the delay-and-sum (DAS) method. In a DAS reconstruction, the travel times Δt from each pixel at (x, z) to each transducer element at $(x', 0)$ are defined by:

$$\Delta t = \sqrt{(x - x')^2 + z^2}/c_0 \tag{2.2.1}$$

and the channel data are read out at the respective travel times followed by a summation over all channels:

$$\boxed{p_0^{(DAS)}(x,z) = \int_{-\infty}^{\infty} p_m(x', \Delta t(x', x, z))dx'} \tag{2.2.2}$$

In this continuous definition of the linear array transducer, x' is the location on the transducer, which is assumed to be infinite, while an actual transducer is limited to a finite interval $[x_1, x_2]$ and has discrete element positions. This approach is very common and its accuracy and computational efficiency depends strongly on the interpolation method that is employed to read out the discrete data set at the continuous delays Δt.

The model based representation of the delay and sum algorithm is known as universal back propagation (UBP) and is based on an actual mathematical inversion [185]:

$$\boxed{p_0^{(UBP)}(x,z) = \int \frac{2}{\pi} \sin(\phi) \frac{1 - \Delta t \partial_{\Delta t}}{(x-x')^2 + z^2} p_m(x', \Delta t) dx'} \tag{2.2.3}$$

where $\phi(x, x', z)$ is the angle from the detector element at $(x', 0)$ to the reconstructed pixel (x, z) and $\partial_{\Delta t}$ is the partial derivative operator with respect to Δt. Comparing the UBP and DAS algorithms, the only difference is the term $\frac{2}{\pi} \sin(\phi)(1 - \Delta t \partial_{\Delta t}) / \left((x-x')^2 + z^2\right)$, which can be rewritten as a convolution with p_m (2.2.3). The mapping law between p_m and p_0 by Δt, however, is exactly the same. The mapping law for one explicit channel is depicted in Figure 2.2.2, which yields the reconstruction of one axial line after lateral integration.

2.2.2 Frequency Domain Methods

Besides the relation between measurement data and image data in time-space domain there is also a relation in the temporal and spatial frequency domain, which can be used to derive reconstruction algorithms. The relation, the respective forward and inverse mapping laws as well as different approaches to use the relation for reconstruction in the frequency domain are demonstrated in the following.

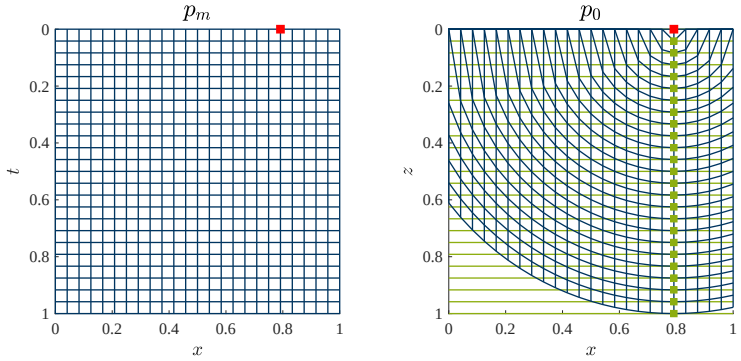

(a) (b)

Figure 2.2.2: Correspondence of time domain data grids; the measurement data grid (a) is mapped on the image data grid (b) followed by an integration along the green lines to get the reconstruct the pixels indicated by the green squares, all axes are normalized to their maximum value

The K-Space Relation

A fundamental relation between the space of measurements and the object space, or, in other words, the photoacoustic source distribution and the measurement on a line sensor is referred to as k-space relation. It states that each data point in the two dimensional spectrum of p_m corresponds to one data point in the two-dimensional spectrum of p_0, which has been demonstrated in various publications [15, 16, 187]:

$$p_m(k_x, k_t) = \frac{k_t \eta(k_t)}{2c_0\kappa_z} p_0(k_x, k_t\sqrt{1-k_x^2/k_t^2}), \tag{2.2.4}$$

where k_t is the temporal wave number associated with the temporal angular frequency ω by $k_t = \omega/c_0$. The impulse response $\eta(t)$, which has been mentioned before in (2.1.21), is usually described as laser pulse shape but can also include the system's acousto-electric impulse response. There are some alterations of this equation. Mostly, the impulse response is not considered, which turns the problem into an initial value problem and in some approaches,

a solid-wall boundary condition is applied instead of a matched boundary condition, which leads to a relation with a cosine transform instead of a Fourier transform [33, 101, 102].

The k-space relation in (2.2.4) describes a mapping law, where each position in the two dimensional spatial frequency domain of p_0 corresponds to one position in the temporal-spatial frequency domain of p_m, which makes it easy to invert. In forward direction, the frequency grid of the image data is not regular and the mapping law is described by:

$$(k_x, k_z) = (k_x, k_t\sqrt{1 - k_x^2/k_t^2}). \tag{2.2.5}$$

This can be inverted to read out the image frequencies in the measurement frequency grid:

$$(k_x, k_t) = (k_x, \sqrt{k_x^2 + k_z^2}) \tag{2.2.6}$$

which results in a regular grid of image data. Solving this relation for the initial pressure distribution p_0 on it's regular spatial frequency grid (k_x, k_z), yields:

$$\boxed{p_0(k_x, k_z) = \frac{2c_0 k_z}{\kappa_t \eta(\kappa_t)} p_m(k_x, \sqrt{k_x^2 + k_z^2}).} \tag{2.2.7}$$

This implies that the amplitude of reconstructed image data at the frequency vector (k_x, k_z) depends on the spectrum of the impulse response at $k_t = \sqrt{k_x^2 + k_z^2}$. Figure 2.2.3 shows the frequency domain mapping. According to the bending of the shape of the mapped grid, the frequency domain mapping seems to resemble the mapping law in time-space domain in Figure 2.2.2, but here, one position in the image data directly corresponds to one position in the measurement data without the need for integration. The calculation of the inverse of $\eta(k_t)$ is generally problematic, especially in the presence of noise and thus, $\eta(k_t)$ is often approximated by 1. In chapter 4.2.2, a Wiener filter approach to account for η is demonstrated instead.

Inversion Approaches

There are different approaches how to use the k-space relation for a PA reconstruction. In the frame of this dissertation, they are categorized as “grid mapping”-methods, a “non-uniform Fourier”-method and a “filtered back propagation”-method.

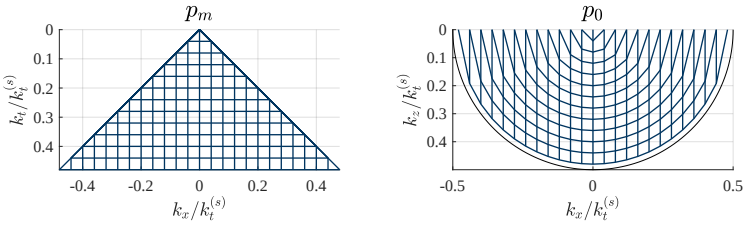

(a) (b)

Figure 2.2.3: Correspondence of frequency domain data grids: the measurement data grid (a) directly corresponds with the image data grid (b), all axes are normalized to the temporal sampling wave number $k_t^{(s)} = 2\pi f_s/c_0$ and only the positive sideband is shown.

Grid mapping methods perform an interpolation in the frequency domain. The usual line of action is to assign values to p_0 on an equidistant frequency grid that are read out of p_m on a curved grid according to the inverse mapping law in (2.2.6). Such an approach was used in the inherent PA reconstruction in the k-wave toolbox [172]. Theoretically, a mapping can also be applied the other way around by making use of the forward mapping law in (2.2.5). The line of action would be to map the values of p_m from an equidistant grid to a non-equidistant grid of p_0 and to perform an interpolation that reads out these scattered values on an equidistant grid (k_x, k_y). This approach rather matches the illustration in Figure 2.2.3 but requires scattered interpolation while the first approach only requires gridded interpolation. The key component of a grid mapping is the interpolation approach, as a falsely interpolated frequency generates errors throughout the image. In [88], a forward relation for discrete data based on the mapping law in (2.2.6) is introduced and a regularized truncated interpolation scheme to retrieve p_0 is derived.

An alternative to grid mapping by interpolation is to numerically calculate the respective Fourier integral onto a non-equidistant grid, which is here referred to as non-uniform Fourier method:

$$\boxed{p_0(k_x, k_z) = \frac{2c_0 k_z}{\kappa_t \eta(\kappa_t)} \int_{-\infty}^{\infty} p_m(k_x, t) \exp(-i\kappa_t t) dt} \tag{2.2.8}$$

with the artificial temporal wave number:

$$\kappa_t := \sqrt{k_x^2 + k_z^2}. \tag{2.2.9}$$

The manual computation of non-uniform Fourier integrals is time consuming, since no fast Fourier methods can be applied. However, there are methods to approximate non-uniform Fourier integrals with the temporal efficiency of fast Fourier transforms (FFT), which are referred to as non-equispaced or non-uniform fast Fourier transforms [51]. This approach has been used for PA imaging by Haltmeier at al. [71]. Again, an alternative line of action to (2.2.8) can be realized by using the forward k-space relation (2.2.4) and applying an inverse Fourier transform in the direction of the non-equidistant spatial frequency κ_z, defined as:

$$\kappa_z := k_t \sqrt{1 - k_x^2/k_t^2}, \tag{2.2.10}$$

which results in:

$$p_0(k_x, z) = \int_{-\infty}^{\infty} \frac{2c_0\kappa_z}{k_t \eta(k_t)} p_m(k_x, k_t) \exp(i\kappa_z z) d\kappa_z. \tag{2.2.11}$$

This integral cannot be numerically calculated without interpolation. However, it is possible to formulate an analytic solution to the Fourier integral by an integral substitution with $\kappa_z := k_t \sqrt{1 - k_x^2/k_t^2}$ and with the differential element $d\kappa_z = \frac{-k_t}{\sqrt{k_t^2 - k_x^2}} dk_t$, which results in the filtered back propagation algorithm:

$$\boxed{p_0(k_x, z) = -2c_0 \int_{-\infty}^{\infty} \frac{\exp(i\kappa_z z)}{\eta(k_t)} p_m(k_x, k_t) dk_t.} \tag{2.2.12}$$

This resembles the Fourier synthetic aperture focusing technique (FSAFT) algorithm described in [28], with the only difference that the filter term $2c_0/\eta(k_t)$ was neglected there. This algorithm will be extended by an operation that accounts for acoustically heterogeneous media during the back propagation in chapter 5.

In terms of computational effort, Fourier methods can exploit the direct correspondence of each pixel in the image space with one pixel in the measurement space. The computationally intensive Fourier transforms can often be computed by efficient fast Fourier methods. If, however, only a small region of interest of the image is required for reconstruction, time-space domain methods can compute these efficiently by only evaluating the pixels in this region,

while the evaluation of a small region of interest still requires all frequency positions to be read out to avoid wrapping of image structures into the region of interest. Also, time-space domain methods might easily be accelerated by dedicated hardware, since each pixel can be computed in parallel.

2.3 Photoacoustic Imaging Systems

Like all imaging modalities, photoacoustic imaging requires a forward model of the measurement process. This forward model relates the photoacoustic source distribution to measurement data on the surface of the imaged object. The task of reconstruction is to determine an inverse model to the forward model that relates the measurements on the surface to a source distribution. In general, a forward model is a simplified solution to the photoacoustic wave equation (2.1.21). The corresponding inverse model needs to be discretized and can then be implemented as a reconstruction algorithm. While such reconstruction algorithms will be presented throughout this dissertation, this chapter rather addresses the hardware components by providing an overview about systems that were proposed in research as well as already available commercial systems.

In general, a photoacoustic imaging system consists of a laser that emits light, which illuminates the tissue of interest and an acoustic sensing device, which can be a commercial ultrasound system with the ability to trigger the laser or to be triggered by the laser. Sometimes, custom made ultrasound probes and ultrasound systems are employed for dedicated PA imaging.

Many setups consist of a transducer surface that encloses the imaged area completely or almost completely in the image plane [167, 174, 183]. Such a full view setup is very fortunate in terms of reconstruction, but applications are limited, since the light can only be completely distributed in the imaged area if the imaged object is small or translucent. Hence, this technique is very common in small animal imaging [29, 62]. Another application is breast imaging, since the female breast can be illuminated from all sides and is fairly translucent. A review about PA breast imaging can be found in [124]. In other PA setups, an actual signal processing based reconstruction does not need to be performed. For example in photoacoustic microscopy, a small laser beam or the acoustic receive focus scans the surface of the object and two dimensional or even three dimensional distributions can directly be attained [135, 189, 190, 195]. Lately, non-contact imaging systems have been introduced, which, in contrast to usually employed piezo-based transducers, measure vibrations on the surface

using interferometry [145].

Apart from the aforementioned approaches, this dissertation focuses on handheld linear arrays for combined photoacoustic and ultrasound (PAUS) acquisition. The first real-time combined photoacoustic and ultrasound (PAUS) system was reported in 2006 by Niederhauser et al. [133]. The system comprises a custom made ultrasound system and a Q-switched alexandrite laser that generates laser pulses, which were delivered through an optical fiber and a prism-mirror combination to the skin with a radiant exposure of 5 mJ/cm^2. Many comparable systems using a commercial ultrasound probe that is connected to a light guide through which the laser is guided towards the tissue with an illumination from both sides have been introduced. Most of those systems use a Q-switched Nd:Yag laser [96] [60], sometimes in combination with an OPO [70]. Such a setup has also been marketed as a commercial system by VisualSonics (Fujifilm) [131].

Another approach is the so called PA enabling device (PED) that has been proposed in [127]. The PED can be connected to an ultrasound probe and the sound is reflected by an acoustic mirror by 90 degrees. The laser light is transmitted through the acoustic mirror, such that the illumination appears right in the ultrasound image plane.

In contrast to systems that employ commercial ultrasound probes, dedicated transducers have been designed for photoacoustic imaging by several groups. The MSOT system by Ntziachristos [30], for example, consists of a circularly shaped array with a small laser window on top and is capable of deep tissue imaging, such as imaging of the carotid artery in vivo [50]. Razansky et al. proposed a 2D array with 256 elements and a solid angle view of 90° with illumination through a hole in the transducer center. This system is able to acquire multi-wavelengths 3D data in real time [46].

To enable the transition of PA imaging from a laboratory based research modality to a clinical imaging tool, much effort has been dedicated to improve costs and compactness of PA systems. One approach to achieve this is to move from bulky solid state lasers to cheap and space efficient laser diodes. In general, laser diodes do not exhibit as much pulse energy as solid state systems, but this can partially be compensated for by higher repetition frequencies [58]. Earlier diode based systems [99] were developed further and have been proven to enable real time PA imaging with laser diodes, such as the system in [36]. This system was developed in the frame of the 7th Framework research project FULLPHASE and currently improved in the Horizon 2020 project CVENT. Some of the experimental data in this dissertation was acquired with this or similar systems exhibiting even higher pulse energies and multiple wavelengths.

Other groups also suggested to move from laser diodes to LEDs as mentioned in section 2.1.1. More details about some of the mentioned systems can be found in [159, p.17ff].

2.4 Atherosclerosis as a High Impact Application

Among the long list of clinical applications of PA imaging, the characterization of atherosclerosis is an attractive candidate to significantly benefit from the potential of photoacoustics. The term atherosclerosis describes the accumulation of lipids and fibrous elements in arterial vessels. Its related complications are considered as the most common cause of death in western societies [116].

Atherosclerotic lesions start as a fatty streak underlying the endothelium of large arteries, which are the cell layers closest to the lumen. These are caused by monocytes migrating into the intima and differentiating into macrophages (see Fig. 2.4.1). Via scavenger receptors, the macrophages take up oxidized low density lipoproteins which leads to esterification and hence the formation of lipid droplets and foam cells that contain high amounts of cholesterol esters. Smooth muscle cells are a key factor in the evolution of complex lipid lesions as they migrate into the intima and contribute to foam cell formation by taking up modified lipoproteins and by synthesizing extracellular matrix proteins to form a fibrous cap enclosing the lipid pool. An evolving lipid pool leads to narrowing of the vessel lumen, which can harm the perfusion of subsequent organs. Acute cardiovascular events, however, rather result from rupture of the atherosclerotic plaques [65], which can lead to myocardial infarction or stroke, depending on where the lesion is located.

In this dissertation, atherosclerotic lesions in the carotid artery are in focus as they are accessible to state of the art PA imaging systems [50]. Disruption of plaques in the carotid artery can lead to occlusive thrombi in the brain and cause strokes.

Besides genetic risk factors, such as hypertension, diabetes mellitus, the male gender and the metabolic syndrome, certain environmental factors promote the development of atherosclerotic lesions, which are smoking, the lack of exercise, a high fat diet and certain infectious agents [65]. Medical treatments often focus on lowering the risk of atherosclerosis, for example by treating hypertension. Above that, antiplatelet drugs and statins are potential lipid lowering drugs [95]. Statins can significantly prevent the progression of atherosclerosis but not all patients respond to them [65]. Above medical interventions, en-

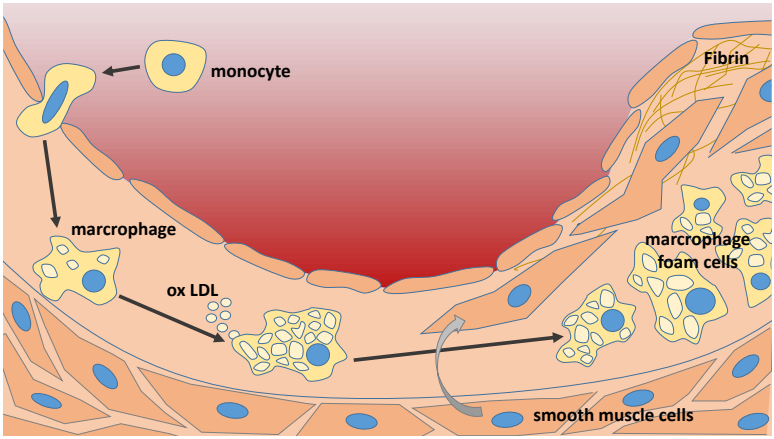

Figure 2.4.1: The process of plaque generation, adapted from Fig. 2 and Fig. 3 in [65]

darterectomy or stenting are the most common surgical procedures, both of which are highly invasive methods with a risk of peri-operative stroke. Hence, surgery should only be applied if the risk of plaque disruption is high. However, it is not always trivial to identify plaques that are prone to rupture [95].

Characterization of the involved constituents of the atherosclerotic lesions by medical imaging might play a key role in the risk assessment of atherosclerotic plaques. According to Lusis et al., efficient non-invasive diagnostic methods are on high demand [116]. Angiography, for example, is a powerful tool to localize a stenosis. However, it does not provide any information about the cause of the stenosis or the composition of potential plaques. The same holds for intravascular ultrasound (IVUS), which, nevertheless, can generate highly resolved images of the arterial walls and can visualize highly echogenic calcifications. In contrast, intravascular multi spectral optical coherence tomography (OCT) can be used for characterization of lipids but for the sake of a penetration depth that is limited to approximately 1 mm. Both IVUS and OCT are invasive methods. Non-invasive imaging modalities, such as magnetic resonance imaging (MRI) and computed tomography (CT) usually require long acquisition times and suffer from motion artifacts. Ultra-fast CT can minimize motion artifacts but still does not provide information about the composition of plaques [5].

Photoacoustic imaging has the potential to be a cost efficient, real time capable alternative to the above mentioned modalities and may provide both morphological information and functional information about atherosclerotic plaques. The penetration depth has been shown to be sufficient for the visualization of the carotid artery [50]. Also, the possibility to acquire images with a spectral information by tuning the laser wavelength is a unique feature of PA imaging and has already been exploited to determine the composition of human vessel walls with lipid cores ex vivo [5]. This allows for numerous approaches to estimate the vulnerability of plaques. Plaque rupture is known to be more likely to occur, if the lesion has a fibrous cap, a high concentration of lipid-filled macrophages in the plaque's shoulder region and a large necrotic core [38, 109]. Neovascularization is also investigated to play a role in plaque instability [65, 128]. Also, for the femural artery, the risk of the restenonis after removal was reported to be related to the plaque's composition [47]. Hemorrhage into the plaque has been found out to correlate with plaque rupture even though it was not identified as a cause [134]. For these mentioned indicators of plaque vulnerability, PA imaging is a promising tool to be employed for identification. Besides attempts to access the carotid artery by illumination through the skin [50], an illumination by a probe inserted in the pharynx has been suggested [104], as well as intra vascular PA probes [90, 91].

All findings presented in this dissertation can apply to any application of PA imaging in acoustically heterogeneous media. Due to the high impact of atherosclerosis, however, the benefit of increasing the PA image quality is motivated by the improvement of carotid artery imaging throughout this dissertation. Since, compared to other applications of PA imaging, the carotid artery is a fairly deep target, problems associated with heterogeneous media, such as aberrations and clutter, might be of higher impact than for superficial targets. Therefore, a numerical phantom of a cross section of the carotid artery was designed that will be used to demonstrate the benefit of the proposed algorithms in simulation studies. The phantom comprises a photoacoustic source distribution and a speed of sound distribution (see Fig. 2.4.2), whose shapes have been derived from ultrasound images of the neck provided by Dr. Michael Jäger from the University of Bern. The boundaries were segmented manually and the resulting map was compared to an anatomic atlas to assign one kind of biological tissue to each region. Respective material properties for both PA source distribution and SOS distribution were then assigned to the regions, which are listed in table 2.4.1 and which have been derived from literature.

Property	Tissue	Value	Unit
speed of sound	skin	1730	m/s
	fat	1450	m/s
	muscle	1590	m/s
	blood	1575	m/s
	fascia	1525	m/s
	water	1480	m/s
absorption coefficient	blood	5	1/cm

Table 2.4.1: Properties of carotid artery phantom (SOS and PA source distribution) derived from [67, p.12], [13, p.313] and [142].

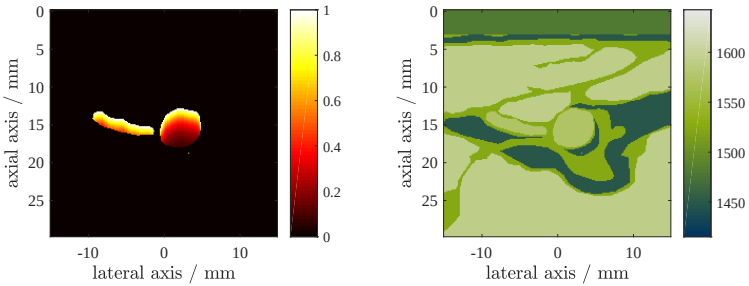

Figure 2.4.2: Numerical carotid artery phantom; nomalized photoacoustic source distribution (a), speed of sound distribution in m/s (b)

3

Acoustic Heterogeneities in Photoacoustic Imaging

The main purpose of this dissertation is to develop methods that account for acoustic heterogeneities during a photoacoustic reconstruction. Therefore, in this chapter, a full wave model for a forward propagating photoacoustic wave in a heterogeneous medium is derived. The derivation resembles that of a general US imaging forward model in some aspects, but, based on a thorough literature reserach, it has not been demonstrated for PA imaging before. Afterwards, the impact of these heterogeneities in actual imaging environments is discussed. In the progress of this chapter, artifacts related to heterogeneous media are classified as clutter artifacts and aberration artifacts. The respective mechanisms leading to these artifacts are described and approaches from literature dealing with the reduction of the respective artifact are presented.

3.1 Photoacoustic Wave Propagation in Heterogeneous Media

The aim of the following derivation is to find a solution to $p(\boldsymbol{r}, t)$ according to the photoacoustic wave equation in heterogeneous media that was derived in chapter 2.1.3 as (2.1.21). To ensure a readily comprehensible notation, the photoacoustic source and the scatter operator are henceforth expressed by

$q(\boldsymbol{r},t)$ and $V_\gamma(\boldsymbol{r})$, respectively:

$$\begin{aligned} q(\boldsymbol{r},t) &:= -c_0^{-2}\partial_t \eta(t) p_0(\boldsymbol{r}) \\ V_\gamma(\boldsymbol{r}) &:= \left[\nabla\cdot\left(\gamma_\rho(\boldsymbol{r})\nabla\right) + c_0^{-2}\gamma_\kappa(\boldsymbol{r})\partial_{tt}\right] . \end{aligned} \tag{3.1.1}$$

To avoid confusions, it should be clarified that, in this notation, applying the term $\nabla\cdot\left(\gamma_\rho(\boldsymbol{r})\nabla\right)$ to $p(\boldsymbol{r},t)$ equals $\nabla\cdot\left(\gamma_\rho(\boldsymbol{r})\nabla p(\boldsymbol{r},t)\right)$. Furthermore, to increase readability, the homogeneous wave operator $\Box$ and the heterogeneous wave operator $\Box_\gamma$ are defined as:

$$\begin{aligned} \Box &:= \left[\Delta - c_0^{-2}\partial_{tt}\right] \\ \Box_\gamma &:= \left[\Box - V_\gamma(\boldsymbol{r})\right] . \end{aligned} \tag{3.1.2}$$

In this notation, the photoacoustic wave equation in heterogeneous media (2.1.21) reduces to

$$\Box_\gamma\, p(\boldsymbol{r},t) = q(\boldsymbol{r},t). \tag{3.1.3}$$

In the following, an analytical solution to (3.1.3) is derived by means of Green functions. The concept of Green functions, which are also referred to as "Green's functions", was introduced by George Green in 1828 as an approach to solve inhomogeneous partial differential equations [27, p.56ff]. The quantities $q(\boldsymbol{r},t)$, $\gamma_\rho(\boldsymbol{r})$ and $\gamma_\kappa(\boldsymbol{r})$ are assumed to be spatially confined to a region Ω and $q(\boldsymbol{r},t)$ is furthermore temporally confined to $t\in[0,\infty[$, such that $q(\boldsymbol{r},t),\gamma_\rho(\boldsymbol{r}),\gamma_\kappa(\boldsymbol{r})\in\Psi$ with $\Psi=\Omega\times[0,\infty[$. The solution to the photoacoustic wave equation in (3.1.3) can be expressed in terms of the outgoing full wave Green function for heterogeneous media g_γ as (compare [49, p.394]):

$$p(\boldsymbol{r},t) = \int_\Psi g_\gamma(\boldsymbol{r},t,\boldsymbol{r}',t')q(\boldsymbol{r}',t')\,d\boldsymbol{r}'dt', \tag{3.1.4}$$

where g_γ is a function of γ_ρ and γ_κ and solves:

$$\Box_\gamma\, g_\gamma(\boldsymbol{r},t,\boldsymbol{r}',t') = \delta(\boldsymbol{r}-\boldsymbol{r}')\delta(t-t'). \tag{3.1.5}$$

Unlike the free field outgoing Green function g_0, which solves

$$\Box\, g_0(\boldsymbol{r}-\boldsymbol{r}',t-t') = \delta(\boldsymbol{r}-\boldsymbol{r}')\delta(t-t'), \tag{3.1.6}$$

a closed form to describe g_γ analytically does not exist. Its argument can furthermore not be expressed as difference of the source location and time

and the readout location and time $(\boldsymbol{r}-\boldsymbol{r}', t-t')$. However, it can be related to g_0 and the scattering potentials by (compare [49, p.391]):

$$\begin{aligned} g_\gamma(\boldsymbol{r},t;\boldsymbol{r}',t') = \quad & g_0(\boldsymbol{r}-\boldsymbol{r}',t-t') \\ & + \int_\Psi g_0(\boldsymbol{r}-\boldsymbol{r}'',t-t'')V_\gamma(\boldsymbol{r}'',t'')g_\gamma(\boldsymbol{r}'',t'';\boldsymbol{r}',t')d\boldsymbol{r}''dt'' \end{aligned} . \tag{3.1.7}$$

Note that, as discussed in chapter 2.1.4, all examples in this dissertation are presented in two dimensions and, hence, g_0 equals $g_0^{(2D)}$ in (2.1.22). Substituting (3.1.7) into (3.1.4), the photoacoustic wavefield can generally be described as the superposition of the wavefield that would have evolved in a homogeneous medium p_h and a scattered wavefield p_{sc}:

$$p(\boldsymbol{r},t) = p_h(\boldsymbol{r},t) + p_{sc}(\boldsymbol{r},t), \tag{3.1.8}$$

where p_h matches the solution to wave equation $\Box p_h = q$ and the scattered wavefield p_{sc} depends on the full wavefield p:

$$\begin{aligned} p_h(\boldsymbol{r},t) = \quad & \int_\Psi g_0(\boldsymbol{r}-\boldsymbol{r}',t-t')q(\boldsymbol{r}',t')\,d\boldsymbol{r}'dt' \\ p_{sc}(\boldsymbol{r},t) = \quad & \int_\Psi g_0(\boldsymbol{r}-\boldsymbol{r}'',t-t'')V_\gamma(\boldsymbol{r}'',t'')p(\boldsymbol{r}'',t'')d\boldsymbol{r}''dt'' \end{aligned} . \tag{3.1.9}$$

While p_h can be solved directly using the solution for $g_0^{(2D)}$ in (2.1.22), there is no direct solution to p_{sc}, since it is a function of the full wavefield p, which is not a known quantity. Still, the solution to $p(\boldsymbol{r},t)$ in (3.1.8) can be expressed only as a function of known quantities. Therefore, (3.1.8) is solved for p_h after substituting p_{sc} from (3.1.9), which yields:

$$p_h = [1 - G_0 V_\gamma]p \tag{3.1.10}$$

with the operator G_0 defined as $G_0 := \int_\Psi d\boldsymbol{r}'dt'\, g_0(\boldsymbol{r}-\boldsymbol{r}', t-t')$. The operator G_0V_γ describes single scattering of the wavefield it is applied to. Solving (3.1.10) for p and substituting p_h according to (3.1.9) yields:

$$p = [1 - G_0 V_\gamma]^{-1} G_0 q. \tag{3.1.11}$$

This inverse operator in (3.1.11) can now be rewritten by making use of Neumann series expansion, which is related to the geometric series (compare [49, p.225]):

$$\boxed{p(\boldsymbol{r},t) = \sum_{i=0}^{\infty} \left(G_0 V_\gamma\right)^i G_0 q(\boldsymbol{r}_0, t_0)} . \tag{3.1.12}$$

Here, the term $(G_0 V_\gamma)^i$ denotes a recursive application of $G_\gamma V_\gamma$ for i times, such that:

$$\left(G_0 V_\gamma\right)^{i+1} = \int d\boldsymbol{r}_i dt_i \, g_0(r_{i+1} - r_i, t_{i+1} - t_i) V_\gamma \left(G_0 V_\gamma\right)^i \tag{3.1.13}$$

with

$$\left(G_0 V_\gamma\right)^0 = 1, \tag{3.1.14}$$

This series expansion is commonly referred to as Born series. For (3.1.12) to hold, the series must converge. This condition is met for sufficiently small values of V_γ, or, according to (3.1.1), for sufficiently small values of γ_κ and γ_ρ and low temporal frequencies. Substituting V_γ from (3.1.1) into (3.1.12), the photoacoustic wavefield p only depends on the known free field Green function g_0 and on the observable quantities $q(\boldsymbol{r}, t)$, $\gamma_\rho(\boldsymbol{r})$ and $\gamma_\kappa(\boldsymbol{r})$. In consequence, an exact direct solution to (3.1.3) is shown to exist, even though it contains an infinite series and is difficult to compute precisely. In the notation in (3.1.12), it is clearly visible, that the generated photoacoustic pressure depends linearly on the photoacoustic source distribution q, while the dependence on the scatterer distributions is nonlinear due to the exponents of V_γ. This is important in terms of solving the inverse problem, as reconstructing sources in a known scatterer distribution is a linear problem, while reconstructing scatterers is not linear, even if the source distribution is known. Truncating (3.1.12) for $i > 1$ returns the Born approximation, which, in contrast, sets p into a linear relation with $\gamma_\rho(\boldsymbol{r})$ and $\gamma_\kappa(\boldsymbol{r})$. A more general description of how to solve a radiation problem in heterogeneous media analytically by using Green functions can be found in [49].

To attain a numerical solution to the wavefield, all quantities can be discretized and equation (3.1.12) can be solved using numerical operations. However, due to the infinite series, this approach is unpractical and it is more common to generate discrete solutions by employing direct numerical solutions to the wave equation (3.1.3). Various approaches for forward simulations of photoacoustic wavefields in heterogeneous media have been proposed. Sheu et al. presented a time domain model based on finite differences [156], which is a very general solution that even incorporates a detailed thermoacoustic model of the thermo-elastic conversion. Other approaches employ finite elements instead of finite differences [194]. As both finite difference and finite element methods require a very dense spatial sampling of about 10 grid points per wavelengths, pseudo-spectral methods are a very popular alternative. By applying the spatial derivatives, which are required for numerically extrapolating the wavefield, in the Fourier domain, the number of required grid points in a

three dimensional problem can be reduced by over 90% [177, p.25]. Pseudo-spectral methods either solve the second order wave equation (3.1.3) [121], or they solve coupled first order equations, such as those in (2.1.14) and (2.1.15) [34]. The second approach was employed for the open source Matlab toolbox "k-wave", which was developed by Treeby et al. in 2010 [14] and which is available at www.k-wave.org.

3.2 Photoacoustic Reconstruction in Heterogeneous Media

The impact of acoustic heterogeneities in biological tissue on the quality of photoacoustic images has been assessed in various publications, whereas, mostly, only the speed-of-sound deviations were under investigation. The variations of speed of sound in soft tissues are usually stated to vary within 10% [168]. The associated scattering effects cause artifacts in the reconstructed images, if the heterogeneities are not corrected for [44]. Some publications focus on the impact of strong scatterers such as air inclusions or bones [40]. In the system proposed by Xia et al., the impact of heterogeneities is validated as minor for weakly scattering tissue, but clearly noticeable for strongly scattering tissue [182]. However, other groups state a relevant impact in media with weakly deviating SOS distributions such as breast tissue [191, 192]. Small variations in the speed of sound, are also investigated in [44] in a simulation study and an ex vivo mouse study. Here, a strong impact of the heterogeneities is stated but the impact of the accuracy of the refraction model for compensating algorithms is claimed to be small.

Besides the reduction of artifacts, there is also the potential to improve the image quality above the quality of images in a homogeneous medium if the acoustic heterogeneities are considered during reconstruction. Generally, the measurements are incomplete due to an aperture of limited size and due to measurements on discrete positions with sensor elements of finite size. For that reason, a reconstruction is usually an ill posed problem. Especially in a setup with a standard linear array, a lot of information is lost during the measurement. This evokes the question if back scattered and refracted waves that are redirected to the transducer can provide additional information about the source distribution that would not have been obtained in a homogeneous medium.

To describe the forward model of a photoacoustic measurement in acoustically heterogeneous media, the evolving wave in (3.1.12) is read out at the

sensor line, which is defined to be the line at $z = 0$ throughout this dissertation. The respective measurement is from now on referred to as p_m with:

$$p_m(x,t) := \int_{-\infty}^{\infty} dz\, p(\boldsymbol{r},t)\delta(z) = p(x,0,t). \tag{3.2.1}$$

It should be noted that an actual measurement operation consists of more than just sifting the pressure at an infinite sensor line. Precise measurement modeling would comprise more properties, such as the averaging over the transducer element size, a sifting at the element positions of finite number and the introduction of accurate boundary conditions to the wavefield. However, for most purposes, a mathematical modeling of the measurement as simple readout out operation is sufficient. The aim of a photoacoustic reconstruction in heterogeneous media is now to find an inverse operation to the following forward model, which maps the source distribution p_0 onto the measurement data p_m:

$$p_m(x,t) = \left[-c_0^{-2} \int_{-\infty}^{\infty} dz\, \delta(z) \sum_{i=0}^{\infty} \left(G_0 V_\gamma\right)^i G_0 \partial_t \eta(t) \right] p_0(\boldsymbol{r}), \tag{3.2.2}$$

which follows from substitution of (3.1.1) and (3.1.12) into (3.2.1).

In the progress of this section, the problem of acoustic scattering in photoacoustic imaging is first viewed as one complete problem and previous approaches to account for this full-wave scattering including the complete physical model in the reconstruction are presented. Then, the artifacts associated with heterogeneous media will be categorized as either reflection related artifacts, which will be referred to as clutter, or as refraction related artifacts, which will be referred to as aberration. Mathematically, the two processes can be distinguished by dividing the Green function into upward traveling part g_0^+ and downward traveling part g_0^-in relation to the z-axis. This yields the two Green functions:

$$\begin{aligned} g_0^+(\boldsymbol{r},t) &:= \frac{\Theta(tc_0 - |\boldsymbol{r}|)}{2\pi\sqrt{(tc_0)^2 - |\boldsymbol{r}|^2}} (1 - \Theta(z)) \\ g_0^-(\boldsymbol{r},t) &:= \frac{\Theta(tc_0 - |\boldsymbol{r}|)}{2\pi\sqrt{(tc_0)^2 - |\boldsymbol{r}|^2}} \Theta(z) \end{aligned} \tag{3.2.3}$$

with Θ being the Heaviside distribution. The respective Green function operator G_0 can thus be split up in to $G_0 = G_0^+ + G_0^-$ and so can the scattered wave p_{sc}:

$$
\begin{aligned}
p_{sc} &= p_{sc}^{+} + p_{sc}^{-} \\
p_{sc}^{+} &= \sum_{i=1}^{\infty} \left(G_0 V_\gamma\right)^i G_0^{+} q. \\
p_{sc}^{-} &= \sum_{i=1}^{\infty} \left(G_0 V_\gamma\right)^i G_0^{-} q
\end{aligned}
\tag{3.2.4}
$$

Note that (3.2.4) is derived from (3.1.12) leaving out the index $i = 0$ in the sum, as this index represents the homogeneous field by $(G_0 V_\gamma)^0 G_0 q = G_0 q = p_h$. This notation will be used to differentiate between parts of the wave that lead to different kinds of artifacts, where p_{sc}^{+} is associated with clutter and p_{sc}^{-} is associated with aberrations, while the full wave scatter problem is described by:

$$
p = p_h + p_{sc}^{+} + p_{sc}^{-}. \tag{3.2.5}
$$

3.2.1 Full Wave Scattering

In the case of a full-view measurement, a common method to include acoustic heterogeneities in a photoacoustic reconstruction is time reversal. While originally introduced as a method, where a measurement is temporally reversed and physically re-emitted by the transducers [55], the term time reversal is nowadays also used to describe a reconstruction technique. In a photoacoustic time reversal reconstruction, the measurement data is reversed in time and then synthetically emitted in a simulation and the resulting wavefield is evaluated at the time corresponding to the light emission, returning an estimate of the initial pressure distribution [35, 76, 173].

In a full view measurement in odd dimensions and if no scatterers are involved, time reversal recreates the actual wavefield perfectly [49, 76, p.81]. In even dimensions, the signal does not completely decay due to the infinite Green function (e.g. (2.1.22) in two dimensions). Hence, the signal cannot be inverted without being measured for an infinite time. In scattering media, the inversion is not perfect, due to the possible occurrence of so called trapping heterogeneities, where parts of the wave never exit the solution area and can thus not be measured [76]. Even for non-trapping media, the reconstruction algorithm can introduce artifact trapping due to imperfect boundary conditions in the simulation [35]. However, a time reversal reconstruction of a full view measurement in a scattering medium in two dimensions usually

returns satisfying data, even though the problem is ill posed [76]. In contrast to time reversal methods, which directly return the final result after one backpropagation, Huang et al. have investigated an iterative method, where the image is updated after a pair of forward and backward propagation, while the backpropagation is calculated using an adjoint operator to the forward operator [79].

In all mentioned cases, the distribution of acoustic heterogeneities is supposed to be known in order to use it for the reconstruction. For exactly known acoustic properties, Stefanov et al. have derived sharp conditions for uniqueness [165]. However in an actual clinical measurement, information about the actual speed-of-sound distribution is generally not availible. The primary question that is diversely discussed throughout literature, is the question if a joint reconstruction of both the photoacoustic sources and the acoustic heterogeneities can be obtained from only photoacoustic measurements. Mathematically, it has been shown by Stefanov et al. that the linearized problem is unstable, indicating that the actual nonlinear problem might also be unstable [164]. However, several groups have presented algorithms that succeed in finding an approximate solution to this problem, at least for a full view measurement with sensors surrounding the imaged object. Huang et al. have presented a nonlinear iterative algorithm that alternatingly updates the speed of sound and the initial pressure distribution [80]. Using Marquard and Tikhonov regularization and simple structures for speed of sound and initial pressure in a simulation study, a joint reconstruction turned out satisfying results. However, Huang et al. conclude that their work also demonstrates the numerical instability of this problem. An algorithm based on a finite element discretization of the Helmholtz equation is presented in [194]. Using a Marquard and Tikhonov regularization scheme for the inversion, they succeeded in the joint reconstruction of phantoms with matching shapes of the speed-of-sound inclusion and the photoacoustic source distribution. Besides regularization, there are other approaches to include a priori knowledge about the scattering distribution, for example by manually determining the general shape of structures with a deviating speed of sound [198].

As many imaging systems are able to acquire ultrasound measurements in addition to photoacoustic measurements, another important question is, if the acoustic heterogeneities can be determined using ultrasound measurements and if this estimation is sufficient to solve the photoacoustic reconstruction correctly. Such an approach has been investigated in thermoacoustic tomography [93] and photoacoustic tomography [122] by estimating a speed-of-sound distribution based on transmission ultrasound data. As an alternative to actu-

ally acquiring a transmission or reflection ultrasound measurement, Dean-Ben et al. placed an optical point absorber of known location in the imaged region [45]. An alternative way to retrieve the speed-of-sound distribution was presented by Huang et al., where information about the shape and acoustic properties of a monkey scull was retrieved from computed tomography (CT) data in order to use it for the photoacoustic reconstruction [78].

Still, all approaches mentioned in this section rely on a full view detector. Even though it has been shown that, under certain conditions, the limited view problem for a known SOS distribution exhibits a unique solution [163], only one of the mentioned publications considers the case of a limited view [79]. Non of the mentioned approaches relied on measurements with a linear array. In chapter 4 of this dissertation, a full wave reconstruction for linear arrays will be derived and assessed in terms of achievable scattering and limited view artifact reduction and the applicability to clinically relevant measurements.

3.2.2 Aberrations

Most mentioned approaches above rely on computationally expensive methods, mostly because of the necessity to simulate acoustic waves during reconstruction, sometimes even multiple times, if the nature of the algorithm is iterative. Aiming for real-time solutions it is important to focus on the actual problems associated with scattering and to determine simpler models to account for those. Hence, in the following, the artifacts introduced by acoustic heterogeneities in photoacoustic imaging are categorized as clutter artifacts or aberration artifacts. Respective algorithms either compensate for reflections or for distortions of the wavefront introduced by acoustic heterogeneities. In contrast to clutter artifacts, where reflections lead to artifacts in the image, aberrations do not introduce additional structures into the image but rather distort the image itself, such that actual shapes cannot be recovered anymore. These artifacts can be assigned to refraction of the photoacoustic wave during the transmission of acoustically heterogeneous media, especially a heterogeneous speed-of-sound distribution. Here, aberration is defined as those image degradations that originate in p_{sc}^{-} in (3.2.4), such that the forward model reads as:

$$p(\boldsymbol{r},t) \approx p_h(\boldsymbol{r},t) + p_{sc}^{-}(\boldsymbol{r},t), \tag{3.2.6}$$

or, in full notation:

$$p(\boldsymbol{r},t) \approx \sum_{i=0}^{\infty} \left(G_0 V_\gamma\right)^i G_0^{-} q(\boldsymbol{r}',t'). \tag{3.2.7}$$

One method to reduce aberration artifacts is the optimization of a global value for the speed of sound, where the actual distribution is neglected [31, 191]. Such an idea has also been extended to a layered medium model [98]. Methods relying on the spatial coherence of the waves from actual sources have been applied to increase the contrast of deeper sources in aberrating media [108, 141]. In a circular sensor setup, aberrations can lead to inconsistencies of the data reconstructed from opposing sensor sides. This encouraged the approach of the so called "half time reconstruction", which suppresses the contribution of certain sensors during the reconstruction [11]. The approach has been further developed by introducing a dedicated weighting of certain channels [41]. In [40] and [42] a statistical model is incorporated and the channel data is weighted according to the probability to exhibit a scattered signal.

None of the aforementioned methods explicitly models the acoustic heterogeneities. Publications that actually consider the speed-of-sound distribution during reconstruction differ mostly in the underlying accuracy of the model describing the influence of the speed-of-sound deviation. Straight ray approaches compute the delays of waves traveling straight through the inhomogeneous medium in a delay-and-sum beamformer [43,44]. Zhang et al. have performed a cross correlation over the entire circularly acquired measurement data set, in order to determine the respective delays [196]. Jose et al. employed a propagation model of higher accuracy by using ray tracing based on the Eikonal approximation [94]. A similar approach was used by Wang et al. [179].

In general, there is an obvious trade-off between the accuracy of the model and the related computational effort. In the frame of this dissertation, a new reconstruction method is introduced that replicates the actual wavefield very accurately and at the same time, can be computed very efficiently (see chapter 5). The method is based on a paraxial approximation of the Helmholtz equation.

3.2.3 Clutter

In photoacoustic imaging, clutter is the general term to describe artifacts associated with reverbing sound waves. The sound waves originating in a photoacoustic source and traveling away from the transducer are scattered back towards the transducer. The reflected waves of strong sources can overcome the amplitude of the waves that originate in weaker photoacoustic sources and, hence, these sources can be obscured in the photoacoustic image. This effect is amplified by the fact that skin, which is known to contain high concentrations of melanin, is generally a strong photoacoustic absorber. At the same time, the

fluence at the skin is very high compared to fluences in deeper tissue. This generates a very strong wave at the tissue's surface, whose reverbing wave generates leads to high intensity structures in deeper image regions [57, 73, 143]. It should be noted that, sometimes, the term clutter is also associated with waves from out-of-plane sources, which also produces artifacts that obscure the actual structures [143]. However, in the scope of this dissertation, this so called "direct clutter" will not be considered, since it is not a result of medium heterogeneities, but a question of the illumination configuration. Thus, the term clutter will henceforth imply that indirect clutter is addressed.

The problem of clutter has been frequently reported and intensively investigated [57, 73, 143]. Mathematically speaking, the scattered wave p_{sc}^{+}, as specified in (3.2.4), is now defined as the part of the wave leading to clutter and the aberration wave p_{sc}^{-} is ignored. This leads to the following approximate forward model:

$$p(\boldsymbol{r}, t) \approx p_h(\boldsymbol{r}, t) + p_{sc}^{+}(\boldsymbol{r}, t), \tag{3.2.8}$$

or, in full notation:

$$p(\boldsymbol{r}, t) \approx \left[\sum_{i=1}^{\infty} \left(G_0 V_\gamma \right)^i G_0^{+} + G_0^{-} \right] q(\boldsymbol{r}', t'). \tag{3.2.9}$$

Ever since photoacoustic imaging has gained attention in research, a lot of work has been dedicated to suppress clutter artifacts. One approach relies on the assumption that scattered waves are of lower spatial coherence than direct photoacoustic waves and can hence be suppressed in a short-lag beamforming approach [7, 141]. Another way to distinguish between clutter and actual sources relies on decorrelation of the clutter signal by tissue deformation. The related approach is referred to as displacement compensated averaging (DCA) and tracks the displacements using ultrasound imaging [86, 89]. The differing shifts of direct and scattered waves during tissue deformation are also exploited in the LOVIT method, where the deformation is forced by an acoustic radiation force, either from an external transducer [85], or by the same transducer that records the photoacoustic measurement [137]. A decorrelation of clutter induced by variations in the illumination configuration is exploited in [132]. Recently, first investigations to train a neural network to distinguish between clutter and actual sources in a controlled simulation study with single point scatterers and point sources has been acquired [8].

None of the aforementioned approaches takes the actual scatterer distribution into account to create the forward model. In fact, since the actual scatterer distribution is generally unknown, a model incorporating the scattering process seems useless. However, information about the scatterers might be retrieved from additionally acquired ultrasound measurements. In the frame of this dissertation, the idea of incorporating information from plane wave ultrasound measurements to reduce clutter artifacts will be assessed (see chapter 6). A comparable method called PAFUSion was recently developed by Singh et al. and has already been shown to be applicable in vivo [158, 160]. In contrast to PAFUSion, the algorithm presented in in this dissertation is derived and operates in the spatial and temporal frequency domain, which allows for efficient computations. Also, an alternative approach with an actual inversion of the model instead of a subtraction of the estimated clutter will be presented (see chapter 6.3.2). The operation in the frequency domain also allows for the emission of less waves by an advanced interpolation method, which will be demonstrated in chapter 6.4. The benefit in computational effort might be an important step towards real time application.

4

Full Wave Reconstruction in Heterogeneous Media

The reconstruction methods introduced in chapter 3.2.1 all rely on a consideration of the full scattered wave during reconstruction of the photoacoustic sources. However, non of them was designed for a linear array and only a few consider a limited view.

The limited view is a major challenge for full wave reconstructions, since actual time reversal requires the waves from all directions to be back propagated into the tissue. Also, in a limited view scenario, part of the image information can be lost due to the fact that waves carrying the information about a certain structure might not be directed towards the transducer. The consideration of heterogeneities has a huge potential, as scattering might redirect the waves towards the transducer. Many algorithms do not differentiate between compressibility variations and density variations, which both contribute to scattering but differ in the directivity of the scattered wave.

Another issue is the impulse response, which incorporates the laser pulse shape and the electro-acoustic impulse response and which is usually not considered in the reconstruction. An appropriate treatment of the full impulse response is an essential feature when it comes to the performance of an algorithm in the presence of noise.

In this section, an iterative reconstruction method is introduced and assessed, that is based on a complex photoacoustic imaging model. The model considers variations in compressiblity and density as well as the full temporal impulse

response of the imaging setup. By analytically deriving an adjoint operator to the forward model operator, a Landweber iteration scheme is employed to find a solution to the inverse PA imaging problem. The derivation and elementary results were part of a Master's thesis [149]. The method has also been published in a conference article [150].

4.1 The Landweber Method

Let R be the operator mapping the photoacoustic sources p_0 onto the measurements p_m by $p_m = Rp_0$. An analytic solution of R was derived in chapter 3 (see (3.2.2)). A general Landweber iteration algorithm is derived by applying the adjoint operator R^* to both sides:

$$R^* p_m = R^* R p_0 \tag{4.1.1}$$

and rewriting it as fix point equation:

$$p_0 = p_0 - R^* (R p_0 - p_m). \tag{4.1.2}$$

By introducing a relaxation parameter α, this can be rewritten as an iterative algorithm with iteration index k:

$$p_0^{(k+1)} = p_0^{(k)} - \alpha R^* \left(R p_0^{(k)} - p_m \right), \tag{4.1.3}$$

which is called the Landweber iteration and equals the gradient descent that solves the respective least-squares problem. While R is a linear operator, a similar algorithm can be derived for non-linear operators using the adjoint of the Fréchet-derivative of the forward operator [139]. The Landweber iteration is regularizing in a sense that the inverse of the number of applied iterations k_{max} can be interpreted as regularization parameter $\lambda = 1/k_{max}$ [114, 139]. This section deals with an application of the Landweber method to the inverse photoacoustic imaging problem, including an analytic derivation for the adjoint operator as well as a description of the implementation.

4.1.1 Mathematical Framework and Theory

Let $p(\mathbf{r}, t)$ be the acoustic pressure at $\mathbf{r} = (x, z) \in \mathbb{R}^2$. Ω' is an open subset of the half-space $\Omega = \mathbb{R}^2 \backslash \{z \leq 0\}$ and is the solution domain for the inverse photoacoustic problem. On it's significant boundary at $\delta\Omega = \left\{ (x, z) \in \mathbb{R}^2 \middle| z = 0 \right\}$,

a transducer is located and positions on the transducer are described by the vector $\boldsymbol{r}_s = (x, 0)$. Variations of the propagation mediums mass density variation $\gamma_\rho(\mathbf{r})$ and compressibility variation $\gamma_\kappa(\mathbf{r})$ are restricted to $\Omega^{'}$ (see (2.1.17) for definition). A similar definition of the geometry was made in [75] for an ultrasound tomography reconstruction algorithm. The derivation of the Landweber method starts with the photoacoustic wave equation for heterogeneous media as presented in (2.1.21) (see derivation in chapter 2.1.3):

$$\Delta p(\boldsymbol{r}, t) - \frac{1+\gamma_\kappa}{c_0^2}\partial_{tt} p(\boldsymbol{r}, t) - \nabla \cdot \left(\gamma_\rho \nabla p(\boldsymbol{r}, t)\right) = -c_0^{-2} p_0(\mathbf{r}) \partial_t \eta(t) \quad (4.1.4)$$

Since the evolving field depends linearly on the source term, $\eta(t)$ can also contain the band-pass behavior of the transducer, even though, technically, the respective filtering is applied during the measurement and not during excitation. The source distribution p_0 is assumed to be restricted to the area Ω. An initial condition forces the wavefield to equal zero before the excitation starts and a boundary condition forces a rigid behavior of the transducer:

$$p(\mathbf{r}, t) = 0, \ \wedge \ \partial_t p(\mathbf{r}, t) = 0, (\mathbf{r}, t) \in \Omega \times \mathbb{R}^{<0}. \quad (4.1.5)$$

$$\nabla p(\boldsymbol{r}, t) \cdot \mathbf{n} = 0, (\mathbf{r}, t) \in \delta\Omega \times [0, T] \quad (4.1.6)$$

The equations (4.1.4)-(4.1.6) describe a time varying source problem with the restriction that the temporal and the spatial source terms are separable. Here, $\nabla p(\boldsymbol{r}, t) \cdot \mathbf{n}$ is the spatial derivative of p in normal direction to the detection line.

The problem to be solved is the reconstruction of the spatial source distribution $p_0(\mathbf{r})$, using the information gained by the actual measurement of the pressure $p_m(\mathbf{r}_s, t)$ on the sensor area. Therefore, the medium's heterogeneity distributions $\gamma_\rho(\mathbf{r})$ and $\gamma_\kappa(\mathbf{r})$ are considered to be known. The operator $R: \ L^2(\Omega) \longrightarrow L^2(\delta\Omega \times [0, T])$ maps a current source distribution $p_0(\mathbf{r})$ onto the respective measurement $p(\mathbf{r}_s, t)$, which is the solution of the time varying source problem in eqs. (4.1.4)-(4.1.6) .

$$R p_0 = p(\mathbf{r}_s, t) \quad (4.1.7)$$

The inverse operator R^{-1} could be applied on actual measurement data $p_m(\mathbf{r}_s, t)$ and would yield a direct solution of s. If R is ill-posed or not bijective, which is the case for an incomplete measurement with a linear array, a direct inversion is not feasible and a suitable $\hat{p}_0$ solution can be gained using the least-square-method:

$$\hat{p}_0 = R^* (R R^*)^{-1} p_m \quad (4.1.8)$$

with R^* being the adjoint operator to R.

Instead of solving (4.1.8), here, a Landweber optimization approach is suggested [105], where the adjoint operator is utilized to translate an error in the measurement to an error in the image. The forward propagation of a current estimation of p_0 and the backward propagation of the error are iterated, until the error is sufficiently small. Therefore, a random initial distribution $p_0^{(0)}$ is chosen and the recursive equation:

$$p_0^{(k+1)} = p_0^{(k)} + \alpha \cdot R^* \left[p_m - R p_0^{(k)} \right] \tag{4.1.9}$$

is applied, where α is a relaxation factor that needs to be determined empirically. The term $[p_m - R p_0]$ describes the error of the measurement and the application of R^* maps the error of the measurement to an error in the image space. The adjoint operator R^* is derived in the next section. The initial distribution $p_0^{(0)}$ was chosen to be $p_0^{(0)}(\mathbf{r}) = 0$ in Ω for all following experiments. Note that the relaxation factor can also depend on the iteration step, as well as on space and then reads as $\alpha_k(\mathbf{r})$. In [114] a linear decrease over time is suggested.

4.1.2 The Adjoint Operator

The adjoint operator R^* reads as:

$$(R^* p(\mathbf{r}_s, t))(\mathbf{r}) = c_0^{-2} \int_0^T Z(\mathbf{r}, t) \partial_t \eta(t) dt \tag{4.1.10}$$

where $Z(\mathbf{r}, t)$ is an auxiliary field, which meets the conditions of the following final value problem:

$$\Delta Z(\boldsymbol{r}, t) - \tfrac{1+\gamma_\kappa}{c_0^2} \partial_{tt} Z(\boldsymbol{r}, t) - \nabla \cdot \left(\gamma_\rho \nabla Z(\boldsymbol{r}, t) \right) = 0 \tag{4.1.11}$$

$$Z(\mathbf{r}, t) = 0 \ \wedge \ \partial_t Z(\mathbf{r}, t) = 0, (\mathbf{r}, t) \in \Omega \times \mathbb{R}^{>T} \tag{4.1.12}$$

$$\nabla Z(\boldsymbol{r}_s, t) \cdot \mathbf{n} = p(\boldsymbol{r}_s, t), (\boldsymbol{r}_s, t) \in \delta\Omega \times [0, T] \tag{4.1.13}$$

where $\mathbf{n}$ is the normal vector on the detection area. Eqs. (4.1.11) - (4.1.13) constitute a final value problem. The boundary condition (4.1.13) expresses that the spatial derivative of the field Z normal to the sensor area equals the measurement data. Note that the field Z fulfills the homogeneous acoustic wave equation for inhomogeneous media, but does not represent a pressure,

since, according to (4.1.13), it has the dimension of pressure multiplied by length. It must be seen as a mathematical construct that serves as an auxiliary field to allow for a computation of the adjoint operator R^*.

The derivation of R^* is accomplished via the definition for adjoint operators:

$$\langle R^* p,\, p_0\rangle_{L^2(\Omega)} = \langle p,\, R\, p_0\rangle_{L^2(\delta\Omega\times[0,T])} \tag{4.1.14}$$

where $\langle A, B\rangle$ signifies the inner product in the respective space. For arbitrary functions p, Z on $\Omega\times[0,T]$ the following identity has been proven (compare equation (A.8) in [75] with the arbitrary functions w and z) :

$$\begin{aligned}
&\int_0^T\int_\Omega\left(\Delta p(\boldsymbol{r},t)-\frac{1+\gamma_\kappa}{c_0^2}\partial_{tt}p(\boldsymbol{r},t)-\nabla\cdot\big(\gamma_\rho\nabla p(\boldsymbol{r},t)\big)\right)Z(\mathbf{r},t)\,d\mathbf{r}dt\\
=\;&\int_0^T\int_\Omega\left(\Delta Z(\mathbf{r},t)-\frac{1+\gamma_\kappa}{c_0^2}\partial_{tt}Z(\boldsymbol{r},t)-\nabla\cdot\big(\gamma_\rho\nabla Z(\boldsymbol{r},t)\big)\right)p(\boldsymbol{r},t)\,d\mathbf{r}dt\\
&+\int_0^T\int_{\delta\Omega}\big(1-\gamma_\rho\big)\big(p(\boldsymbol{r},t)\nabla Z(\boldsymbol{r},t)\cdot\mathbf{n}-Z(\boldsymbol{r},t)\nabla p(\boldsymbol{r},t)\cdot\mathbf{n}\big)\;dS(\mathbf{r})dt\\
&+\int_\Omega\frac{1+\gamma_\kappa}{c_0^2}\left[p(\boldsymbol{r},t)\partial_t Z(\boldsymbol{r},t)-Z(\boldsymbol{r},t)\partial_t p(\boldsymbol{r},t)\right]_0^T d\mathbf{r}
\end{aligned}\tag{4.1.15}$$

Using the definition of p and Z in (4.1.4)-(4.1.6) and (4.1.11)-(4.1.13), and the fact that γ_ρ vanishes on the boundary, (4.1.15) reduces to

$$\int\int Z(\mathbf{r},t)\partial_t\eta(t)\;dt\cdot c_0^{-2}p_0(\mathbf{r})\;d\mathbf{r}=\int\int p(\mathbf{r},t)\nabla Z\cdot\mathbf{n}\;dS(\mathbf{r})dt \tag{4.1.16}$$

$$\Rightarrow\left\langle\int_0^T Z(\mathbf{r},t)\partial_t\eta(t)dt,\, c_0^{-2}p_0(\mathbf{r})\right\rangle=\langle p(\mathbf{r}_s,t),\,\nabla Z\cdot\mathbf{n}\rangle \tag{4.1.17}$$

Substituting (4.1.7) and (4.1.13) and comparing this to (4.1.14), the adjoint operator $R^*(\mathbf{r})$ reads as:

$$\boxed{R^*p=c_0^{-2}\int_0^T Z(\mathbf{r},t)\partial_t\eta(t)dt} \tag{4.1.18}$$

4.1.3 Implementation

The Landweber reconstruction algorithm was implemented in Matlab, while both forward and back propagation are realized as pseudo spectral acoustic wavefield simulations using the k-wave toolbox [14]. The data flow of the

Landweber iteration for PA data is visualized in Fig. 4.1.1. The algorithm requires the photoacoustic measurement data $p_m(x,t)$, the acoustic medium properties $\gamma_\kappa(\boldsymbol{r})$ and $\gamma_\rho(\boldsymbol{r})$ and an initial estimation of the source distribution $\hat{p}_0^{(0)}(\boldsymbol{r})$ as input, while $\hat{p}_0^{(0)}(\boldsymbol{r})$ does not require a-priori knowledge and can be a zero distribution. The algorithm starts with a forward propagation of $\hat{p}_0^{(0)}(\boldsymbol{r})$, generating the estimated measurement data $\hat{p}_m$. Subtracting $\hat{p}_m$ from the actual measurement p_m yields the error in the space of measurements $p_m^{(err)}$. The error is temporally reversed and employed as source to the back propagation generating the auxiliary field $Z(\boldsymbol{r},t)$. The field Z is temporally back-reversed and the inner product over Z and the temporal derivative of the impulse response over time yields the update term Δp_0, which is scaled by the scalar relaxation factor α and added to the current estimation of the PA source $\hat{p}_0$. This procedure is repeated in each iteration and the final result for $\hat{p}_0$ is the final reconstruction result. The iteration can be terminated after a fix number of iterations or when the measurement error reaches a threshold.

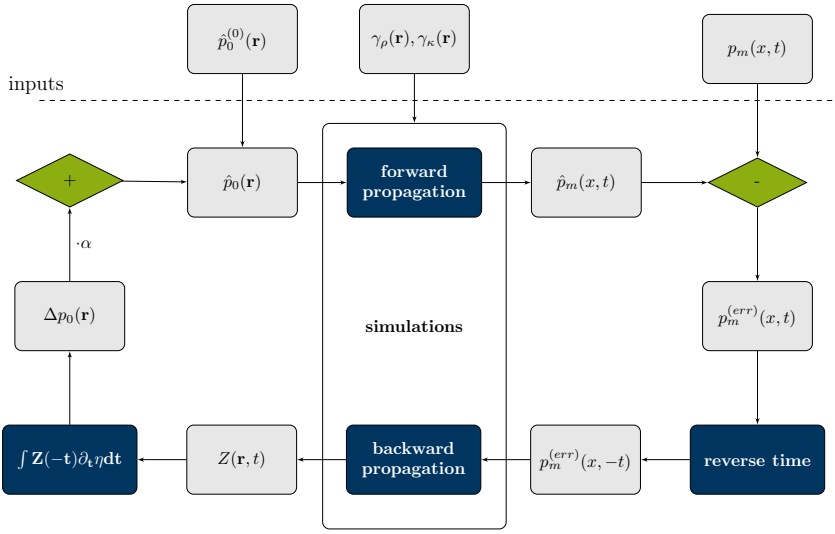

Figure 4.1.1: Flow chart showing the Landweber reconstruction

Computation of the Forward Propagation

For the forward simulation, a time varying pressure source problem with the impulse response $\eta(t)$ as temporal excitation is solved by k-wave. To attain a simulation grid that is completely independent of the transducer characteristics, the entire first row of the solution grid is read out as sensor and the actual channel data is retrieved by interpolation. Therefore, the sensor data set is resampled to the temporal grid of the measurement data by upsampling using zero padding in the frequency domain and a linear interpolation of the up-sampled data at the time steps defined by the acquisition delay and the sampling frequency of the actual measurement. Spatial resampling is accomplished by applying the inner product of the sensor data $p_{sim}(x, z = 0, t)$ and a rect-function with the shape of the respective transducer element, such that

$$\hat{p}_m(x_i, t) \quad = \int p_{sim}(x, z = 0, t)\mathrm{rect}\left((x_i - x)/\Delta e\right) dx \tag{4.1.19}$$

where x_i is the location of the i-th of N_{el} transducer elements and Δe is the element width.

For an accurate computation, the rect-function has to be analytically low-pass filtered before it can be discretized according to the Nyquist theorem. This is especially required, since the width of one element Δe is not necessarily a multiple of the sample width Δx and the transducer elements might not be centered on the simulation grid. The low-pass filtered version of the rect-function $\mathrm{rect}_{\mathrm{lo}}$ with discretization width Δx and element width Δe calculates as:

$$\begin{aligned}
\mathrm{rect}_{\mathrm{lo}}(x, \Delta x, \Delta e) \quad &= \mathrm{rect}(x/\Delta e) * \mathrm{sinc}(x/\Delta x) \\
&= \textstyle\int_{-\infty}^{\infty} \mathrm{rect}(x'/\Delta e)\mathrm{sinc}((x - x')/\Delta x)dx' \\
&= \textstyle\int_{-\Delta e/2}^{\Delta e/2} \mathrm{sinc}((x - x')/\Delta x)dx' \\
&= -\Delta x \textstyle\int_{(x+\Delta e/2)/\Delta x}^{(x-\Delta e/2)/\Delta x} \mathrm{sinc}(\tilde{x})d\tilde{x} \\
&= \Delta x \cdot \mathrm{sinint}((x + \Delta e/2)/\Delta x) \\
&\quad - \Delta x \cdot \mathrm{sinint}((x - \Delta e/2)/\Delta x),
\end{aligned} \tag{4.1.20}$$

using the sine integral function $\mathrm{sinint}(x) = \int_0^x \sin(x')/x' dx'$.

Computation of the Backward Propagation

The backward propagation that creates the auxiliary field $Z(\boldsymbol{r},t)$ is implemented as a final value problem according to (4.1.11) - (4.1.13). A pressure source is defined at the transducer line and the spatial derivative is accounted for by a finite difference approximation of order one:

$$\frac{Z(x,z=\Delta z,t)-Z(x,z=0,t)}{\Delta z} \approx p_m^{(err)}(x,t) \tag{4.1.21}$$

Solving (4.1.21) for $Z(x,z=0,t)$, a Dirichlet boundary condition in dependence on the current field can be applied by forcing the pressure value at $z=0$ to be dependent on the current pressure value at the consecutive pixel in axial direction at $z=\Delta z$:

$$Z(x,z=0,t) \approx -Z(x,z=\Delta z,t)-p_m^{(err)}(x,t)\Delta z \tag{4.1.22}$$

A similar approach was used for back propagation in [75]. The fact that the first order finite difference in (4.1.21) is centered in $\Delta z/2$ leads to an increasing displacement of the field over iterations, which can be accounted for by reading out the field Z at an offset of $\Delta z/2$ by interpolation.

Like in the forward propagation, a conversion from the array data of the measurement error $p_m^{(err)}$ to source data of the simulation $p_{sim}^{(err)}$ is required, since the respective grids are not necessarily equal. Again, the temporal resampling is acquired by upsampling in the frequency domain and linear interpolation. The spatial resampling is performed by computing a weighted sum over all rect-functions that determine the shape of the transducer elements. These rect-functions are summed up and weighted by the pressure value in the respective channel at the current time step:

$$p_{sim}^{(err)}(x,t) \quad = \sum_{i=1}^{N_{el}} p_m^{(err)}(x_i,t)\mathrm{rect}_{\mathrm{lo}}((x-x_i)/\Delta e) \tag{4.1.23}$$

Computation of the Update Term

The update is calculated by the application of the adjoint operator to the error in the space of measurements according to (4.1.9). Since the field $Z(\boldsymbol{r},t)$ is excited by a finite difference that is centered at $z=\Delta z/2$ (see (4.1.21)), Z has to be shifted by Δz to ensure an exact mapping, which is accomplished by linear interpolation between subsequent pixels in axial direction. Instead of differentiating $\eta(t)$ over time (see (4.1.18)), the auxiliary field Z is differentiated over time. Applying the derivative to Z instead of η is

valid if the negative value of the resulting update term Δp_0 is used, due to the following relation:

$$\begin{aligned}\int Z(t)\partial_t\eta(t)dt &= \int \partial_t(\eta(t)Z(t))\,dt - \int \eta(t)\partial_t Z(t)dt \\ &= [Z(t)\eta(t)]_{-\infty}^{\infty} - \int \eta(t)\partial_t Z(t)dt \\ &= -\int \eta(t)\partial_t Z(t)dt,\end{aligned} \tag{4.1.24}$$

which is the case for finite time impulse responses with $\eta \to 0$ for $t \to \pm\infty$. The derivative is computed as a first order finite difference over two temporal samples by:

$$\partial_t Z(t) \approx \frac{Z(t+\Delta t) - Z(t-\Delta t)}{\Delta t} \tag{4.1.25}$$

such that the differentiated quantity is centered at t. Due to numerical problems of the wavefield near the sensor line, the first 10 axial rows of the update term are set to 0 to assure convergence. The relaxation factor α is determined empirically and the optimal choice might vary with the measurement setup and the phantom's complexity.

4.2 Reconstruction with Known Heterogeneities

In a first step, the theoretical capabilities of the method to improve photoacoustic images are stressed. The heterogeneities are assumed to be known during the photoacoustic reconstruction, such that possible inaccuracies can directly be assigned to the algorithm and not imperfect heterogeneity data. All measurements in this section were acquired by numeric simulations providing absolute ground truth information about the heterogeneities and the actual PA source distribution. After investigating general properties in terms of the improvement of resolution and the recovery of lateral image features, the capabilities to deal with noise and, finally, the impact in a realistic clinical scenario are assessed.

4.2.1 Assessment of General Capabilities

By considering the acoustic heterogeneities and the system's temporal impulse response, the resolution of a Landweber reconstruction is expected to outperform the resolution of a standard reconstruction. In addition, the Landweber iteration might even be able to restore structures that would not have been measured by a limited view detector without scattering. Both of these features are assessed in this section using dedicated numerical phantoms.

Resolution

In order to quantitatively determine the benefit of the Landweber method in comparison to a standard reconstruction that does not consider acoustic heterogeneities, measurements of a numerical phantom were simulated using the pseudo-spectral simulation environment k-wave [14]. The properties of the simulation are gathered in table 4.2.1. The numerical phantom comprises three photoacoustic point sources that are arranged in a triangle, such that a lateral profile and an axial profile through two sources can easily be obtained in order to derive a measure for the resolution (see Fig. 4.2.1). The point sources, which have the size of one pixel, are embedded in a randomly varying SOS distribution with a Gaussian distribution and 5% standard deviation. The blue rectangle in the speed-of-sound distribution signifies the region of interest (ROI) of the sources that is magnified in Fig. 4.2.1-a.

Property	Value	Unit
grid size	256×256	pixels
grid area	29.9×29.9	mm^2
center frequency	2	MHz
fractional bandwidth	78	%
transducer elements	216	
pitch	1.389	mm
kerf	0	mm
laser pulse FWHM	1	ns

Table 4.2.1: Simulation properties for the “point-source” phantom

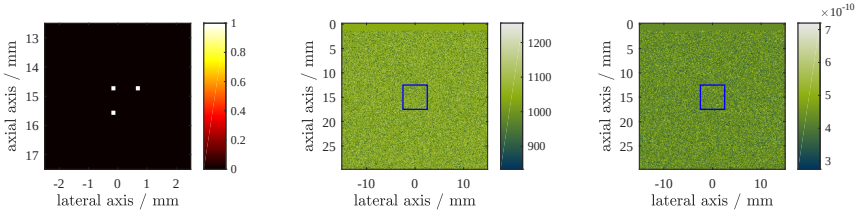

(a) $p_0(\boldsymbol{r})$ (b) $\rho(\boldsymbol{r})$ (c) $\kappa(\boldsymbol{r})$

Figure 4.2.1: Numerical "resolution" phantom, PA source distribution (a), mass density distribution (b), compressibility distribution (c)

As the image mainly consists of point sources, it can be used to assess the spatial resolution of the reconstruction. Besides diffraction limitations due to the limited view and blurring of the structures that can be assigned to scattering, the temporal impulse response $\eta(t)$ is the dominating factor affecting the spatial resolution. The impulse response of this simulated imaging system is a combination of the temporal laser pulse shape and the electro-acoustic impulse response of the transducer and is depicted in both time and frequency domain in Figure 4.2.2. According to the PA k-space relation (see (2.2.4)), one temporal frequency of the measurement data correspond to the magnitude of the frequency vector in the PA source distribution. Hence, the temporal bandwidth of the impulse response is mapped on a ring in the reconstructed image. For that reason, the wavenumbers corresponding to the−6 dB band limit of the impulse response are plotted into the following image spectra of the reconstruction results to provide insights on the capability of a reconstruction method to recover suppressed frequencies.

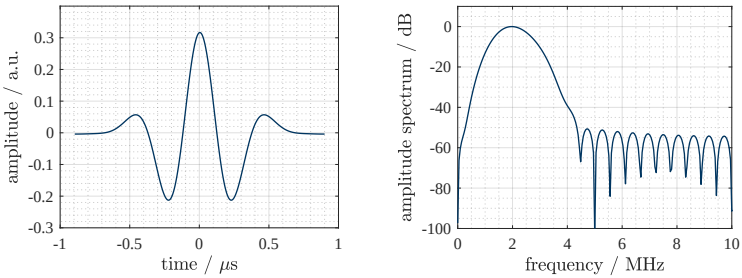

(a) (b)

Figure 4.2.2: Impulse response $\eta(t)$ and transfer function $\eta(\omega)$ - point source

Figure 4.2.3 shows the reconstruction results in the same ROI around the point sources as the phantom in Figure 4.2.1 was depicted. The results of a standard reconstruction that does not consider the medium properties are compared to the results of the Landweber method after one and 10,000 iterations on a linear intensity scale before envelope detection. Looking at the space domain images, a blurring and distortions of the point sources can be recognized in the reference reconstruction, while the location of the sources seems to be accurately recovered by the Landweber method. After one iteration, the sources are locatable but still appear blurred. After 10,000 iterations, most of the intensity is concentrated onto the pixels of the actual point sources. Looking at the image spectra, the image content of the reference reconstruction decays strongly outside the band limits and the damping is even stronger in the Landweber reconstruction after one iteration. This can be explained by the adjoint in (4.1.18) acting as a filter on the wavefield with the derivative of the impulse response, which generally lowers the spatial resolution. However, it can be seen that lateral frequencies, which are strongly damped in the reference reconstruction, are restored even after one iteration. After 10,000 iterations, the intensity in strongly damped frequency regions far beyond the -6 dB limit in both axial and lateral direction indicate a recovery of information that was assumed to be lost or at least strongly attenuated during the measurement process.

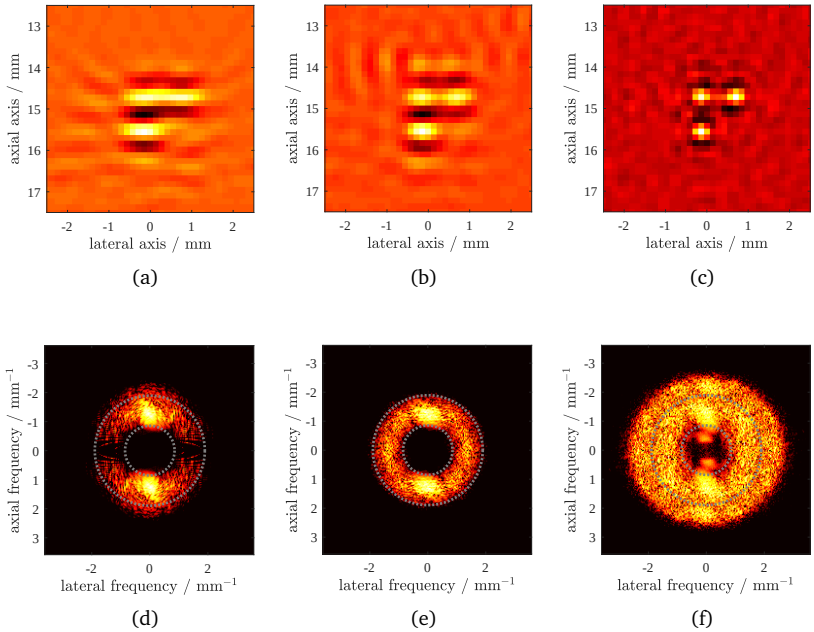

Figure 4.2.3: Reconstruction results of the “point-source” phantom in space and spatial frequency domain; standard reconstruction (a,d), Landweber reconstruction after 1 iteration (b,e), Landweber reconstruction after 10.000 iterations (c,f), Dynamic Range of log-compressed spectra: 30 dB

Figure 4.2.4 shows the lateral and axial profiles through the two respective point sources on a linear scale after envelope detection in comparison to the reference reconstruction and the Landweber reconstruction after 10,000 iterations. In both directions, the two sources cannot be separated at all in the reference reconstruction, whereas the Landweber methods results in clearly distinguishable peaks with dips of −11.1 dB in axial direction and −14.0 dB in lateral direction compared to their respective maximum values.

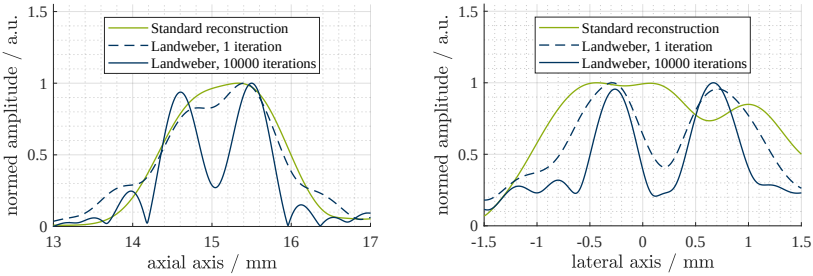

(a) (b)

Figure 4.2.4: Axial (a) and lateral (b) profiles - point source

Limited View Compensation

Apart from an improved resolution, another question that is assessed is in how far artifacts associated with the limited view can be omitted by considering scattering in the reconstruction. A source distribution in the shape of a circular disc is depicted in Figure 4.2.5-a. Lateral boundaries of the disc source propagate into lateral direction and, hence, the respective wave fronts are not measured by the limited size aperture described (see properties in table 4.2.2). However, it can be expected that the speed-of-sound distribution depicted in Figure 4.2.5-b, which consists of one tilted transition from one SOS to another SOS, might redirect those wave fronts toward the transducer due to reflection. In that case, the image quality could actually benefit from heterogeneous media, since information that seems to be not contained in the measurement data can actually be recovered.

Property	Value	Unit
grid size	256 × 256	pixels
grid area	29.9 × 29.9	mm^2
center frequency	2	MHz
fractional bandwidth	50	%
transducer elements	216	
pitch	1.389	mm
kerf	0	mm

Table 4.2.2: Simulation properties for the “disc-source”-phantom

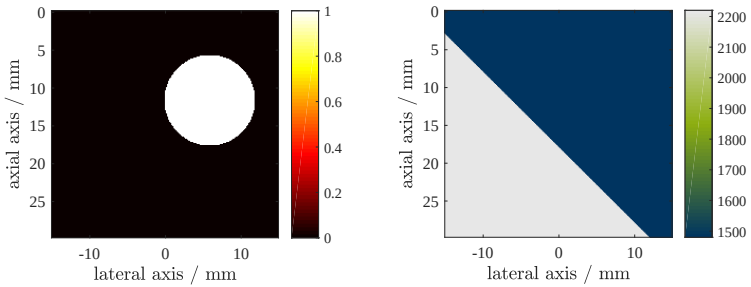

Figure 4.2.5: Numerical “disc-source” phantom; PA source (a), SOS (b)

Figure 4.2.6 shows the respective reconstruction results of the standard reconstruction, again in comparison to the Landweber reconstruction after one and after 10,000 iterations. In fact, the lateral boundaries appear to be clearly visible in the Landweber reconstruction after one iteration and the boundaries become sharper during the iteration process. In addition, the scattering artifact, which seems to mirror the disc at the SOS boundary, is gone. However, there is still another reflection artifact, which refers to that part of the wave that is transmitted through the SOS boundary during back propagation. The amplitude of this new artifact is reduced within 10,000 iterations, but cannot be completely eliminated.

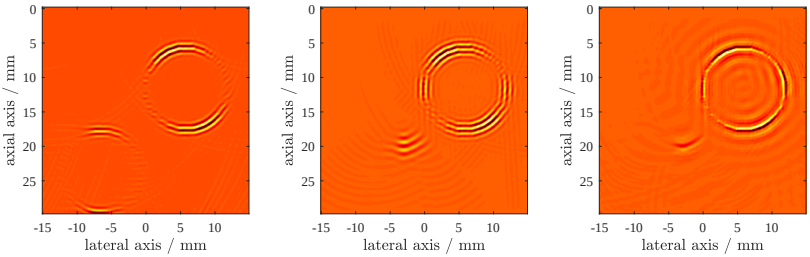

(a) (b) (c)

Figure 4.2.6: Reconstruction results of the “disc-source” phantom; standard reconstruction (a), Landweber reconstruction after 1 iteration (b), Landweber reconstruction after 10.000 iterations (c)

4.2.2 The Impact of Noise

In the absence of noise, a recovery of suppressed spatial frequencies can be achieved by filtering with the inverse of the impulse response $\eta(t)$. Hence, to state a benefit of the Landweber method, a comparison of the reconstruction results of measurement data corrupted by noise in inevitable. As first step on the way to a fair comparison of noisy data, the performance of the Landweber method is assessed on non-noisy but strongly band limited data. This was achieved by the application of an impulse response that does not exhibit a Gaussian spectrum, but is cropped at the −6 dB limits in the frequency domain. The respective impulse response and the spectrum are depicted in Figure 4.2.7. The main purpose of this study is to verify, if any effect during the reconstruction might be able to recover spatial frequencies that have not been transferred by the wave, for example by the scattering of evanescent waves during the excitation.

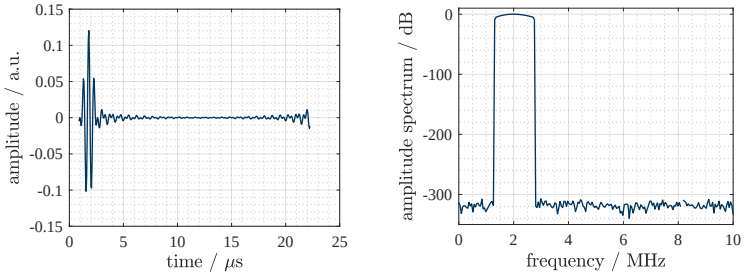

(a) (b)

Figure 4.2.7: Impulse response $\eta(t)$ (a) and transfer function $\eta(\omega)$ (b) for a strongly band limited measurement

Again the reconstruction results are depicted in space domain and in spatial frequency domain (see Fig. 4.2.8). Now, all results are within the absolute band limits, even after 10,000 iterations. A difference can only be stated in the lateral frequencies, which can still be recovered using the Landweber iteration. However, this comparison shows that the Landweber method cannot recover frequencies that are completely suppressed during the measurement. This is supported by the line profiles in Figure 4.2.9, where the lateral resolution can be strongly improved by the Landweber method, but the axial resolution is in the range of the axial resolution of the standard reconstruction. As expected, the Landweber iteration fails to recover spatial frequencies that have not been propagated as wave and the increase of resolution in Figure 4.2.3 can only be assigned to an amplification of damped frequencies. This implies that, in the presence of noise, it cannot be expected that image features of frequencies way below the noise level can be correctly recovered. If the bandwidth of images reconstructed from noisy data is increased, this means that the Landweber method is rather a powerful noise filter but does not conquer the resolution limit.

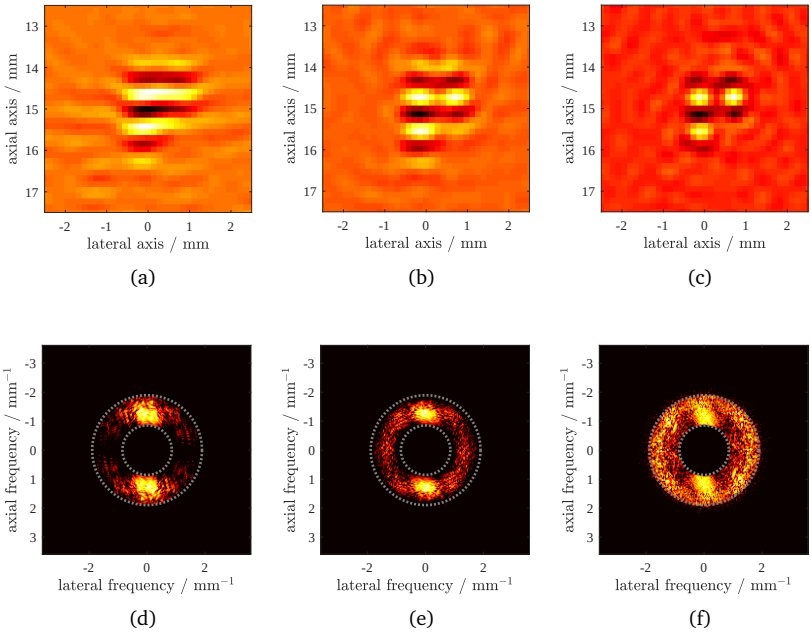

Figure 4.2.8: Reconstruction results of the “point-source” phantom in space domain and spatial frequency domain for a strongly band limited impulse response; standard reconstruction (a,d) , Landweber reconstruction after 1 iteration (b,e), Landweber reconstruction after 10.000 iterations (c,f), Dynamic Range of log-compressed spectra: 20 dB

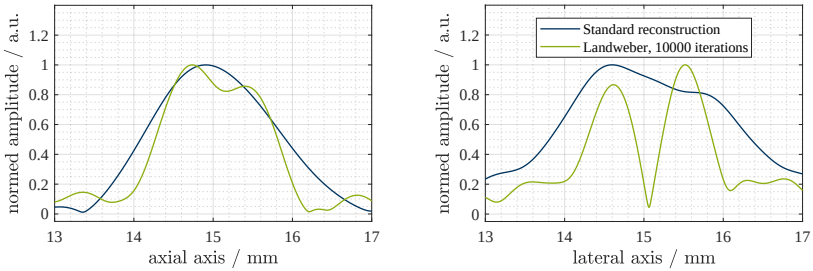

(a) (b)

Figure 4.2.9: Axial (a) and lateral (b) profiles - point source with strongly band limited impulse response

Now, the original impulse response is employed, but the measurement data is corrupted by Gaussian noise with a peak signal to noise ratio (PSNR) of −30 dB, meaning the square of the highest value in the actual signal is at 3.16% of the noise power. The point sources cannot be seen at all in the standard reconstruction (see Figure 4.2.10). The images of the Landweber reconstruction are very noisy, but in principle, the general shape of the point sources can still be recovered. The improvement over iterations is very small, but the spectra suggest a significant improvement in spatial resolution. The increase of bandwidth of previous results without noise in Figure 4.2.3, however, cannot be reached any more. These results might demonstrate that the Landweber method is an effective tool for noise compensation, as it amplifies frequencies that are slightly damped but suppresses frequencies that are dominated by noise.

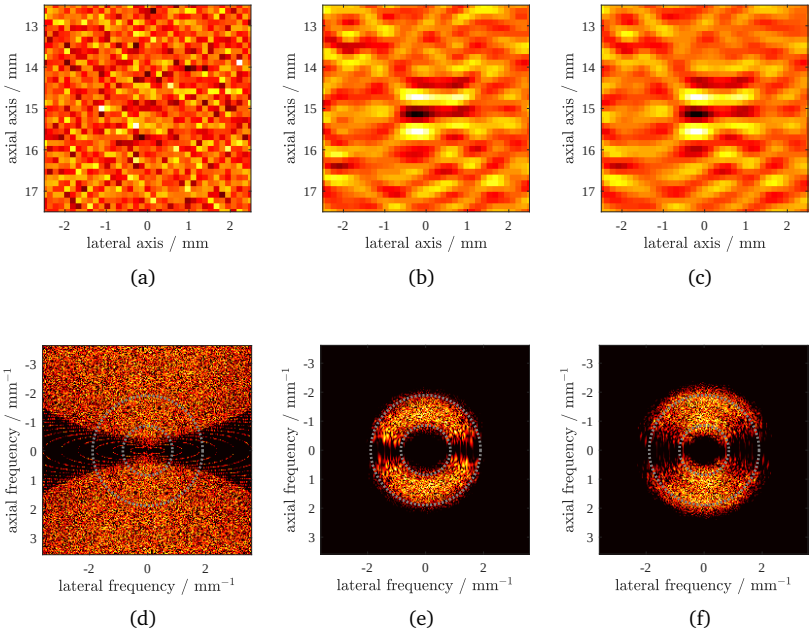

Figure 4.2.10: Reconstruction results of the "point-source" phantom in space domain and spatial frequency domain for noisy data (PSNR −30 dB); standard reconstruction (a,d) , Landweber reconstruction after 1 iteration (b,e), Landweber reconstruction after 10.000 iterations (c,f), Dynamic Range of log-compressed spectra: 20 dB

However, for a fair comparison, it should be considered that the knowledge about the impulse response can also be exploited in the standard reconstruction by spectral filtering of the measurement data. The Filter kernel that minimizes the square error in the restoration of noisy filtered data is the Wiener Deconvolution filter H_W, which is defined as [118, p.107]:

$$H_W(\omega) = \frac{1}{\eta(\omega)} \frac{|\eta(\omega)|^2}{|\eta(\omega)|^2 + \frac{P_n(\omega)}{P_s(\omega)}} \tag{4.2.1}$$

with $P_n(\omega)$ being the spectral noise power density and $P_s(\omega)$ being the spectral signal power density. A comparison between the Landweber reconstruction results and a standard reconstruction after a Wiener deconvolution of the measurement data was conducted in order to provide an estimate of the capabilities of noise suppression during the Landweber reconstruction. To neglect the impact of aberrations to the resolution, the following simulations were acquired in a homogeneous acoustic background with $c(\boldsymbol{r}) = 1480\,\mathrm{m/s}$ and $\rho(\boldsymbol{r}) = 1040\,\mathrm{m}^{-3}$. It should be noticed that, in this case, the spectral densities $P_n(\omega)$ and $P_s(\omega)$ can be exactly determined by determining the spectrum of the noise free simulation data and the spectrum of the added noise for each channel. In actual imaging scenarios, however, both $P_n(\omega)$ and $P_s(\omega)$ need to be estimated based only on noisy measurement data. In consequence, the application of the Wiener filter requires a-priori knowledge and the respective results must be seen as an upper limit of what actual filtering might be able to achieve.

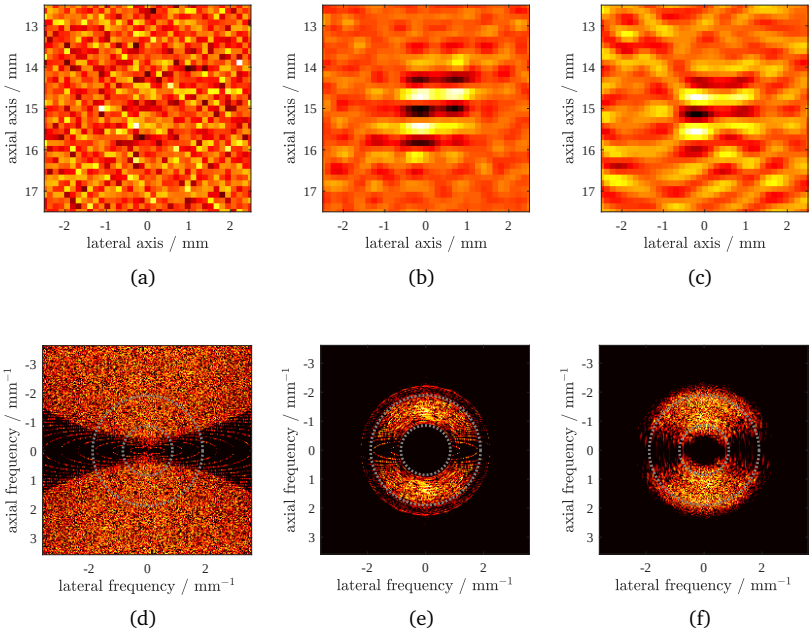

Figure 4.2.11: Reconstruction results of the “point-source” phantom in space domain and spatial frequency domain for noisy data (PSNR −30 dB); standard reconstruction (a,d), standard reconstruction with prior Wiener deconvolution (b,e), Landweber reconstruction after 10.000 iterations (c,f), Dynamic Range of log-compressed spectra: 20 dB

The reconstruction results of the standard reconstruction with and without prior Wiener deconvolution are depicted in Figure 4.2.11-(a,d) and in Figure 4.2.11-(b,e), respectively. In both the image after Wiener deconvolution and the Landweber image, spatial frequencies beyond the −6 dB limit are visible. The results of the Landweber reconstruction seem to exhibit more noise. However, the line profiles in Figure 4.2.12 indicate that the spatial resolution of the Landweber method is highly competitive with an ideal Wiener deconvolution. Axially, the Landweber method seems to outperform the standard reconstruction with Wiener deconvolution. In lateral direction, a comparison

is difficult to make, but the two results are fairly similar.

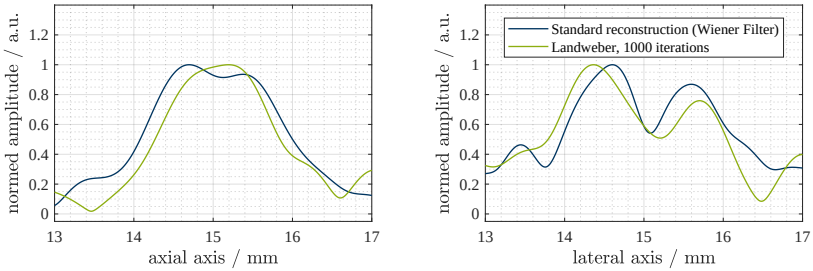

(a) (b)

Figure 4.2.12: Axial (a) and lateral (b) profiles (Wiener) - point source and noisy data

4.2.3 Performance Using Realistic Properties

For now, all phantoms were designed to investigate a specific property of the reconstruction algorithm. However, the source distributions were quite unrealistic in order to provide information about the application of the Landweber method to clinical measurement data. To prove a benefit of the method in realistic tissue properties, the carotid artery phantom that was described in chapter 2.4, and is also depicted in Figure 4.2.13, was used for a simulation and reconstructed with a standard reconstruction and the Landweber reconstruction. The respective simulation properties are listed in table 4.2.3.

Property	Value	Unit
grid size	256×256	pixels
grid area	29.9×29.9	mm^2
center frequency	2	MHz
fractional bandwidth	78	%
transducer elements	96	
pitch	0.245	mm
kerf	0.049	mm
laser pulse FWHM	1	ns

Table 4.2.3: Simulation properties for the “carotid-artery” phantom

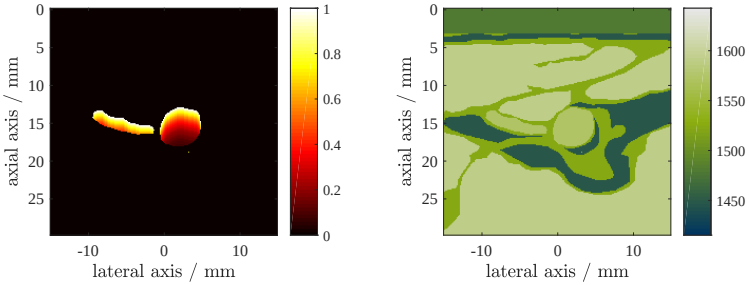

Figure 4.2.13: Numerical “carotid artery” phantom; photoacoustic source distribution (a), speed-of-sound distribution (b)

The respective reconstruction results are depicted in Figure 4.2.14. The images are displayed on a linear scale before envelope detection. The Landweber reconstruction succeeds in mapping the boundaries to the correct locations, while the standard reconstruction yields distorted image features. Also, a significant recovery of bandwidth can be stated, which becomes obvious, for example by the fact that the lumen of the vene is filled out instead of only showing the boundaries. It is even possible to see the signal decay within the vessels due to the decreasing fluence, that can also be seen in the original phantom.

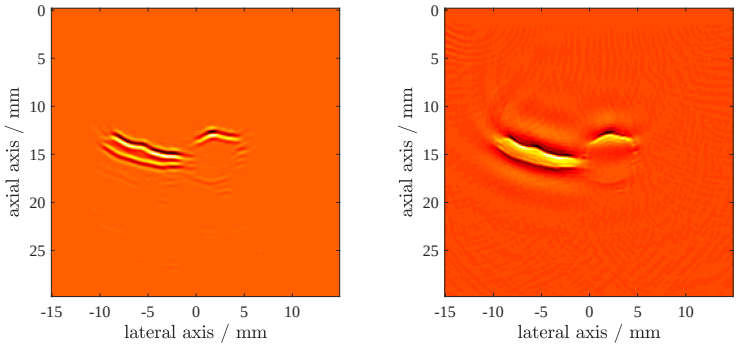

Figure 4.2.14: Landweber reconstruction results for the carotid artery phantom; standard reconstruction (a), Landweber reconstruction after 10,000 iterations (b)

4.3 Reconstruction with Estimated Heterogeneities

While the previous studies focused on general properties of the Landweber method and assumed the heterogeneity distributions to be exactly known within the reconstruction, this section addresses the applicability of the Landweber reconstruction to clinically relevant scenarios, where the speed-of-sound distribution is not exactly known, but might be estimated. In general, as pointed out in chapter 3.2.1, ultrasound imaging is a promising tool to derive information about the acoustic properties and many PA systems allow for the additional acquisition of ultrasound images. However, it can generally be expected that the results from reconstruction algorithms that derive medium properties are imperfect. Therefore, the first study in this section will be dedicated to the question in how far degradations of the acoustic heterogeneity distribution harm the reconstruction results of the Landweber reconstruction. This is assessed by actively blurring and misplacing the actual heterogeneity distribution. In a second experiment, again based on simulation data of the numerical carotid artery phantom (see Figure 4.2.13), the performance

of the Landweber reconstruction is assessed when the heterogeneity distributions are acquired from reflection mode ultrasound measurements using a non-linear iterative ultrasound reconstruction method [75]. Just like the Landweber method, the non-linear ultrasound reconstruction is based on an iterative scheme, where the image is updated by a numerically computed pair of forward and adjoint operators. However, here, two parameters are reconstructed, which are the relative medium properties for compressibility γ_κ and density γ_ρ. Since the dependence of the measured wave on the medium properties is not linear, the forward operator was differentiated using a Fréchet derivative before the determination of the adjoint operator, which has also been demonstrated in [129, 130]. Finally, since, in ultrasound imaging, the wave excitation can be varied and an US measurement comprises a set of US measurements in the same medium for different incoming waves, the optimization is realized as a Kaczmarz method, where the individual measurements are randomly permuted and an update is calculated for each measurement instead of optimizing the whole forward problem at once before updating [139]. The two adjoint operators for compressibility $R_\kappa^{'*}$ and density $R_\rho^{'*}$ read as:

$$\begin{aligned}\left(R_\kappa^{'*} p_m^{(us)}\right)(\boldsymbol{r}) = &\quad + \int_0^T c_0^{-2} Z^{(us)}(\boldsymbol{r},t)\partial_{tt} p^{(us)}(\boldsymbol{r},t)dt \\ \left(R_\rho^{'*} p_m^{(us)}\right)(\boldsymbol{r}) = &\quad - \int_0^T \nabla Z^{(us)}(\boldsymbol{r},t)\cdot\nabla p^{(us)}(\boldsymbol{r},t)dt\end{aligned} \tag{4.3.1}$$

where $p_m^{(us)}$ is the ultrasound measurement data, $p^{(us)}$ the respective ultrasound wavefield and $Z^{(us)}(\boldsymbol{r},t)$ is an auxiliary field that is defined exactly as $Z(\boldsymbol{r},t)$ in (4.1.11) - (4.1.13) in relation to $p^{(us)}$. The update is calculated by back propagating the current error in the space of measurements via the adjoint operators and adding the result to the current estimation of the medium parameters:

$$\begin{aligned}\hat{\gamma}_{i+1}^\kappa = &\quad \hat{\gamma}_i^\kappa + \alpha_\kappa R_\rho^{'*}(\hat{p}_{m,i}^{(us)} - p_m^{(us)}) \\ \hat{\gamma}_{i+1}^\rho = &\quad \hat{\gamma}_i^\rho + \alpha_\rho R_\rho^{'*}(\hat{p}_{m,i}^{(us)} - p_m^{(us)})\end{aligned}\ . \tag{4.3.2}$$

Here, $\hat{\gamma}_i^\kappa$ and $\hat{\gamma}_i^\rho$ are the estimations of the compressibility variation and the density variation in the i-th iteration and $\hat{p}_{m,i}^{(us)}$ is the forward propagation in the current medium properties. α_κ and α_ρ are the relaxation parameters that need to be found empirically. A detailed description of the entire method can be found in [74].

4.3.1 The Limits of Reconstruction in Estimated Heterogeneities

The first experiment assesses the robustness of the Landweber reconstruction to false heterogeneity maps. As it can be assumed that heterogeneity maps derived from ultrasound images will never be exact, in this experiment the actual SOS distribution that has been used to generate PA measurement data is manipulated and the effect on the Landweber reconstruction results is evaluated. Two scenarios are investigated, a misplaced SOS distribution and a blurred SOS distribution. Again, to be able to accurately interpret the results, a simple numerical phantom is chosen that matches the one in Figure 4.2.5, comprising a disc-shaped source distribution and a single tilted SOS transition. The original SOS distribution and the two distorted distributions are depicted in Figure 4.3.1. The shift is in the order of the center wavelength ($0.94\lambda_c$) and the blurring kernel has a standard deviation in the order of twice the center wavelength ($1.88\lambda_c$), where the center wavelength is $\lambda_c = 0.74$ mm.

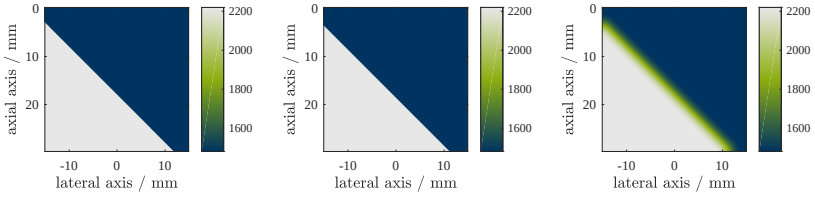

Figure 4.3.1: Distorted SOS distribution of numerical “disc-source” phantom; original SOS distribution (a), shifted SOS distribution (b), blurred SOS distribution (c)

The respective reconstruction results after 100 iterations are found in Figure 4.3.2. While the boundaries of the disc phantom are clearly visible and form a correct circle, the lateral boundaries are clearly displaced in the shifted phantom and the respective boundaries that are backpropagated after reflection from the SOS transition are tilted. In the reconstruction with the blurred SOS distribution, the lateral boundaries are barely visible and strong artifacts appear on both sides. As these introduced distortions are a conceptual error within the back propagation mode, it is not expected that the these results will

improve with a higher number of iterations.

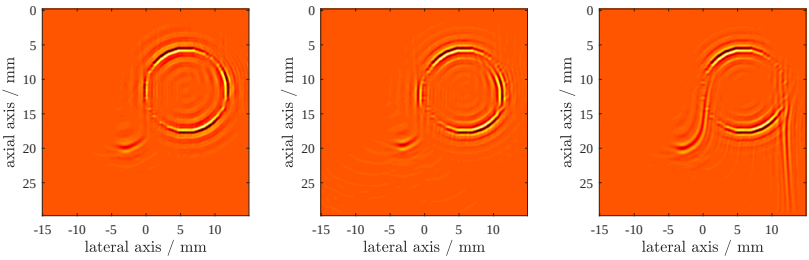

(a) (b) (c)

Figure 4.3.2: Landweber reconstruction results of the "disc-source" phantom with distorted SOS distribution after 1000 iterations; result using original SOS distribution (a), result using shifted SOS distribution (b), result using blurred SOS distribution (c)

4.3.2 SOS Estimation Using a Non-Linear Reconstruction

Finally, the performance of the Landweber reconstruction using reconstructed medium heterogeneities and hence not requiring any a-priori knowledge of the imaged tissue is assessed. The SOS map was derived from the Kaczmarz ultrasound reconstruction described at the beginning of section 4.3. Again, the carotid artery phantom was employed to provide an impression of the results in realistic medium properties. For this simulation, the phantom was slightly shifted in axial direction, since the Kaczmarz reconstruction generated strong artifacts in regions very close to the transducer. In a realistic scenario, this might be achieved by using a physical standoff or a setup in water, providing a layer of appropriate thickness with homogeneous material properties. For the ultrasound reconstruction, single element excitations were used. The center frequency of the excitation pulse had to be chosen as 763 kHz, which is lower than the transducer's center frequency of 2 MHz. This was done to comply with a general restriction of the method that does not allow for phase shifts of more than π between the waves traveling in the actual medium compared to waves traveling in the medium of the first iteration step [129]. The respective non-linear reconstruction result after 15,000 iterations is depicted in Figure 4.3.3-c

next to the actual SOS distribution (Fig. 4.3.3-b) and the PA source distribution (Fig. 4.3.3-a) and . While large homogeneous regions could not completely be restored in the SOS reconstruction, the general shape of all structures is recreated precisely and edges are preserved with almost no blurring.

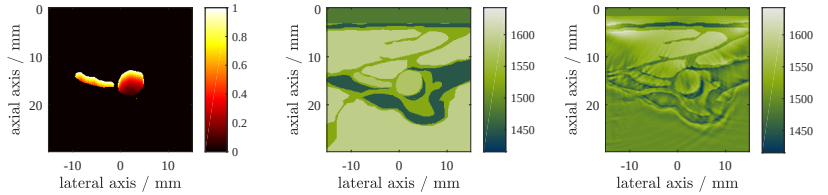

Figure 4.3.3: Numerical "carotid-artery" phantom; photoacoustic source distribution (a), speed-of-sound distribution (b), estimated speed-of-sound distribution by Kaczmarz reconstruction (c)

In Figure 4.3.4, the reconstruction results of the Landweber method using the SOS map returned by the Kaczmarz reconstruction is compared to the result using the original distribution and a Fourier backpropagation PA reconstruction that does not consider SOS variations (see (2.2.12)). Other than the standard reconstruction, the iterative reconstruction maps the sources to the correct locations and restores much of the signal lost by the limited view and damped by the impulse response of the transducer and the laser pulse. Comparing the reconstruction in the actual speed of sound to the reconstruction in the speed of sound estimated by the Kaczmarz method, a difference in the images can barely be made out. A normalized error between the reconstruction result $\hat{p}_0$ and the actual distribution p_0 was calculated for all three results in Figure 4.3.4 as:

$$e = \frac{E(p_0 - \hat{p}_0)}{\sqrt{E(p_0)E(\hat{p}_0)}} \tag{4.3.3}$$

with the signal energy operator E defined applied to p_0 calculates as $Ep_0 = \int_\Omega p_0(\boldsymbol{r})^2 d\boldsymbol{r}$. While the standard reconstruction returned a normalized error of 15.6 dB, the Landweber reconstruction based on the actual SOS distribution returned an error of 2.8 dB and the Landweber reconstruction based on the Kaczmarz SOS estimation returned 3.5 dB.

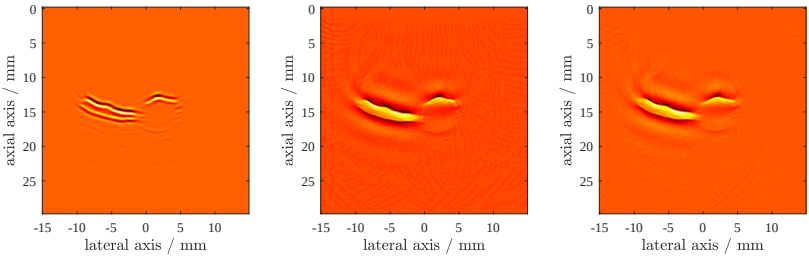

(a) (b) (c)

Figure 4.3.4: Reconstruction results of numerical “carotid-artery” phantom; standard reconstruction (a), Landweber reconstruction after 10,000 iterations using the acutal SOS disitribution (b), Landweber reconstruction after 10,000 iterations using SOS distribution estimated by the Kaczmarz reconstruction (c)

4.4 Discussion and Conclusions

In this chapter, an iterative photoacoustic reconstruction algorithm that is based on the Landweber method was derived and studied. The algorithm considers a set of properties of the measurement that are usually neglected during reconstruction, such as the transducer dimensions, the impulse responses of the transducer and the laser excitation and, most important, acoustical heterogeneities.

First, the general capabilities of the method with exactly known heterogeneity distributions were tested. The reconstruction results in section 4.2.1 show that the resolution of band filtered measurements in the presence of both compressibility scatterers and mass density scatterers can be strongly improved using the Landweber iteration and improves with an increasing number of iterations. It was furthermore shown that the presence of acoustic heterogeneities is not necessarily a harm to the reconstruction. Once the heterogeneities are considered in the reconstruction, the image quality can even be significantly improved by restoring structures, which generate waves that are only measured by a limited aperture after scattering (see section 4.2.1). It was shown in section 4.2.2 that the Landweber reconstruction does not succeed in recovering spatial frequencies that have not been propagated due to complete

suppression of the referring temporal frequencies in the impulse response (see Fig. 4.2.8). However, damped frequencies can be efficiently recovered, even in the presence of noise (see Fig. 4.2.10) and the results are very close to a Wiener deconvolution of the measurement data, where both noise spectrum and signal spectrum are exactly known (see Fig. 4.2.11). The recovery of lateral structures is much more effective using the Landweber method than using Wiener deconvolution. It is questionable if the high computational effort justifies this improvement over direct filtering methods, but at least when scattering dominates the image quality, the Landweber reconstruction might still be the best choice. In a simulation that imitates a clinical measurement of the carotid artery, the benefits of the Landweber iteration above a standard reconstruction were proven in section 4.2.3. Even though the SOS deviations in the region of the carotid artery are comparably low, there is a significant degradation of the image if the SOS distribution is not considered. The Landweber reconstruction succeeds in restoring the actual shape and quite much of the bandwidth of the actual phantom.

After the general assessment, the capabilities of the Landweber reconstruction for an imperfectly known acoustic heterogeneity distribution were stressed. First, the algorithms vulnerability to distortions of the employed heterogeneities was investigated by shifting and blurring the respective distribution. In the tested scenario, small deviations from the actual distribution lead to significant artifacts in the reconstruction (see section 4.3.1). It is likely that a convergence for imperfect data cannot be assured. Considering that, compared to the employed center wavelength, only slight manipulations of the underlying SOS distribution were made, the robustness of the Landweber reconstruction to imperfect heterogeneity data must be highly questioned. However, in the frame of simulated data, it could be shown that similar results could be produced without any a-priori knowledge about the acoustic heterogeneities (see section 4.3.2). By employing a non-linear US reconstruction based on single element emissions, a highly resolved SOS distribution could be estimated. Even though the estimation exhibited some artifacts, the result of the Landweber reconstruction based on the estimated SOS distribution did not deviate strongly from a result, where the actual distribution was used. Still, especially in the light of the Kaczmarz US reconstruction not yet having been applied to experimental data and being restricted in the employed temporal frequencies, an actual application of the Landweber method in a clinical PA imaging system is currently not likely. For that reason, less model based but more robust and efficient algorithms to account for acoustic heterogeneities will be introduced in the following chapters of this dissertation.

5

Refraction-Compensating Reconstruction

In this chapter, a new method to account for aberrations in PA imaging is introduced that will be referred to as paraxial back propagation (PBP). The method is validated on simulation data and on in-vivo data. Some of the methods and results have been published in a conference article [153].

As pointed out in section 3.2.2, the quantity that is responsible for aberrations is the speed of sound. Therefore, within this chapter, variations in acoustic properties are limited to variations in the speed of sound. Variations of mass density and compressibility leading to a constant SOS may still generate scattering of the wave but do not delay or advance wave fronts. Hence, such scatterers do not contribute to aberrations and, in consequence, are not addressed here.

The method that is introduced in this chapter relies on a paraxial wave propagation model, which is related to the Fresnel approximation and is valid for waves that have a predominant propagation direction. The key component of the approximation is a split step approach, which separates diffraction and refraction of the wave into two consecutive steps during a wavefield extrapolation. This model is able to efficiently approximate wave front distortions by variations in the SOS by considering forward scattering, while backscattering is completely neglected. The benefit of the neglection of backscattered waves during back propagation will be investigated by comparing the method to a direct time reversal approach.

Paraxial approximations, which are also referred to as parabolic approxi-

mations, have been used for imaging and simulations in other contexts. Besides the split step approach, there are variations of the model, for example the "non-stationary phase shift" or the "phase shift and interpolation approach" [120]. Due to the necessity to calculate multiple wavefields, however, these approaches can be expected to be more time consuming than the split step. In numerical studies, a propagation model resembling the one that is proposed in this chapter was used for an iterative reconstruction algorithm in transmission ultrasound tomography [9, 64] and a direct approach in reflection tomography [81, 82]. Other applications of paraxial approximations for imaging or simulations can be found in the field of optics [54, 68] or geophysics [120].

5.1 A Paraxial Wave Propagation Model

For the consideration of aberrations, backscattering is not of interest but rather the phase delays of the wave, which are introduced by speed of sound variations. Hence, the first simplification for this method is the neglection of those parts of density variations and compressiblity variations that do not affect the speed of sound according to $c = (\rho\kappa)^{-1/2}$. For the sake of a compact notation, the speed of sound variation will henceforth be represented by it's relative deviation $\gamma_c(\mathbf{r})$ of the actual SOS $c(\mathbf{r})$ from the reference SOS c_0 by $\gamma_c(\boldsymbol{r})$, which is defined as:

$$\gamma_c(\mathbf{r}) = c_0/c(\mathbf{r}) - 1. \tag{5.1.1}$$

The respective Helmholtz equation, which is the temporal frequency domain representation of the wave equation, reads as:

$$\Delta p + k_t^2(1+\gamma_c)^2 p = 0 \tag{5.1.2}$$

with k_t being the temporal wave number according to $k_t = \omega/c_0$, with ω being the angular temporal frequency and c_0 being the scalar reference SOS. Note that the paraxial approximation is a general wave propagation model and hence, for now, the photoacoustic sources are neglected. Also, in this wave model, mass density variations are not as accurately included as in the general wave equation for heterogeneous media in (2.1.21).

The paraxial extrapolation of a pressure field in z-direction is derived in line with [9], where a similar approach was used for simulating the wave propagation in transmission ultrasound tomography. Applying an envelope transformation with:

$$p(\mathbf{r}) = e^{ik_t z} u(\mathbf{r}) \tag{5.1.3}$$

a substitution into the Helmholtz equation (5.1.2) yields:

$$\partial_{xx}u + \partial_{zz}u + 2ik_t\partial_z u + k_t^2\left((1+\gamma_c)^2 - 1\right)u = 0. \tag{5.1.4}$$

For p being a plane wave that propagates into z-direction, u is constant in z. For all plane wave solutions to p with a small angle in relation to the z-axis, u varies slowly with z. Thus, in these cases $\partial_{zz}u$ can be neglected and the differential equation can be factorized to

$$(\partial_z + ik_t + ik_tQ)(\partial_z + ik_t - ik_tQ)u = 0 \tag{5.1.5}$$

with Q being a pseudo differential operator that is defined as:

$$Q := \sqrt{k_t^{-2}\partial_{xx} + (1+\gamma_c)^2}, \tag{5.1.6}$$

which can be approximated by:

$$Q \approx \sqrt{1 + k_t^{-2}\partial_{xx}} + \gamma_c \tag{5.1.7}$$

as suggested in [54] and also employed in [9]. Note that the factorization in (5.1.5) is only valid, if the commutator of the two operators Q and $\partial_z + ik_t$:

$$[\partial_z + ik_t, Q] = \partial_z Q - Q\partial_z \tag{5.1.8}$$

can be neglected, which is the case for n varying slowly with z [9]. The two factors in (5.1.5) result in two separable differential equations, where one describes the forward propagating wave envelope u^+ and one the backward propagating wave envelope u^- in relation to the z-axis. The formal solution after solving for u^+ or u^- and evaluating at $z + \Delta z$ yields an extrapolation formula of the fields for given values at z:

$$\begin{aligned} u^-(x, z+\Delta z) &= e^{-ik_t(1-Q)\Delta z}u^-(x,z) \\ u^+(x, z+\Delta z) &= e^{-ik_t(1+Q)\Delta z}u^+(x,z) \end{aligned} \tag{5.1.9}$$

For this, γ_c is required to be constant over z within the interval $[z, z+\Delta z]$, which is from now on referred to as one slice. Assuming the SOS varying slowly with z, this assumption is not expected to harm the results too much and its impact will decrease with decreasing Δz. Using the approximation of Q in (5.1.7), Lie-Trotter splitting of the two summands of this approximated Q can be employed, assuming they commute [69]. Then the solutions read as:

$$u^\mp(x, z+\Delta z) = e^{-ik_t\Delta z}e^{\pm ik_t\left(\gamma_c(x,z) + \sqrt{1+k_t^{-2}\partial_{xx}}\right)\Delta z}u^\mp(x,z)\ , \tag{5.1.10}$$

where the pseudo spectral operator $\exp(\pm ik_t((1+k_t^{-2}\partial_{xx})^{1/2}\mp 1)\Delta z)$ can be expressed in the frequency domain as $\exp(\pm ik_t((1-(k_x/k_t)^2)^{1/2}\mp 1)\Delta z)$ using the Fourier pair $x \longleftrightarrow k_x$. In consequence, the extrapolation of forward and backward propagating envelope fields can be approximated by:

$$\begin{aligned} u^{\mp}(x,z+\Delta z) = \quad & e^{-ik_t\Delta z}e^{\pm ik_t\gamma_c(x,z)\Delta z} \\ & \cdot\mathscr{F}_{k_x}^{-1}\left\{e^{\pm i\kappa_z\Delta z}\mathscr{F}_x\left\{u^{\mp}(x,z)\right\}\right\} \end{aligned} \tag{5.1.11}$$

with $\kappa_z := k_t((1-(k_x/k_t)^2)^{1/2}$ yielding a solution to the forward and backward propagating pressure fields according to (5.1.3), that writes as:

$$\boxed{\begin{aligned} p^{\mp}(x,z+\Delta z) = \quad & e^{\pm ik_t\gamma_c(x,z)\Delta z} \\ & \cdot\mathscr{F}_{k_x}^{-1}\left\{e^{\pm i\kappa_z\Delta z}\mathscr{F}_x\left\{p^{\mp}(x,z)\right\}\right\}. \end{aligned}} \tag{5.1.12}$$

This solution can be understood heuristically as a separation of the wave propagation into two processes. The first process describes the diffraction of the wave, assuming a constant SOS. The diffraction is applied by shifting each mono frequent plane wave, measured in one axial plane, into its propagation direction, such that the axial component of the shift matches Δz. The second process describes the refraction of the wave, which is applied by adjusting the phase of the wavefield according to the actual SOS at each lateral location within Δz. As a directive information of the wave cannot directly be addressed in the space domain, this step assumes that the whole wavefield would have propagated directly into z-direction. The error induced by this simplification vanishes with decreasing Δz.

The efficiency of the paraxial split step approach might be explained as follows: For the wave diffraction, the propagation angle of the plane waves is of importance, where one plane wave angle corresponds to one lateral frequency in the frequency domain of x. On the other hand, for the refraction, the spatial distribution of the SOS distribution in the respective slice is of importance. Separating diffraction and refraction into two successive steps while alternating from space domain to spatial frequency domain, the wavefield can be extrapolated efficiently, as the Fourier transforms can be computed using fast Fourier algorithms. The recursive nature of the paraxial approximation is necessary, since a direct computation of the propagation through multiple slices Δz is not possible. This is due to the fact that the phase shift in the frequency domain and the phase shift in the space domain do not commute, which becomes obvious, when regarding them as a convolution in x followed by a multiplication in x.

5.2 Paraxial Photoacoustic Back Propagation

The aim of a photoacoustic reconstruction is to deduce the initial pressure distribution $p_0(\mathbf{r})$ from the temporal measurement of the respective wavefield at the sensor, which is now referred to as $p_m(x,t) = p(\mathbf{r}_s,t)$. The initial pressure distribution is defined as the acoustic wavefield at $t=0$, which is the moment of laser illumination. Note that a laser pulse shape deviating from a temporal delta impulse will only result in a temporal filtering of the respective signals if thermal confinement is met. In consequence, the forward problem can be modeled by an initial value problem that is defined by the Helmholtz equation (5.1.2) and the boundary conditions:

$$\begin{aligned} p(\mathbf{r},t=0) &= p_0 \\ \partial_t p(\mathbf{r},t=0) &= 0 \end{aligned} \tag{5.2.1}$$

as long as p is evaluated at times $t>0$. Obviously, this initial value problem can be solved by determining the entire wavefield $p(\mathbf{r},t)$ and evaluating it at $t=0$. This corresponds to determining the entire wavefield $p(\mathbf{r},k_t)$ and integrating over k_t, because $p(t=0) = \int p(k_t)\exp(ik_t 0)dk_t = \int p(k_t)dk_t$. The approximation of the entire wavefield can be achieved based on the recursion formula (5.1.12) as an extrapolation into positive z-direction of the wavefield traveling into negative z-direction p^-. This is because only PA waves traveling backward in regard to the z-axis can be measured by a transducer at $z=0$. Finally, the paraxial back propagation can be computed by the following instruction:

$$\boxed{\begin{aligned} p^-(x,z=0,k_t) &= p_m(x,k_t) \\ p^-(x,z+\Delta z) &= e^{ik_t\gamma_c(x,z)\Delta z} \\ &\quad \cdot \mathscr{F}_{k_x}^{-1}\left\{e^{i\kappa_z\Delta z}\mathscr{F}_x\left\{p^-(x,z)\right\}\right\} \\ p_0^{(px)}(\mathbf{r}) &= \tfrac{1}{2\pi}\int_{-\infty}^{\infty} p^-(\mathbf{r},k_t)dk_t \end{aligned}} \tag{5.2.2}$$

with $p_0^{(px)}$ being the paraxial estimation of the initial pressure distribution p_0.

5.3 Implementation

While the diffraction term $\exp(i\kappa_z\Delta z)$ in (5.2.2) is independent of z, the refraction term $\exp(ik_t\gamma_c(x,z)\Delta z)$ depends on z and needs to be computed for each slice individually. This and many more important considerations have

to be made for a discrete implementation of the paraxial back propagation (PBP) algorithm. They will be discussed in the following section. Also, when the algorithm is tested, the real benefit of a paraxial approximation can only be assessed in comparison to other algorithms that are able to compensate for SOS variations in a PA reconstruction. Therefore, in this chapter, issues during the implementation and suggestions to account for those are discussed and two reference algorithms are introduced, one more model based and one less model based than PBP.

Evanescent Waves

Despite the mathematical correctness of the diffraction term $\exp(ik_t(1-(k_x/k_t)^2)^{1/2}\Delta z)$ in (5.2.2), the presence of noise or even numerical inaccuracies in the evanescent parts of the measurement data prevents a reconstruction from generating adequate image results. Evanescent parts are referred to as the areas in the two dimensional spectrum of p_m, where the absolute of the lateral spatial frequency is higher than the absolute of the temporal wave number $|k_x| > |k_t|$. Looking at $k_t < k_x < 0$, the argument of the exponential function in the diffraction term $ik_t(1-(k_x/k_t)^2)^{1/2}\Delta z$ becomes real with a positive sign, which implies that the amplitudes of the evanescent parts in the measurement data increase exponentially during backward propagation. In fact, this is the correct inversion of the negative sign of the argument during forward propagation, where evanescent amplitudes decrease exponentially. However, for imperfect measurement data, the amplification of evanescent parts during back propagation is crucial. For that reason, the diffraction term was set to 0 for $|k_x| > |k_t|$ and, hence, not allowing evanescent amplitudes to be propagated at all. The respective propagation model reads as:

$$\begin{aligned} p^-(x,z+\Delta z) = \; & e^{ik_t\gamma_c(x,z)\Delta z} \\ & \cdot \mathscr{F}_{k_x}^{-1}\left\{e^{i\widetilde{\kappa}_z\Delta z}\mathscr{F}_x\left\{p^-(x,z)\right\}\right\} \end{aligned} \tag{5.3.1}$$

with

$$\widetilde{\kappa}_z = \begin{cases} k_t\sqrt{1-(k_x/k_t)^2} & ,|k_x| \geq |k_t| \\ 0 & ,\text{otherwise} \end{cases} \tag{5.3.2}$$

The Damping Layer

While temporal zero padding is not required, because the field is evaluated at $t = 0$ and not ealier, the periodic nature of discrete Fourier pairs evokes the

necessity to avoid lateral wrapping of waves exiting the lateral borders of the reconstruction area. This might be realized by zero padding in x-direction. Here, we introduce a more efficient way, which resembles to the concept of perfectly matched layers in finite difference or pseudo spectral simulation methods [26]. An additional layer is padded onto both lateral ends of the measurement data set p_m with $p_m = 0$ for $x \notin [x_1, x_2]$ and x_1 and x_2 being the start position and end position of the linear array in x. A layer width of 16 pixels was found to be a good trade-off between wave supression and computation time[1]. The heterogeneity distribution $\gamma_c(\boldsymbol{r})$ was padded with zeros likewise. After each recursion step, a lateral Tukey window was multiplied to all frequencies of the wavefield p at the current depth, damping all values in the padded area, such that the pressure value was eventually zero at the boundaries of the padded region but the damping was smooth enough to suppress strong reflections into the solution area. Mathematically speaking, the recursion step in (5.2.2) is supplemented with the Tukey window function w_{Tukey} as:

$$\begin{aligned} p^-(x, z+\Delta z) = \; & w_{Tukey}(x) e^{ik_t \gamma_c(x,z)\Delta z} \\ & \cdot \mathscr{F}_{k_x}^{-1} \left\{ e^{i\tilde{\kappa}_z \Delta z} \mathscr{F}_x \left\{ p^-(x,z) \right\} \right\} \end{aligned} \tag{5.3.3}$$

with $w_{Tukey}(x)$ being defined as:

$$w_{Tukey}(x) = \begin{cases} (1 - \cos(\pi(x - x_1 + \Delta x_p)/\Delta x_p))/2 & , x_1 - \Delta x_p \leqslant x \leqslant x_1 \\ 1 & , x_1 < x < x_2 \\ (1 + \cos(\pi(x - x_2)/\Delta x_p))/2 & , x_2 \leqslant x \leqslant x_2 + \Delta x_p \end{cases} \tag{5.3.4}$$

within the interval $x \in [x_1 - \Delta x_p, x_2 + \Delta x_p]$, where the original lateral grid is defined within the interval $[x_1, x_2]$ and Δx_p is the lateral width of the padded area. The application of the damping window is visualized in Figure 5.3.1, where exemplary reconstruction results are displayed without damping window, with a 2 pixel damping window and with a 16 pixel damping window. The respective windowing functions are plotted as green line above the plots. The image without damping window exhibits some strong structures on the left and right side above the actual sources, which can be assigned to wrapping artifacts. In the image with 2 pixels padding width, wrapping cannot appear because all

[1] Note that, referring to a transducer with λ-spacing and a computation grid with the same spacing as the transducer, 16 pixels equals 16 times the center wavelength.

wave amplitudes exiting the solution area are set to 0. However, there are still some significant artifacts visible, which can be assigned to reflections, due to the fast decay of the wave amplitudes over space within the padded area. These reflections are strongly suppressed in the image, where the 16 pixels damping window was applied. Note that, instead of an additional multiplication with the Tukey window, γ_c can also be chosen to be imaginary in that area to apply an artificial attenuation. Since the numerous executions of the lateral fast Fourier transforms (FFT) is the most time consuming operation in the paraxial back propagation, it is recommended to choose the number of pixels in lateral direction including the damping layer to exhibit small maximum prime factors, which will lead to an efficient computation of the FFT [32]. In the plots in the results section of this chapter, the padded pixels are always cropped off after the reconstruction for an accurate visualization.

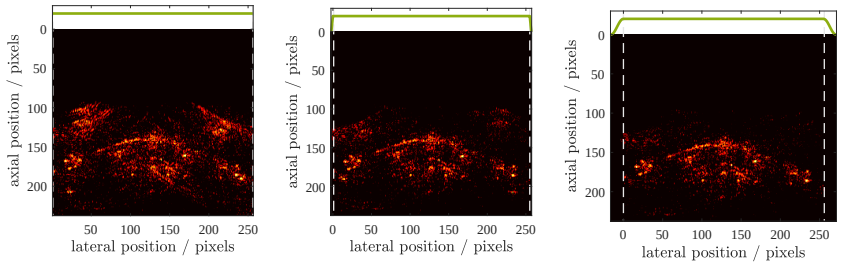

Figure 5.3.1: Comparison of lateral damping layer sizes in PBP reconstruction; no damping layer (a), 2 pixels damping layer (b), 16 pixels damping layer (c), dynamic range: 20 dB, more information about the data set can be found in section 5.5.3.

The Transmission Factor

Besides wave attenuation by dissipative energy conversion, which is not considered here, the wave front of a forward propagating wave is attenuated by reflections due to the power distribution into the transmitted and the reflected wave. For given acoustic properties, this behavior can be included into the paraxial wave propagation model by introducing a transmission factor for a wave propagating into negative z-direction. A general transmission factor in

conduction theory for a wave traveling into negative z-direction is defined as [144]:

$$T^{-}(z+\Delta z) = \frac{2Z(z)}{Z(z)+Z(z+\Delta z)} \tag{5.3.5}$$

with $Z(z) = \rho(z)c(z)$ being the medium's impedance, where it is assumed that Z is constant within the interval $z \in [z, z+\Delta z[$ and the transitions occurs at $z+\Delta z$. Assuming a homogeneous density and using (5.1.1), T can be expressed as a function of γ_c as:

$$T^{-}(z+\Delta z, y) = 2\left(1+\frac{1+\gamma_c(z,x)}{1+\gamma_c(z+\Delta z,x)}\right)^{-1} \tag{5.3.6}$$

This inclusion into the forward model has also been suggested by Gemmeke et. al [63]. A straight forward approach to include the transmission factor into the backward wave model is to multiply the inverse value of the transmission factor with the backward propagated wave in the recursion step, which, after including the aforementioned damping window, reads as:

$$\begin{aligned} p^{-}(x,z+\Delta z) = \; & w_{Tukey}(x)/T^{-}(x,z+\Delta z)e^{ik_t\gamma_c(x,z)\Delta z} \\ & \cdot \mathscr{F}_{k_x}^{-1}\left\{e^{i\tilde{\kappa}_z\Delta z}\mathscr{F}_x\left\{p^{-}(x,z)\right\}\right\} \end{aligned} \tag{5.3.7}$$

Hence, the amplitude loss due to reflections during the forward propagation can be accounted for without actually computing the reflected wavefields.

5.3.1 Reference Algorithms

The paraxial reconstruction will be compared to two other heterogeneous reconstruction methods within the scope of this chapter. The first reconstruction method is a less model based approach using a delay-and-sum formalism, where individual delays are computed for each combination of a pixel location and a sensor element location by ray tracing:

$$\Delta t(\mathbf{r},\mathbf{r}_s) = \int_0^{|\mathbf{r}_s-\mathbf{r}|} \frac{1}{c(\mathbf{r}+s\cdot\mathbf{e}_s)}ds. \tag{5.3.8}$$

Here, $\mathbf{r}$ is the location of the current pixel to reconstruct, $\mathbf{r}_s = (x_s, 0)$ is the location of the respective sensor element in the lateral interval $x_s \in [x_1, x_2]$ and $\mathbf{e}_s = (\mathbf{r}_s - \mathbf{r})/|\mathbf{r}_s - \mathbf{r}|$ is the unity vector pointing from $\mathbf{r}$ to $\mathbf{r}_s$. The integral

is evaluated as discrete sum over an index j with $s = j \cdot \Delta s$, with incremental distance Δs matching the lateral element pitch and the values of $c(\mathbf{r})$ are queried at $\mathbf{r} + j \cdot \Delta s \cdot \mathbf{e}_s$ using nearest neighbor interpolation. The initial pressure distribution $p_0(\mathbf{r})$ is then estimated by evaluation of the measurement data at the specific delays followed by lateral integration:

$$p_0^{(ray)}(\mathbf{r}) = \int_{x_1}^{x_2} p_m(x_s, \Delta t(\mathbf{r}, \mathbf{r}_s)) d\mathbf{r}_s \tag{5.3.9}$$

which, again, is computed as discrete sum over all channels. This method corrects for delays caused by a heterogeneous SOS distribution, treating acoustic waves as straight rays, and not accounting for refraction or scattering. A comparable model was suggested by Dean-Ben et al. in [44].

In contrast to this straight ray approach, a time reversal reconstruction is a strictly model based approach and has been widely used for PA imaging in heterogeneous media (see chapter 3.2.1). In time reversal imaging, the photoacoustic measurement is temporally inverted and treated as Dirichlet boundary condition in the computation of a time reversal field $p_{TR}(\mathbf{r}, t)$ [188]:

$$p_{TR}(\mathbf{r}, t) = \int \int_{\partial\Omega} p_m(\mathbf{r}'_s, T - t') \partial_{z'} g_\gamma^{(D)}(\mathbf{r}, \mathbf{r}'_s, t, t') d\mathbf{r}'_s dt'. \tag{5.3.10}$$

Here, T is the time during which the measurement was recorded and $g_\gamma^{(D)}$ is the full wave Green function that is subject to the Dirichlet boundary condition on $\partial\Omega$ [188]. While the analytic solution of $g_\gamma^{(D)}$ is not obvious, (5.3.10) can be computed using numerical wavefield solvers, such as finite difference or pseudo-spectral methods. In such simulations, the boundary condition can be implemented as a forced time varying source term located at the transducer surface [172]. To estimate the initial pressure distribution p_0, the time reversal field is evaluated at $t = T$:

$$p_0^{(TR)}(\mathbf{r}) = p_{TR}(\mathbf{r}, T) \tag{5.3.11}$$

In principle, time reversal assumes that physical processes are invariant of their temporal direction, meaning it can not be distinguished, if an event happened forward or backward in time. Hence, if the complete wavefield propagating out of an observation domain is propagated back into the domain, the complete wavefield is reversed. In consequence, back propagating the measured wavefield and evaluating it at $t = 0$ should recover the exact initial pressure distribution. However, in case of a limited view, where only a part of

the wavefield is back propagated, this implies that reflected waves occur that would have been canceled out in a full view back propagation. These additional reflections can appear as false sources in the initial pressure distribution. In consequence, time reversal comes with the advantage of accounting for all involved reflections in the forward process, but if the time reversal data is incomplete, it might be even better to neglect these reflections in order to reduce artifacts. Figure 5.3.2 illustrates this problem on a one dimensional grid, comparing the data measured and back propagated from either only one side of the solution area (limited view), or both sides of the solution area (full view). In addition, a limited-view time reversal that does not consider the SOS inclusion is shown. After the complete time reversal at $t = 0$, the limited view solution that considers the SOS inclusion can map the source to the correct position but exhibits additional peaks close to the inclusion. In contrast, these artifacts do not occur for the limited view backpropagation that does not consider the SOS inclusion. However, in that case, the source is also not mapped onto the correct position. Accounting for refraction but neglecting reflections, paraxial back propagation has the potential of combining both features, a correct mapping and no additional scatter artifacts, which will be investigated in the following.

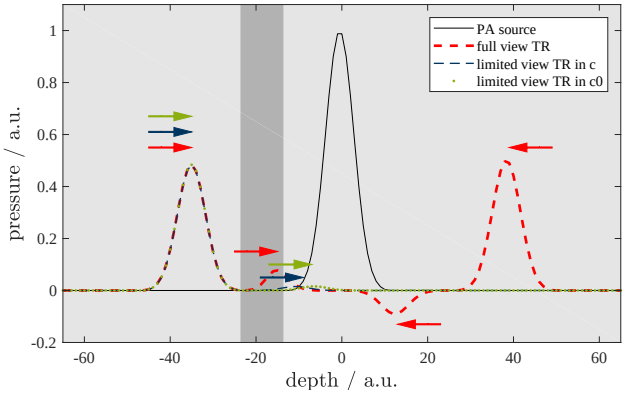

(a)

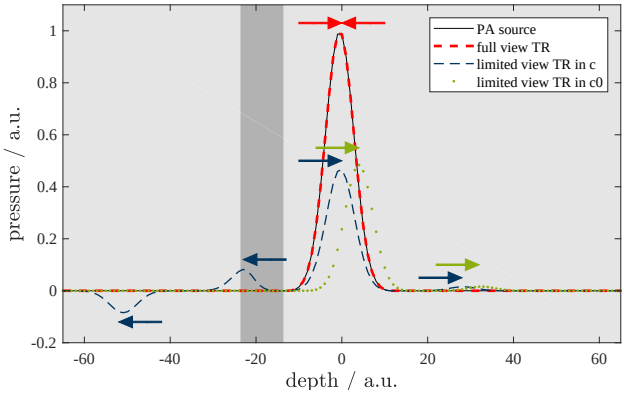

(b)

Figure 5.3.2: One dimensional time reversal in a heterogeneous medium with an inclusion c of 30% deviation from the background SOS c_0 in the interval indicated by the dark gray background; (a) wavefield at $t = T - 0.13T$ showing the back propagating waves before entering the region of deviated SOS (b) wavefield at $t = 0$ showing the estimated initial pressure distribution. Here, a full view means a detection and back propagation from both ends of the solution area, while a limited view means detection and backpropagation from only the left side.

5.4 Aberration Correction in Known Heterogeneities

The first experiments are designed to assess the general capabilities of the PBP method. For now, the SOS distribution is considered to be known, which certainly does not hold for actual clinical data sets. However, in order to have the results independent from inaccuracies of a speed of sound reconstruction, the assumption of known SOS distributions is inevitable to verify the method. Approaches to combine PBP with SOS reconstructions, such that no a priori knowledge about the actual distribution is required, will be presented in section 5.5.

5.4.1 General Capabilities in Comparison to Other Methods

The general capabilities of the paraxial back propagation were assessed on well controlled simulation data. A numerical phantom was designed that consists of two point sources in a speed of sound background with circular inclusions of random size and random SOS deviation as depicted in Figure 5.4.1. The simulation settings are listed in table 5.4.1.

Property	Value	Unit
grid size	128×128	pixels
grid area	12.8×12.8	mm^2
center frequency	11.75	MHz
fractional bandwidth	80	%
transducer elements	128	
pitch	0.1	mm
kerf	0	mm

Table 5.4.1: Simulation properties for Random SOS discs phantom

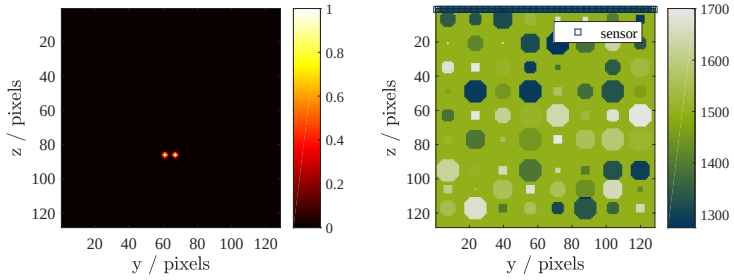

Figure 5.4.1: Numerical "point-source" phantom with random SOS inclusions; PA source distribution (a), SOS distribution (b)

Figure 5.4.2 shows the reconstruction results after envelope detection on a linear intensity map and the respective line profiles through the point sources on a logarithmic scale. While the homogeneous reconstruction distributes the sources all over the lower image area, the ray-tracing algorithm focuses on the actual location more successfully, but still does not allow for a separation of the two point sources. In contrast to that, both the paraxial reconstruction and the time reversal approach succeed in mapping the peaks of the two sources onto the actual source locations and the two sources are clearly distinguishable with a dip in the range of -15 dB. In terms of computation time, the PBP clearly outperforms time reversal by a factor of 20.5 (see caption of Fig. 5.4.2) but by a factor of 6.2 slower than the homogeneous reconstruction. It should be noted that these computation times are highly dependent on the respective implementation and on the specific imaging grids and can therefore not be generalized.

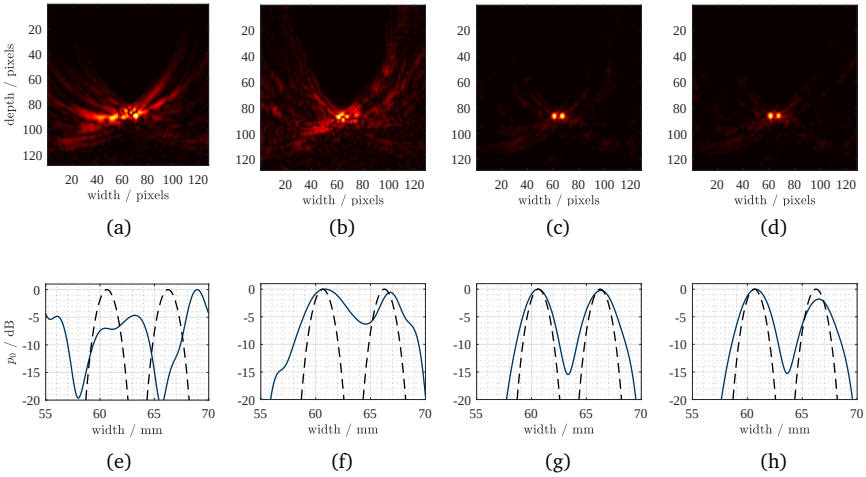

Figure 5.4.2: Comparison of reconstruction methods for random SOS inclusions (computation times in brackets); standard reconstruction (0.11 s) (a,e), ray tracing DAS reconstruction (16.58 s) (b,f), paraxial reconstruction (0.68 s) (c,g), time reversal reconstruction (13.94 s) (d,h)

In order to attain a more complete idea of how PBP and time reversal compete with each other in terms of the image quality, the experiment was extended by separating the part of the SOS distribution accountable for transmission scattering and the part accounting for reflection scattering. In addition, a comparison of the two methods in a homogeneous medium was conducted. The respective SOS distributions and reconstruction results are depicted in Figure 5.4.3. The first phantom, which only exhibits transmission scattering (Figure 5.4.3-a) leads to comparable spatial distributions for both methods, indicated by similar dips between the two point sources (see Figure 5.4.3-j). However, the amount of artifacts above the sources is higher for the time reversal method (second column in Figure 5.4.3), which can be attributed to back reflection during the back propagation in limited view time reversal (see Fig. 5.3.2 for explanation). However, it should be mentioned that these artifacts are only visible due to the logarithmic intensity scale on the large dynamic range of 50 dB. In the scenario with heterogeneities only behind the

sources (Figure 5.4.3), which implies that only reflection scattering occurs, the amount of artifacts of the two methods is similar. However, the dip between the two sources is about 3 dB deeper for time reversal, which might be assigned to the fact that reflected waves during time reversal back propagation are remapped onto the source location, while the PBP does not account for backscattering. This indicates that, for heterogeneities behind the source, backscattering during back propagation is actually desired, while it corrupts image quality for heterogeneities in front of the sources. The reconstruction in the homogeneous medium in the last column of Figure 5.4.3 is only a reference verifying that the artifacts in the other configuration can actually be attributed to scattering.

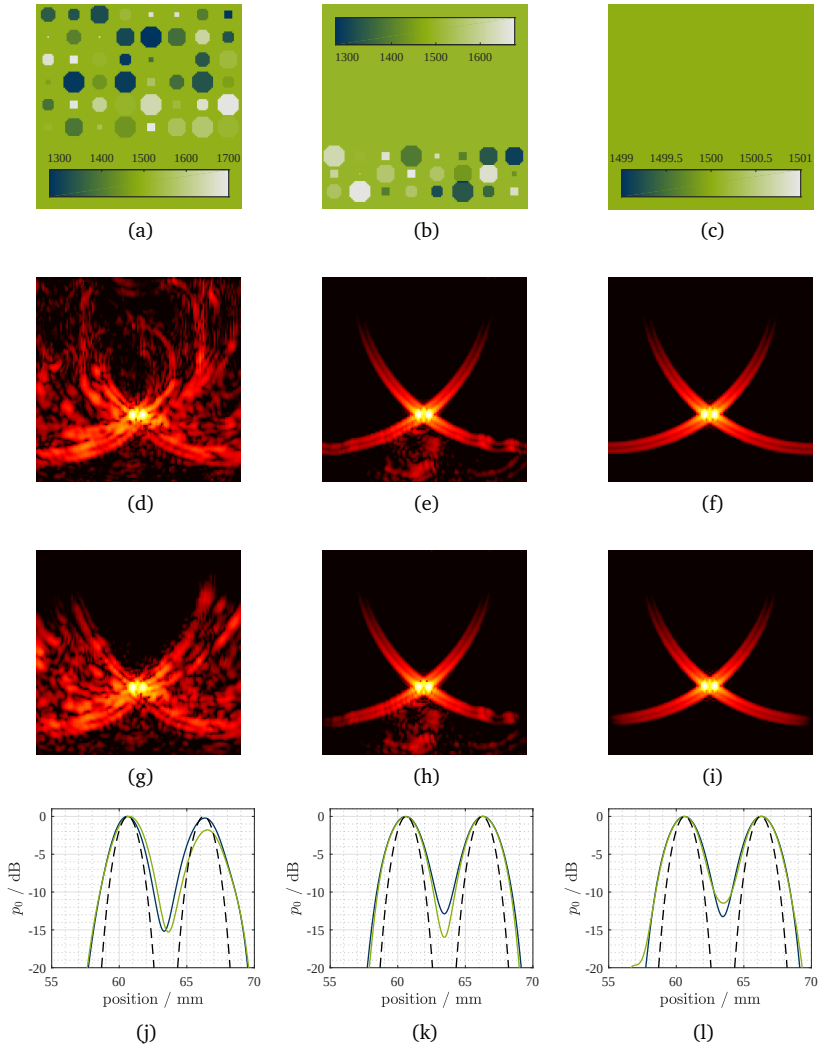

Figure 5.4.3: Comparison of PBP and time reversal reconstruction methods for differently located SOS inclusions; the three SOS distributions (a-c), time reversal results (d-f), PBP results (g-i) and profiles with time reversal in blue and PBP in green (j-l), axes according to Fig. 5.4.2

5.4.2 Performance Using Realistic Properties

The SOS deviations in Section 5.4.1 generated strong aberration artifacts, such that the accuracy of the paraxial back propagation algorithm could be assessed in detail. However, in order to draw direct conclusions about the benefit of the method being applied to realistic clinical tissue properties, numerically generated measurement data of the carotid artery phantom, which is described in detail in chapter 2.4, provide more insights. The photoacoustic source distribution and the SOS distribution are depicted in Figure 5.4.4. The simulated transducer exhibited 96 elements with a pitch of 0.45 mm, a kerf of 0.49 mm, a center frequency of 7.5 MHz and a fractional bandwidth of 78%.

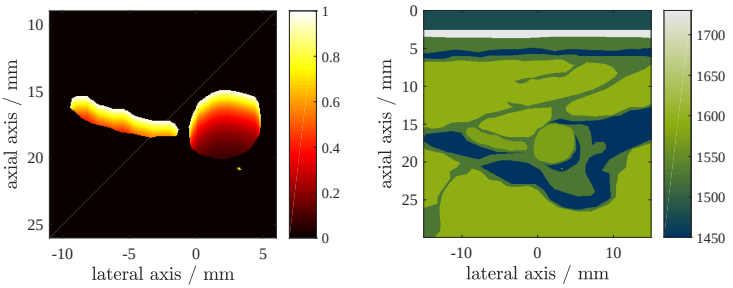

Figure 5.4.4: Numerical "carotid artery" phantom; photoacoustic source distribution (magnified to visualize the hemorrhage) (a), speed of sound distribution (b)

The following results address the benefit of the PBP in comparison to a standard reconstruction that does not consider SOS variations. The first question is in how far SOS variations can distort the image in a realistic scenario and in how far the PBP can compensate for these distortions. In order to visualize the extent of distortions of the shape, an overlay image of the reconstructed image on the actual source distribution is depicted in Figure 5.4.5. Without applying any noise and depicting the PA images on a logarithmic intensity scale with a dynamic range of 30 dB, all boundaries can clearly be seen. In contrast to the distorted shape of the standard reconstruction, the PBP returns a well defined contour along the actual boundaries of the vessels. Especially

the small structure at $(20.9, 3.2)$ mm, which mimics a hemorrhage, appears to be less blurred than in the standard reconstruction.

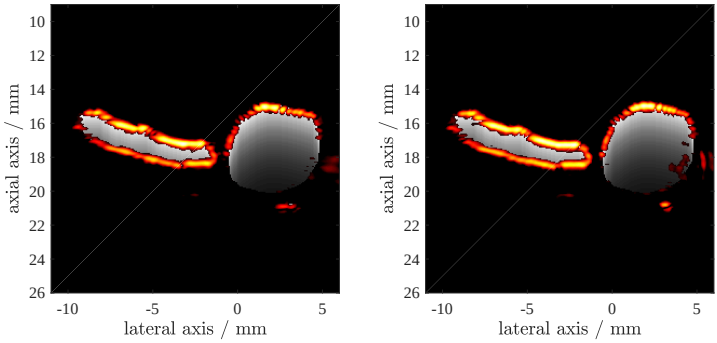

Figure 5.4.5: Comparison of reconstructions of "carotid artery" phantom in an overlay image with the reconstructed source distribution over the actual source distribution on a gray scale; standard reconstruction (a), PBP (b) (DR 50dB)

Besides a slightly corrupted interpretability due to the false allocations of the boundaries, it can be expected that blurring of small structures will decrease their maximum signal strength and might disappear in noisy data. Therefore, Gaussian noise was added to the numerically generated measurement data with a signal to noise ratio (SNR) of -9 dB. The respective results of the PBP, again in comparison to a standard reconstruction are shown in Figure 5.4.6. For this scenario, the hemorrhage at $(20.9, 3.2)$ mm is clearly visible in the PBP reconstruction but can hardly be distinguished from noise in the standard reconstruction.

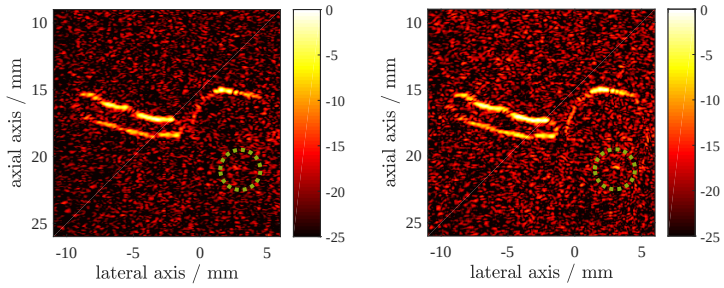

Figure 5.4.6: Comparison of reconstructions of "carotid artery" phantom for noisy data (SNR -9dB); standard reconstruction (a), PBP (b) (dynamic range 25 dB)

5.5 Aberration Correction in Estimated Heterogeneities

In contrast to the previous results, which validated the general capabilities of PBP, this section addresses the actual applicability of the method in clinically relevant scenarios, where the SOS distribution is generally unknown. First, the SOS information provided to the reconstruction algorithm is actively manipulated in order to verify the robustness of the algorithm in a controlled simulation setup with realistic medium properties. Then, the performance of the method using an SOS distribution that was reconstructed from plane wave reflection mode data is assessed. The algorithm for the SOS reconstruction was introduced as "computed ultrasound tomography in echo mode" (CUTE) [87] and exploits the linear relation between the inverse of the SOS distribution and phase delays of waves received from different transmission angles. The respective algorithm for the reconstruction was provided by Andreas Ihrig. Finally, paraxial back propagation is applied to in vivo data showing murine tissue, where two regions were segmented from an US image and values for the SOS of ultrasound gel and general tissue were assigned to these two regions.

5.5.1 Assessment of Robustness

The ability of the PBP to retrieve PA sources in an imperfectly reconstructed SOS distribution is estimated by actively impairing the accuracy of a known SOS distribution and verifying the effect on the photoacoustic reconstruction. The main purpose of this investigation is to figure out, if, for a clinically relevant tissue composition, imperfect information about the SOS distribution can still improve the image quality compared to algorithms that do not consider the SOS variation at all.

Here, the SOS distribution employed for the PBP is convolved with a Gaussian filter of increasing variance. This attempt specifically aims for investigating the robustness of a reconstruction for a decreasing resolution of a hypothetical SOS reconstruction. The filter kernel was normalized in order not to scale the SOS distribution during blurring. Gaussian noise was added to the measurement data resulting in an SNR of −9 dB. The reconstruction results with a Gaussian convolution kernel of 1 mm (Fig. 5.5.2-e,f) and 3 mm (Fig. 5.5.2-g,h) full width at half maximum (FWHM) are compared to the reconstruction results with perfectly known SOS (Fig. 5.5.2-c,d) and to a standard reconstruction (Fig. 5.5.2-a,b). The filter kernels are depicted in Figure 5.5.1.

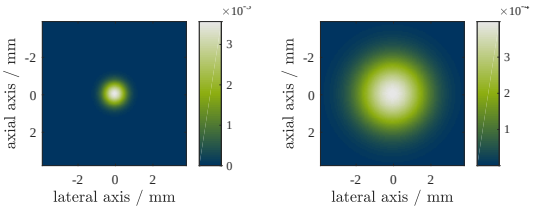

Figure 5.5.1: Normalized lowpass filter kernels with Gaussian distribution; 1 mm FWHM (a), 3 mm FWHM (b)

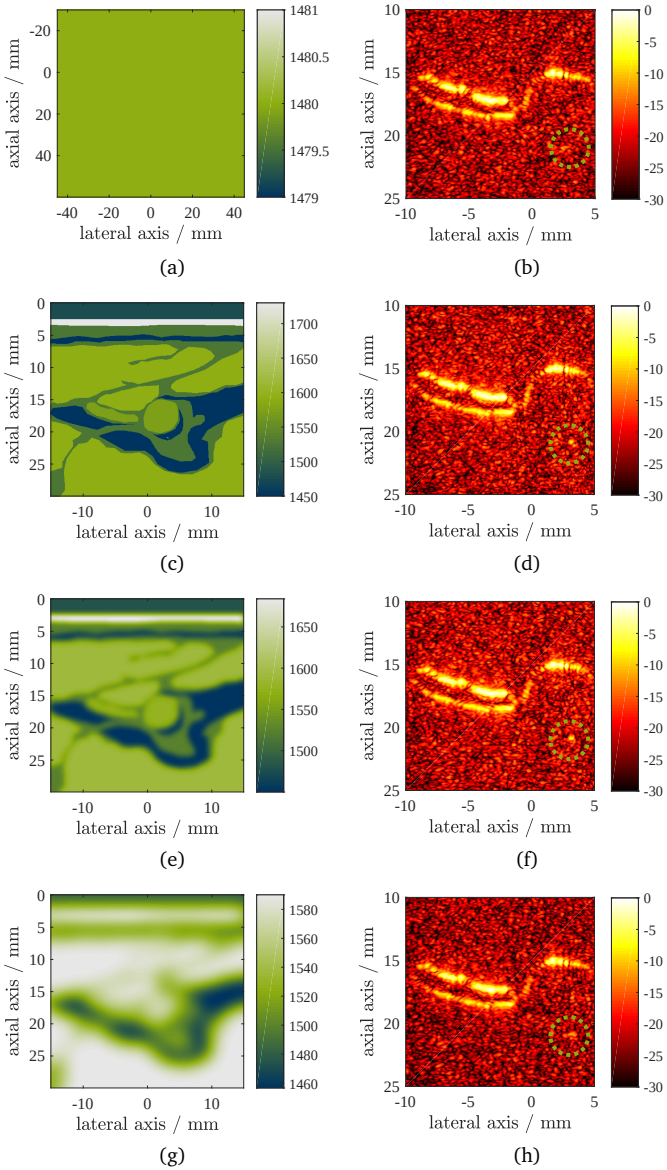

Figure 5.5.2: Comparison of different stages of blurring of the SOS distribution during PBP reconstruction; SOS distributions: homogeneous (a), no blurring (c), 1 mm blurring (e), 3 mm blurring (g), respective PA reconstructions in dB (b,d,f,h)

In this example, the hemorrhage at $(3.1, 20.8)$ mm can hardly be seen in the standard reconstruction, while it is clearly visible in the PBP image with a perfectly known SOS distribution. Using the blurred distribution with 1 mm FWHM filter yields a reconstruction, where the hemorrhage is still clearly visible. Even with 3 mm FWHM blurring, the hemorrhage still peaks out of the background noise but is seemingly distorted.

5.5.2 Combination with a Speed of Sound Reconstruction[2]

The fact that an SOS distribution of low resolution might be sufficient to improve the image quality of the PA reconstruction arises the question if reconstructed SOS distributions might achieve comparable results. Therefore, the accuracy of a paraxial back propagation based on an SOS distribution that is generated by reflection ultrasound tomography (CUTE), as introduced by Jaeger et al. [87], is investigated. Again, simulations were used to generate both PA and plane wave US measurement data using a numerical phantom as depicted in Figure 5.5.3a and Figure 5.5.3b. In CUTE, the SOS distribution is estimated from phase shifts in US data from different transmit waves. For this experiment, 13 plane wave measurements were simulated with transmit angles between $-30°$ and $30°$ in steps of $5°$. Each of these sets is a linear combination of 11 adjacent plane waves in $0.5°$ steps. The regularization parameter for the Tikhonov problem inversion was set to $7.5 \cdot 10^{-2}$. The CUTE reconstruction result is depicted in Figure 5.5.3c. While the lateral shape of the SOS inclusions could be restored fairly accurately, the axial shape appears blurred.

[2] Some text passages in this section were published in [153] © 2017 IEEE. The CUTE reconstructions were performed by M.Sc. Andreas Ihrig (Ruhr-Universität Bochum).

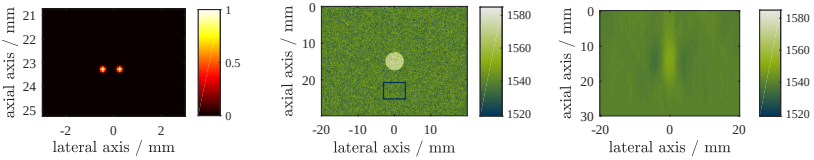

Figure 5.5.3: Numerical “point-source” phantom with single SOS inclusion and CUTE reconstruction; magnified PA source distribution (a), SOS distribution with ROI of PA sources (b), SOS distribution reconstructed with CUTE (c)

Accordingly, photoacoustic data was generated and reconstructed using a homogeneous reconstruction (Fig. 5.5.4-a), using the paraxial back propagation with the actual SOS distribution (Fig. 5.5.4-b) and using the paraxial back propagation with the SOS distribution returned by the CUTE reconstruction (Fig. 5.5.4-c). The results were compared to the actual source distribution (Fig. 5.5.3-a).

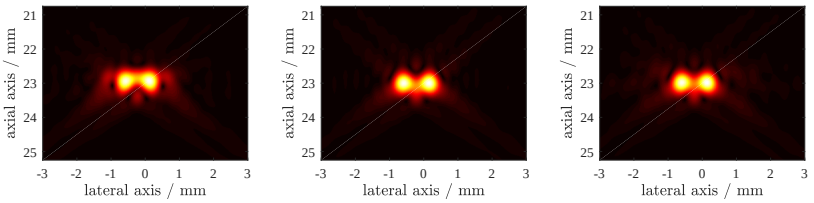

Figure 5.5.4: Comparison of PA reconstruction results of “point-source” phantom with single SOS inclusion; standard reconstruction (a), PBP with actual SOS distribution (b), PBP with reconstructed SOS distribution (c)

While the sources in the homogeneous reconstruction are misplaced and blurred, the paraxial back propagation maps the sources onto the correct locations and does not exhibit any visible side lobes. Even though the CUTE

reconstruction is not perfect, the PA reconstruction results based on the CUTE SOS distribution match those, where the actual SOS distribution was employed, very well. As CUTE computes SOS distributions according to phase changes, the reconstructed distribution might succeed in applying the correct phase delays during PA back propagation, even though the underlying SOS reconstruction is imperfect.

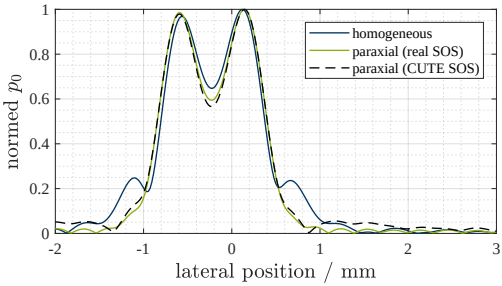

(a)

Figure 5.5.5: Comparison of profiles through point sources in the standard reconstruction, in the PBP reconstruction with actual SOS distribution and in the PBP reconstruction with the estimated SOS distribution

5.5.3 In Vivo Example[3]

The PA reconstruction by paraxial back propagation was validated on data from an in vivo experiment. The entire measurement was planned and executed by the staff at the European Institute for Molecular Imagig (EIMI) in Münster and the respective data sets were made available for this dissertation. Photoacoustic and B-mode ultrasound images were acquired using a preclinical ultrasound system (Vevo 2100, Fujifilm VisualSonics Inc., Toronto, Canada) and a tunable (680–970 nm) OPO laser platform (VevoLAZR, Fujifilm VisualSonics Inc., Toronto, Canada). Light pulses of approximately 15 ns were delivered through optical fibers terminating in the head of an LZ-550 ultrasound transducer (Fujifilm VisualSonics Inc., Toronto, Canada, center frequency: 40 MHz, bandwidth: 32–55 MHz). PA images were taken with pulse energies < 30 mJ. In

[3]Some text passages in this section were published in [153] © 2017 IEEE

vivo PA imaging was performed on a single male 17-week old C57/BL6 mouse anaesthetized with isoflurane (1.2–1.7% v/v in O2). All experiments were performed in accordance with the German Laws for Animal Protection and were approved by the local authority (North Rhine-Westphalia State Agency for Nature, Environment and Consumer Protection).

The acquired B-mode images were employed to estimate the SOS distribution. Therefore, two areas were segmented in the B-mode image, one background area representing the surrounding ultrasound gel and one tissue area. The segmentation was acquired as threshold gray value segmentation with the threshold at 1 % maximum image intensity followed by a morphological closing operation using a disc-shaped structure element of 16 pixels radius. Two standard values for the SOS were assigned to the resulting areas, 1480 m/s for ultrasound gel and 1540 m/s for tissue. The B-mode US image and the resulting approximated SOS distribution are shown in Figure 5.5.6.

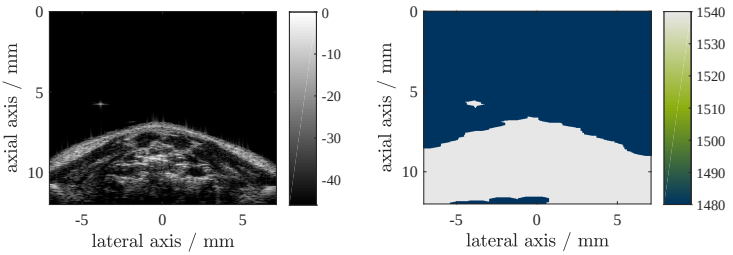

Figure 5.5.6: B-mode US image on log-scale in dB (a) and SOS distribution in $\frac{\mathrm{m}}{\mathrm{s}}$ segmented from the B-mode image (b)

The results of a homogeneous PA reconstruction using only the SOS value of tissue in comparison to the paraxial back propagation using the approximated SOS distribution are depicted in Figure 5.5.7. As first impression, one can notice that the homogeneous reconstruction appears more noisy. This can be explained by the fact that peak sources, such as small vessels, have a reduced amplitude when being blurred by aberrations, which reduces the lower threshold for a fix dynamic range and thus includes more noise. In addition, the shapes of certain structures in the paraxial reconstruction meet

the expectations better than in the standard reconstruction. For instance, the carotid artery, which is depicted in Figure 5.5.8-b and 5.5.8-e, appears more circular using the paraxial reconstruction. Also, small sources that might be assigned to vessels, such as the one in Figure 5.5.8-a and 5.5.8-d, appear as a bow in the standard reconstruction but are point shaped in the paraxial reconstruction. Two overlay images of PA data on US data comparing the homogeneous reconstruction to the paraxial back propagation are shown in Figure 5.5.9.

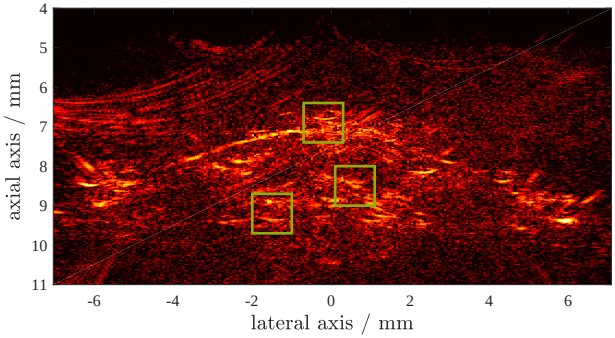

(a)

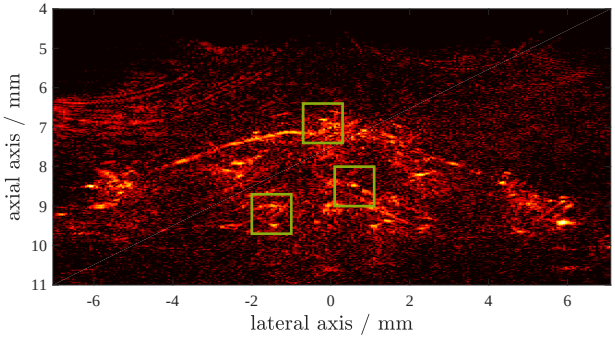

(b)

Figure 5.5.7: Comparison of reconstruction results of in vivo images on log-scale (dynamic range: 30dB); standard reconstruction (a), PBP using SOS distribution segmented from B-mode image (b), green frames signify the ROIs that are magnified in Fig. 5.5.8

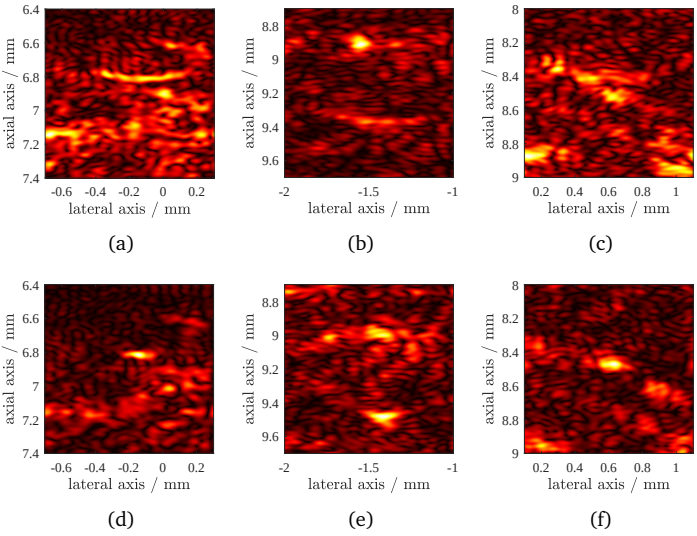

Figure 5.5.8: Magnified ROIs of Fig. 5.5.7 on a linear intensity scale; ROIs in standard reconstruction (a-c), respective ROIs in PBP reconstruction (d-f)

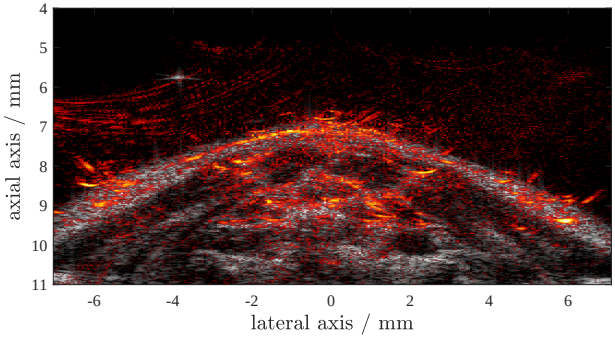

(a)

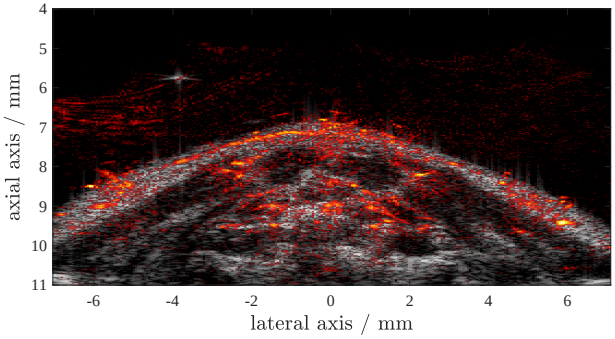

(b)

Figure 5.5.9: Comparison of reconstruction results of in vivo images on log-scale (dynamic range: 30dB) as overlay image PA over B-mode US; standard reconstruction (a), PBP using SOS distribution segmented from B-mode image (b)

5.6 Discussion and Conclusions

As a new approach to reduce aberration artifacts in PA imaging, a back propagation model based on a paraxial approximation of the wave equation was introduced in this chapter. The method is called paraxial back propagation (PBP) and uses a Fourier split step to separate diffraction and refraction processes during the back propagation of a PA measurement. While the diffraction

step assumes the wave to propagate in a homogeneous medium, the refraction step corrects the wave fronts according to the mediums heterogeneities but assumes a fix propagation direction. The split step is applied by phase shifts of the wavefield while alternating between lateral space domain and lateral frequency domain, which can be computed with high efficiency by using fast Fourier algorithms. A damping layer at the lateral boundaries was introduced as an alternative to zero padding, allowing the lateral width to be reduced by almost a factor of two (depending on the geometry). Since the lateral Fourier transform and it's inverse are applied in each axial slice for all temporal frequencies, a reduction of lateral pixels is very beneficial in terms of computation time.

The PBP method requires knowledge about the speed of sound variations within the imaged region. In a first validation step, the exact SOS distribution is assumed to be known to the reconstruction (see section 5.4). For an SOS deviation that was beyond what can be expected from biological tissue, PBP mapped the sources onto the correct locations, while a standard reconstruction that did not consider these deviations generated distorted structures all over the image area (see Fig 5.4.2). The paraxial model produces accurate results for strong SOS deviations despite the fact that it has a predominant propagation direction. The directivity of linear array transducers might play a role in this, since laterally propagating waves cannot be measured efficiently, such that the predominant propagation in axial direction might be sufficient.

Two other reconstruction approaches that can account for SOS deviations were compared to PBP, both of which, at least in this implementation and for the tested geometry, require more computation time by about one order of magnitude (see Fig. 5.4.2). A ray tracing algorithm based on a delay-and-sum reconstruction with adjusted delays was not able to restore the shape of two close point sources in a highly scattering medium. The reason for these strong remaining aberrations might be assigned to the inaccurate refraction model, which is discussed in [44]. However, there, the conclusion is drawn that for most biological tissues, the SOS deviations are not strong enough, such that the simple refraction model is still valid. The PBP was also compared to time reversal, which is a strongly model based approach which simulates the back propagation of a PA measurement including multiple reflections. In terms of image quality, time reversal and PBP achieved similar results (see Fig. 5.4.2). In an additional experiment, it was shown that time reversal might improve the resolution due to back reflected waves (see Fig. 5.4.3). At the same time, back reflection also lead to additional artifacts during time reversal back propagation, which can be explained by the lack of the wavefield that was not

back propagated due to the limited view. PBP, however, which does not account for back reflection, does not introduce these additional artifacts. Considering that the chosen SOS deviations are very strong and both the improvement in resolution due to back reflection and the artifacts due to back reflection only have a small effect, it can be stated that back reflection effects will not be of huge relevance for biological tissue. One point to consider, however, is that, for large intensity differences in PA sources, weak back reflections might already play an important role, since the resulting artifacts might obscure low intensity sources.

In a study with a realistic tissue mimicking numerical phantom, the aberrations were not strong (see Fig. 5.4.5). Still, a standard reconstruction dislocated and blurred sources, while PBP recovered the actual shapes accurately. In the chosen example, the hemorrhage peaked out of the noise in the PBP reconstruction but was not visible in the standard reconstruction (see Fig. 5.4.6).

The approach's applicability without exact knowledge about SOS distribution was also investigated. First, the algorithms robustness to inaccurate SOS data was assessed (see Fig. 5.5.2). To a certain degree, badly resolved SOS distributions were sufficient to still benefit from PBP compared to a standard reconstruction. This indicates that other SOS reconstruction methods or even segmentation of the US images with adequate SOS values assigned to specific areas might be sufficient. In the tested scenario, the resolution was decreased to 1 mm and to 3 mm FWHM. According to [87, p.12], this matches the range of resolution that can be expected from an SOS reconstruction using the CUTE algorithm. First results of PBP based on an SOS distribution estimated by CUTE generated promising results (see Fig. 5.5.4). In the given experiment, a comparison of PBP using the actual SOS distribution and using a distribution estimated by CUTE returned almost similar results, even though the two SOS distributions differed seemingly. As CUTE attempts to find an SOS distribution that minimizes phase delays, the result might produce correct phases of the backpropagated PA wave, even though the SOS distribution is not correct. However, it should be considered that the stronger the aberration become, the more difficult it will become to apply CUTE for the SOS estimation, as CUTE is restricted to small phase shifts.

Finally, both the applicability and the benefit to in vivo data was shown using preclinical measurements from the European Institute of Molecular Imaging in Münster (see Fig. 5.5.7). By separating areas of ultrasound gel and biological tissue by threshold segmentation followed by a morphological operation, a straight forward process to approximate an SOS distribution was presented. In the given measurement with a large ultrasound gel layer on top of the tissue,

the application of PBP made a significant difference to the results of a standard reconstruction. More advanced segmentation approaches separating different kinds of tissue based on their respective speckle pattern are imaginable and might improve the aberration correction.

In summary, paraxial back propagation is an efficient way to account for strong aberrations in PA imaging, in case any information about the SOS deviations in the imaged region can be made available. The information does not have to be very precise and can be derived from US methods. However, aberrations in biological tissue, at least for soft tissues, are usually small, such that less model based methods might be sufficient. Still, compared to a ray tracing algorithm, PBP was computed much faster and might therefore be a convincing choice.

6

Reflection-Compensating Reconstruction

The paraxial back propagation that was introduced in chapter 5 has been shown to compensate for aberrations, but cannot reduce clutter artifacts (see section 3.2.3 for a detailed description of the origins of clutter). While for the compensation of aberrations, the heterogeneity map can be imperfect to a certain degree (see chapter 5.5.1), the results of chapter 4.3.1 indicate that a very accurate map is needed for the compensation of reflections. State of the art approaches that address the reduction of clutter have been listed in chapter 3.2.3.

In the following chapter, a new approach to reduce clutter artifacts is presented that does not require additional hardware and can be integrated on any PA system that allows for the acquisition of plane wave (PW) ultrasound reflection measurements in addition to the PA measurements. For the method to work, all PA sources need to be located within the field of view. For a one dimensional linear array, this implies that the tissue has to be illuminated beneath the transducer, for example by applying a transparent acoustic standoff when illuminating from the side of the transducer. In contrast to other methods that use information from reflection ultrasound data to identify clutter artifacts, this approach operates in the temporal and spatial frequency domain. Exploiting relations between the respective quantities in the frequency domain, the algorithm can be implemented with high computational efficiency. The findings presented in this chapter have been published in [151, 152, 154].

6.1 The Photoacoustic Frequency Domain Scatter Model[1]

The quantities used in the following derivation can be divided into functions of $\mathbf{r} = (x, z) \in \Omega$ in the object space $\Omega \subset \mathbb{R}^2$ and functions of $(x, t) \in \delta\Omega \times [0, T]$ in the measurement space $\delta\Omega \times [0, T] \subset \mathbb{R}^2$. For the latter, measurements will be restricted to pressure signals on the line $z = 0$, which is assumed to be the location of a linear array sensor. This implies quantities in the object space to equal 0 for $z \leq 0$.

Quantities in object space are the initial pressure distribution $p_0(\mathbf{r})$, which is aimed for in the PA reconstruction, and the acoustic medium properties compressibility variation $\gamma_\kappa(\boldsymbol{r})$ and mass density variation $\gamma_\rho(\boldsymbol{r})$ (see (2.1.17) for a definition).

The first quantity in the space of measurements is the plane wave ultrasound measurement, which is described by $p_m^{(us)}(x, t, \vartheta)$. Here, ϑ is the transmit angle and is defined to equal 0 for a propagation into x-direction and to equal $\pi/2$ for a propagation into z-direction. The second quantity in the space of measurements is the photoacoustic measurement data set $p_m(x, t)$. Now, p_m is treated as a superposition of the pure photoacoustic measurement $p_m^{(h)}$, that would have been received in a homogeneous medium, and the measurement of the scattered wave $p_m^{(sc)}$:

$$p_m(x, t) = p_m^{(h)}(x, t) + p_m^{(sc)}(x, t) \tag{6.1.1}$$

A general solution to the scattered wavefield $p_{sc}(\mathbf{r}, k_t)$ that results from scattering of an incoming wave p_{in} at the heterogeneities γ_ρ and γ_κ in the temporal frequency domain reads as [49, p. 235]:

$$\begin{aligned} p_{sc}(\mathbf{r}, k_t) = &-k_t^2 \int_\Omega \gamma_\kappa(\mathbf{r}') p_{in}(\mathbf{r}', k_t) g_\gamma(\mathbf{r}, \boldsymbol{r}', k_t) d\boldsymbol{r}' \\ &+ \int_\Omega \gamma_\rho(\mathbf{r}') \big(\nabla p_{in}(\mathbf{r}', k_t)\big) \cdot \nabla g_\gamma(\mathbf{r}, \boldsymbol{r}', k_t) d\boldsymbol{r}'. \end{aligned} \tag{6.1.2}$$

Here, $g_\gamma(\boldsymbol{r}, \boldsymbol{r}', k_t)$ is the full wave Green function as introduced in (3.1.7) (see chapter 3.1 for more information). This relation can be used to model the forward propagation in a plane wave ultrasound (PWUS) measurement $p_m^{(us)}$ if the incoming wave is chosen as a plane wave $p_{in}(\mathbf{r}, k_t) := \eta_{us}(k_t) \exp(-ik_t \mathbf{e}_\vartheta \cdot \mathbf{r})$

[1] Some text passages in this section were published in [152] © 2016 OSA

and the pressure is evaluated on the sensor line $\boldsymbol{r}_s = (x, z = 0)$:

$$
\begin{aligned}
&p_m^{(us)}(x, k_t, \vartheta) = \\
&-\eta_{us}(k_t) k_t^2 \int_\Omega \gamma_\kappa(\mathbf{r}') \exp(-ik_t \mathbf{e}_\vartheta \cdot \mathbf{r}') g_\gamma(\boldsymbol{r}_s, \boldsymbol{r}', k_t) d\boldsymbol{r}' \\
&+\eta_{us}(k_t) \int_\Omega \gamma_\rho(\mathbf{r}') \left(\nabla \exp(-ik_t \mathbf{e}_\vartheta \cdot \mathbf{r}')\right) \nabla g_\gamma(\boldsymbol{r}_s, \boldsymbol{r}', k_t) d\boldsymbol{r}',
\end{aligned}
\tag{6.1.3}
$$

where the temporal transfer function η_{us} comprises the electric excitation pulse and the two-way electro-acoustic transfer function of the transducer. The unity vector $\mathbf{e}_\vartheta$ is defined as $\mathbf{e}_\vartheta = (\cos(\vartheta), \sin(\vartheta))$ and points into the direction of the transmitted plane wave (see Fig. 6.1.1).

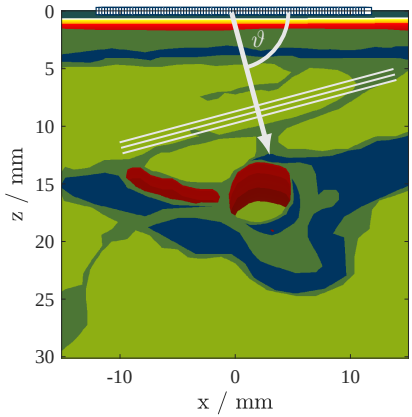

Figure 6.1.1: Carotid artery phantom showing the coordinate system and the orientation of the transmit angle ϑ

As has been shown in chapter 2.2.2, in a homogeneous medium, the photoacoustic source p_0 relates to the photoacoustic measurement p_h as (compare (2.2.4)):

$$
p_m^{(h)}(k_x, k_t) = \frac{k_t \eta_{pa}(k_t)}{2 c_0 \kappa_z} p_0(k_x, \kappa_z)
\tag{6.1.4}
$$

Given the relations between quantities in the space of objects with quantities in the space of measurements in (6.1.3) and (6.1.4), the scattered PA wave will now be modeled with respect to the object functions followed by a substitution by the respective measurement functions. The first step is to decompose the wave that originates in a photoacoustic excitation into plane waves. In the spatial frequency domain, the temporally evolving photoacoustic wave for $t \geq 0$ is described by [33]:

$$p_{in}(k_x, k_{z,} t) = p_0(k_{x,} k_z) \cos(k c_0 t) \tag{6.1.5}$$

with $k = \sqrt{k_x^2 + k_z^2}$ being the magnitude of the spatial frequency vector. The wave is decomposed into plane monofrequent waves in the space domain and temporal frequency domain by Fourier transforms followed by a transform into polar coordinates. Plane waves that propagate into negative $z-$direction, which implies angles of $\vartheta \in]-\pi, 0[$, are considered not to contribute to the reflected clutter wave and are therefore neglected. The incoming wave is then described by:

$$p_{in}(\mathbf{r}, k_t) = -\frac{k_t}{4c_0\pi} \int_0^\pi p_0(-k_t \mathbf{e}_\vartheta) \exp(-i k_t \mathbf{e}_\vartheta \cdot \mathbf{r}) d\vartheta \tag{6.1.6}$$

Here, ϑ accounts for the propagation direction of the individual plane waves in relation to the $x-$axis. This incoming sum of plane waves is plugged into the general solution to the inhomogeneous acoustic wave equation in (6.1.2) as p_{in}:

$$\begin{aligned} &p_m^{(sc)}(x, k_t) = \\ &+ \frac{k_t}{4c_0\pi} \int_0^\pi p_0(-k_t \mathbf{e}_\vartheta) k_t^2 \int_\Omega \gamma_\kappa(\mathbf{r}') \exp(-i k_t \mathbf{e}_\vartheta \cdot \mathbf{r}') g_\gamma(\boldsymbol{r}_s, \boldsymbol{r}', k_t) d\boldsymbol{r}' d\vartheta \\ &- \frac{k_t}{4c_0\pi} \int_0^\pi p_0(-k_t \mathbf{e}_\vartheta) \int_\Omega \gamma_\rho(\mathbf{r}') \left(\nabla \exp(-i k_t \mathbf{e}_\vartheta \cdot \mathbf{r}') \right) \cdot \nabla g_\gamma(\boldsymbol{r}_s, \boldsymbol{r}', k_t) d\boldsymbol{r}' d\vartheta. \end{aligned} \tag{6.1.7}$$

This relation describes the scattered PA measurement as function of the object functions of US and PA imaging. Now the object functions can be replaced by the respective measurement functions to attain a relation relying only on measurable quantities. Comparing (6.1.7) to the plane wave US measurements in (6.1.3), it can be seen that the scattered PA wave can be expressed as a linear combination of PWUS measurements with varying transmit angles:

$$p_m^{(sc)}(k_x, k_t) = -\frac{k_t}{4c_0\pi\eta_{us}(k_t)} \int_0^\pi p_0(-k_t \mathbf{e}_\vartheta) p_m^{(us)}(k_x, k_t, \vartheta) \, d\vartheta \tag{6.1.8}$$

Accordingly, the initial pressure distribution p_0 in (6.1.8) can be expressed by $p_m^{(h)}$ using (6.1.4). For that, it is required to substitute the integration over ϑ with an integration over $k_x^{(\vartheta)} := k_t \cos(\vartheta)$ with $dk_x^{(\vartheta)} = -\kappa_x^{(\vartheta)} d\vartheta$ and $\kappa_x^{(\vartheta)} := k_t \sin(\vartheta)$. This results in an expression of the scattered PA wave relying only on quantities in the measurement space:

$$\boxed{p_m^{(sc)}(k_x, k_t) = -\frac{1}{2\pi\eta_{us}(k_t)} \int_{-k_t}^{k_t} p_m^{(h)}(-k_x^{(\vartheta)}, -k_t) p_m^{(us)}(k_x, k_t, \vartheta(k_x^{(\vartheta)}, k_t)) dk_x^{(\vartheta)}.} \tag{6.1.9}$$

The evaluation of $p_m^{(h)}$ at $(-k_x^{(\vartheta)}, -k_t)$ equals an evaluation of the complex conjugate $p_m^{(h)*}$ at $(k_x^{(\vartheta)}, k_t)$. The angles of the plane waves in the ultrasound measurements depend on the integration variable $k_x^{(\vartheta)}$ by:

$$\vartheta = \cos^{-1}\left(\frac{k_x^{(\vartheta)}}{k_t}\right). \tag{6.1.10}$$

The relation in (6.1.9) does not sufficiently describe a scattered photoacoustic wave in general. Due to the neglection of negative angles in (6.1.6), transmission scattering is not considered. In addition, (6.1.5) is only valid for $t \geq 0$ and returns a converging wave at times $t < 0$. This does not resemble a causal photoacoustic wave propagation initialized at $t = 0$ and falsely creates additional scattering of the converging wave. However, both of these simplifications have low impact on the application for clutter reduction, since the skin, which is the major source for the incoming wave in (6.1.6), is usually located between the sensor and the scatterers.

6.1.1 Considerations for Model Inversion

By expressing p_{sc} as a linear combination of $p_m^{(h)}$ and $p_m^{(us)}$ in (6.1.9), a forward relation mapping $p_m^{(h)}$ onto the actually measurable p_m is straight forward. Substituting (6.1.9) into (6.1.1) yields:

$$p_m = (G_{BP} + 1)\, p_h, \tag{6.1.11}$$

with the backpropagation operator:

$$G_{BP} := -\frac{1}{2\pi\eta_{us}(k_t)} \int_{-k_t}^{k_t} dk_x' p_m^{(us)}(k_x, k_t, \vartheta(k_x', k_t))\mathscr{C}, \tag{6.1.12}$$

where $\mathscr{C}$ is the conjugate operator that maps a complex number onto it's conjugate value, such that $\mathscr{C}x = x^*$. The operator notation is introduced to ensure readability and will be continued in subsequent chapters. The aim is now to find an inversion for (6.1.11), such that p_h can be expressed only by the measurable quantities p_m and $p_m^{(us)}$. The inversion, however, is challenging in many aspects. In the scope of this chapter, two numerical inversion approaches will be introduced that differ in accuracy and computational complexity. First, however, some preliminary considerations about the forward model need to be made.

Spatial Frequency Readout

The first topic to consider is how to read out the ultrasound data in (6.1.9). The integration over the $k_x^{(\vartheta)}$ implies an integration over the transmit angle ϑ. A huge amount of transmissions is required to attain a complete set of ultrasound measurement data that can fulfill (6.1.10) for each frequency vector (k_x, k_t) in $p_m^{(h)}(k_x, k_t)$. This problem is solved by acquiring a fix set of transmissions and by linearly interpolating the measurement data between the acquired angles. Let ϑ be the required angle for a single combination of $k_x^{(\vartheta)}$ and k_t, such that $\vartheta = \cos^{-1}(k_x^{(\vartheta)}/k_t)$ and let ϑ_1 and ϑ_2 be the closest neighboring angles that actually were acquired, then $p_m^{(us)}(\vartheta)$ can be approximated by:

$$p_m^{(us)}(k_x, k_t, \vartheta) \approx (1-w) \cdot p_m^{(us)}(k_x, k_t, \vartheta_1) + w \cdot p_m^{(us)}(k_x, k_t, \vartheta_2), \qquad (6.1.13)$$

where the interpolation weight w calculates as:

$$w = (\vartheta - \vartheta_1)/(\vartheta_2 - \vartheta_1). \qquad (6.1.14)$$

Obviously, the linear interpolation becomes more accurate, the more transmissions are acquired. An advanced interpolation that allows for a significant reduction of the number of required transmissions will be introduced in section 6.4.

Temporal Frequency Matching

The second topic to consider is the matching of the temporal impulse responses of the PA imaging process and the US imaging process. For the PA acquisition, the impulse response η_{pa} comprises the temporal laser pulse shape and the acousto-electric impulse response of the transducer. For the US acquisition, the impulse response depends on the electric excitation pulse, the electro-acoustic

impulse response in transmission and the acousto-electric impulse response in reception, while the later two can be assumed to exhibit reciprocity. The inner product of the homogeneous signal $p_m^{(h)}$ with the ultrasound measurements $p_m^{(us)}$ without filtering:

$$p_{BP} := -\frac{1}{2\pi}\int_{-k_t}^{k_t} p_m^{(us)} p_m^{(h)} dk_x^{(\vartheta)} \tag{6.1.15}$$

returns a quantity p_{BP} that contains both impulse responses η_{us} and η_{pa} (see (6.1.3) and (6.1.4)). According to (6.1.9), the inverse US impulse response has to be applied to p_{BP} before adding it to $p_m^{(h)}$:

$$p_m = p_m^{(h)} + \eta_{us}^{-1} p_{BP}. \tag{6.1.16}$$

Applying η_{us}^{-1}, however, causes trouble for weakly transferred frequencies, especially in the presence of noise. Hence, another approach to account for the US impulse response is required.

Figure. 6.1.2 visualizes how well the back propagated signal p_{BP} reproduces a clutter artifact in the actual signal p_m using different filtering approaches. The data sets for p_m and p_{BP} were generated artificially, such that p_{BP} is a band-filtered version of p_m and white noise of 15 dB SNR was added to both signals. The first approach is to completely ignore η_{us}^{-1}:

$$p_m \approx p_m^{(h)} + p_{BP}. \tag{6.1.17}$$

As depicted in Fig. 6.1.2(a,b), p_{BP} cannot accurately recreate a scatter artifact in p_m, since the frequency ranges differ. Substituting η_{us}^{-1} with the respective Wiener deconvolution filter:

$$\eta_{us}^{(W)} = \frac{1}{\eta_{us}} \frac{\eta_{us}\eta_{us}^*}{\eta_{us}\eta_{us}^* + \frac{1}{SNR}}, \tag{6.1.18}$$

improves the accuracy:

$$p_m \approx p_m^{(h)} + \eta_{us}^{(W)} p_{BP}. \tag{6.1.19}$$

However, when applying $\eta_{us}^{(W)}$, the estimated artifact $\eta_{us}^{(W)} p_{BP}$ and the actual artifact in p_m differ by a filter $\eta_{us}\eta_{us}^* / \left(\eta_{us}\eta_{us}^* + \frac{1}{SNR}\right)$ (see Fig. 6.1.2(c,d)).

Instead of inverse filtering p_{sc}, the entire relation in (6.1.11) can also be filtered with η_{us}:

$$\eta_{us} p_m = \eta_{us} p_m^{(h)} + p_{BP}, \tag{6.1.20}$$

such that no inverse filter is required. While, in this configuration, the frequency ranges of estimated artifact and actual artifact actually match, it comes with the drawback of a reduced bandwidth of the PA signal and hence a reduced resolution the reconstructed PA image after inversion (see Fig. 6.1.2(e,f)). It is therefore required to sacrifice resolution to gain clutter reduction.

Here, a new suggestion is made that is a combination of the two approaches in (6.1.19) and (6.1.20). Instead of applying the full inverse US impulse response η_{us}^{-1}, a windowed version suppressing strongly amplified frequencies $\eta_{win}\eta_{us}^{-1}$ is applied to p_{BP} and the same windowing function is also applied to the PA measurements:

$$\eta_{win}p_m = \eta_{win}p_m^{(h)} + \eta_{win}\eta_{us}^{-1}p_{BP} \tag{6.1.21}$$

The window function η_{win} might be chosen as:

$$\eta_{win} = \frac{\eta_{us}\eta_{us}^*}{\eta_{us}\eta_{us}^* + \frac{1}{SNR}}, \tag{6.1.22}$$

which, again, turns the filter $\eta_{win}\eta_{us}^{-1}$ into a Wiener deconvolution filter like in (6.1.19). However, this time, the frequency content of the actual artifact and the estimated artifact match. The impulse responses of PA and US are not completely different because both are dominated by the electro-acoustic impulse response. Also, the laser pulse shape is usually matched to this spectral range. Hence, windowing the PA measurement with the Wiener filter of the ultrasound impulse response is likely not to reduce the resolution too much, but to significantly reduce noise (Fig. 6.1.2(g,h)).

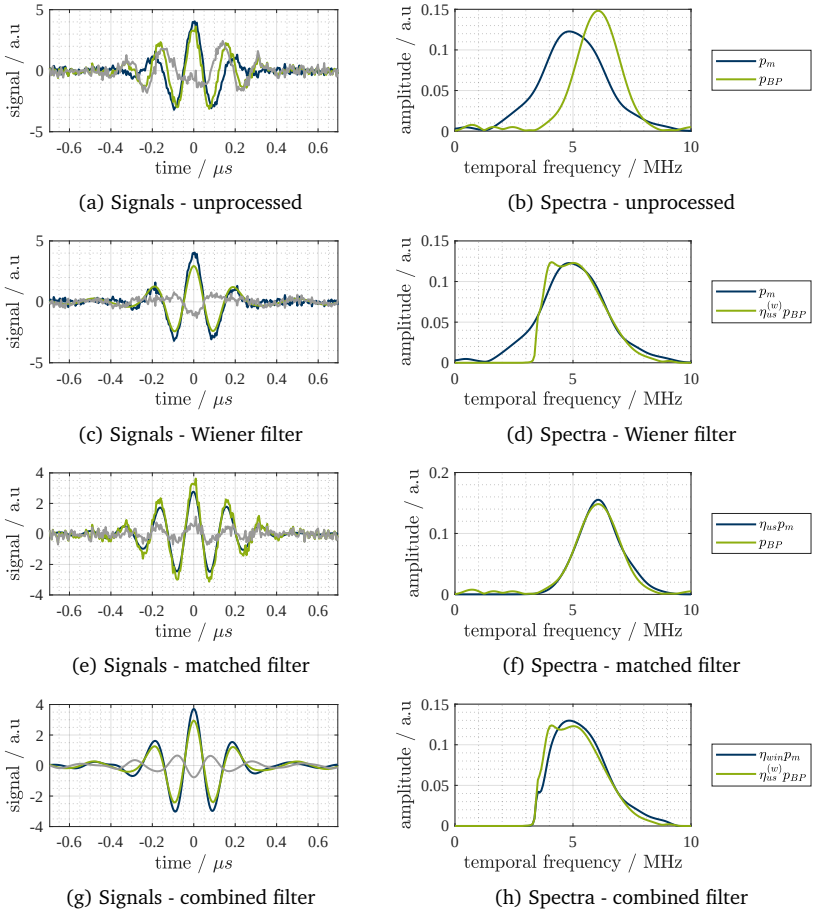

(a) Signals - unprocessed

(b) Spectra - unprocessed

(c) Signals - Wiener filter

(d) Spectra - Wiener filter

(e) Signals - matched filter

(f) Spectra - matched filter

(g) Signals - combined filter

(h) Spectra - combined filter

Figure 6.1.2: Comparison of signal filtering approaches for recreation of a clutter artifact in p_m by a backpropagated homogeneous measurement p_{BP} - the weaker the difference signal (gray line), the better clutter can be reduced.

6.2 Model Inversion by Scatter Estimation

The first approach to invert the forward relation in (6.1.11) is based on a model simplification and is hence expected to lack accuracy. However, other than the inversion model in section 6.3, it does not require the online computation of a matrix inversion. Solving (6.1.11) for $p_m^{(h)}$ yields:

$$p_m^{(h)} = \left(1 + G_{(BP)}\right)^{-1} p_m \tag{6.2.1}$$

with the definition of $G_{(BP)}$ in (6.1.12). Now, applying Neumann series expansion returns:

$$p_m^{(h)} = \sum_{i=0}^{\infty} \left(-G_{(BP)}\right)^i p_m. \tag{6.2.2}$$

Truncating the series after the second term ($i = 1$) makes the proof of convergence of the series needless and results in:

$$p_m^{(h)} \approx \left(1 - G_{(BP)}\right) p_m. \tag{6.2.3}$$

The same result is attained by approximating $p_m^{(h)}$ by p_m in the first summand of (6.1.11). Due to this simplification, clutter artifacts will be treated as sources and will therefore introduce new artifacts, which, however, are of weaker amplitude. Hence, the simplification is valid for weak scattering.

6.2.1 Implementation of the Scatter Estimation

After a discretization of (6.2.3), p_m and $p_m^{(h)}$ are written as vectors for each temporal frequency k_t, while G_{BP} is a matrix that contains interpolated values from the set $\{p_m^{(us)}(\vartheta_1), p_m^{(us)}(\vartheta_2), ..., p_m^{(us)}(\vartheta_n)\}$ at the same temporal frequency. In order to fine tune the result, an additional parameter α is introduced that weights the contribution of the estimated scatter and accounts for different signal amplitudes of PA and US signals:

$$p_m^{(h)} \approx p_m - \alpha G_{(BP)} p_m. \tag{6.2.4}$$

The matrix multiplication has to be applied for each relevant temporal frequency to generate a full data set p_h. After this, p_h is reconstructed, while the reconstruction method might be any standard algorithm (see chapter 2.2). Therefore, a frequency domain reconstruction is suggested (see chapter 2.2.2),

since the data set is already in the Fourier domain. Since the reconstruction is a linear operation, the subtraction in (6.2.3) might as well be applied after reconstructing both p_m and $G_{BP}p_m$. This requires the computation of two reconstructions but allows for more precise fine tuning of α and the temporal frequency matching that was described in section 6.1.1. The flowchart in Fig. 6.2.1 shows how the complete algorithm is implemented, starting at the acquisition of the measurement data for both PA and US and ending at the retrieval of a PA image that is compensated for clutter.

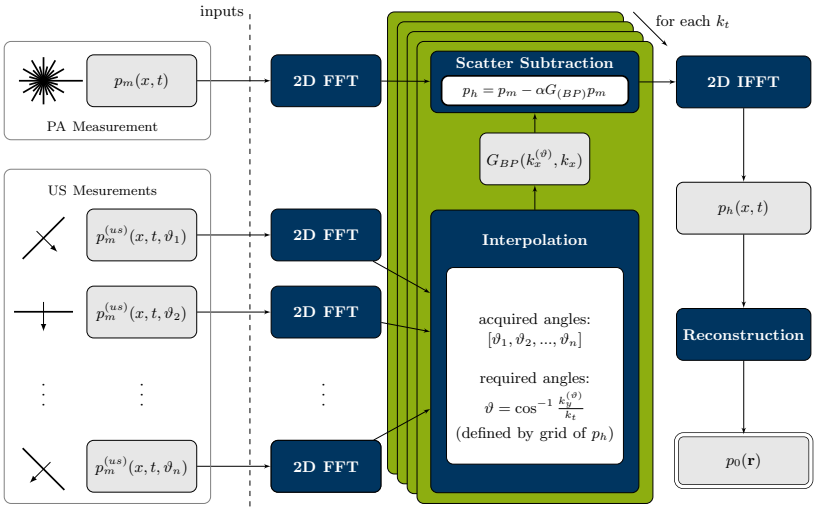

Figure 6.2.1: The clutter reduction algorithm with scatter estimation: PWUS measurements from multiple transmission angles are Fourier transformed, interpolated to to match the readout grid of the PA data, then multiplied with the conjugate of the Fourier transformed PA data set and the product is subtracted from the PA data set. The resulting data set is inversely Fourier transformed and reconstructed, returning an image that is compensated for clutter artifacts.

6.2.2 Results Using Scatter Estimation

The clutter reduction method based on scatter estimation and subtraction is validated in regard to various aspects. First, the general properties of the method are investigated using a dedicated numerical clutter phantom and measurement data based on simulations. To proof the performance in a realistic scenario, a strongly absorbing skin source was added to the numerical carotid artery phantom used in previous chapters.

General Capabilities and Limits

A numerical phantom was designed to demonstrate the general capabilities of the clutter reduction method (see Fig. 6.2.2a). The phantom consists of four different combinations of a point source and a scatterer, which all stress different properties. The left part comprises a point source above a bar shaped density scatterer producing a clutter artifact. The second part matches this configuration with the only difference that at the position, where the artifact is expected, another source is placed that is not supposed to be canceled out with the artifact. The third part of the phantom resembles the first configuration but the density scatterer is replaced by a broad SOS scatterer to assess if a phase shift of the propagating wave is sufficiently considered. In the last part, the source is located beneath the scatterer to assess the expected drawback that, during back propagation, the PA wave is scattered before it actually reaches the source, which might introduce additional artifacts.

The simulated transducer had a center frequency of 3.5 MHz with a fractional bandwidth of 80% and comprised 64 elements with a pitch of 0.15 mm (see top of Fig. 6.2.2a). 101 plane wave measurements were simulated between $-50°$ and $50°$ relative to the z-axis. The laser pulse was modeled as a Dirac delta pulse. The clutter reduction with artifact subtraction was applied using the filtering method in (6.1.21). Afterwards, a Fourier back propagation reconstruction (2.2.12) was applied to both the uncompensated and the compensated data set.

Figure 6.2.2 shows the PA reconstruction with and without clutter reduction (see Fig. 6.2.2-a and Fig. 6.2.2-b, respectively). An artifact power ratio is evaluated as ratio of signal energies with and without compensation in a small region of interest (ROI) around the artifacts. The artifact power ratio of the left reflection is damped by 10.7 dB. The actual source located at the same place as the second reflection artifact is not removed. The clutter artifact underneath the SOS deviation is damped by 3.2 dB. Above the source that

is located underneath the scatterer at position four, a new artifact appears, which can be attributed to a reflection during back propagation before the PA sources are reached. The amplitude of the additional artifact is 12.5 dB lower than the other sources at that depth.

In summary, a successful clutter reduction can be stated, which does not suppress actual PA sources at the location of an artifact but introduces weak additional artifacts for scatterers between the transducer and the PA source.

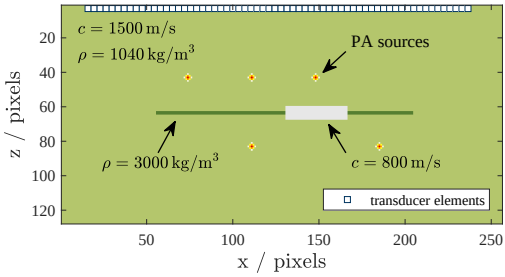

(a)

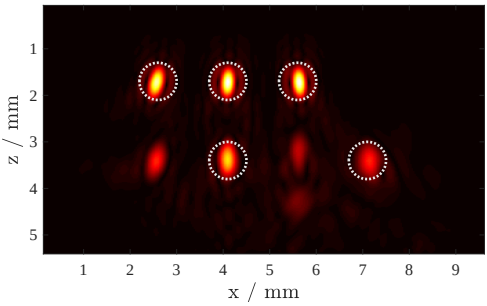

(b)

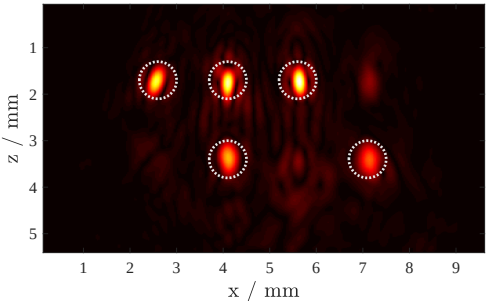

(c)

Figure 6.2.2: Numerical “clutter”-phantom and results for the clutter estimation approach; Overlay image of PA sources (red), SOS distribution (gray) and density distribution (green) (a), PA image without clutter reduction (b), PA images with clutter reduction (c)

Results for Realistic Properties

The numerical "carotid-artery" phantom that was introduced in previous chapters (see Fig. 2.4.2) was adapted to exhibit a strong photoacoustic source in the region of the skin. The phantom is visualized in Fig. 6.2.3 as an overlay image with PA sources on a red color map and the SOS distribution on a blue to green color map. The transducer location is indicated by the squares on the top. The simulated transducer matches the one described in chapter 4.2.3. Gaussian noise was added to the simulated PA measurement data resulting in an SNR of 20 dB. Simulated PWUS measurements were acquired with 81 transmission angles between −40° and 40° in relation to the axial axis.

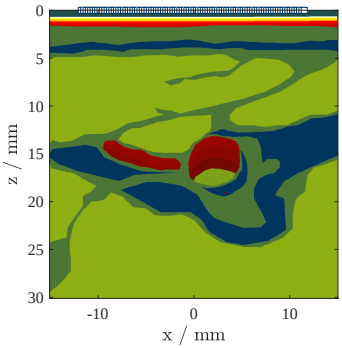

Figure 6.2.3: Numerical "carotid artery"-phantom including skin source as overlay image with PA sources (red) over the SOS distribution (blue to green) and transducer elements indicated by blue squares on top of the image

The uncompensated PA image (Fig. 6.2.4-a) exhibits various clutter artifacts that appear as curved horizontal lines in the upper part and as point-like and circular structures in the center and bottom part. The shape of the carotid artery is hard to determine and the hemorrhage at $(18.9, 3.2)$ mm can barely be distinguished from the artifacts. Figure 6.2.4-b shows the estimated clutter distribution. The image is displayed after envelope detection for visualization purposes, while the subtraction is carried out on high frequency data before envelope detection. In the image with clutter compensation (Fig. 6.2.4-c), all artifacts are damped, while the actual sources appear clearly and no strong

additional artifacts are introduced. The degree of artifact suppression differs in different image areas. While, in the lateral center, most artifacts are completely eliminated, artifacts in the outer lateral regions are still clearly visible. This might be referred to a bad coverage of transmitted waves under steep angles in those regions.

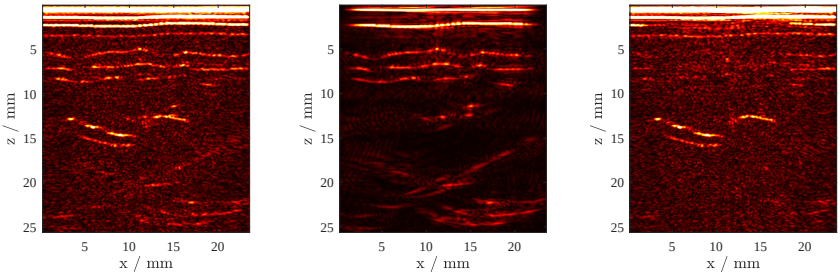

(a) uncompensated (b) clutter estimation (c) compensated

Figure 6.2.4: Clutter reduction by subtraction for numerical "carotid-artery" phantom; uncompensated PA image (a), reconstructed clutter estimation (b), compensated PA image (c)

6.3 The Direct Inversion Approach

As explained in section 6.1.1, analytically solving the relation in (6.1.11) for $p_m^{(h)}$ is challenging. However, as alternative to a the scatter estimation approach in section 6.2, a solution to $p_m^{(h)}$ can be computed by a numerical inversion minimizing the error functional:

$$e = \left|\left(1 + G_{(BP)}\right) p_m^{(h)} - p_m\right|^2 \tag{6.3.1}$$

In contrast to the scatter estimation approach, a numerical inversion does not simplify the model in (6.1.11). However, the computational effort increases. The inverse of $(1 + G_{(BP)})$ cannot be precomputed and reapplied to other frames, as it depends on the US measurements referring to the current frame. Fortunately, due to the formulation in the temporal frequency domain, the

solution to (6.3.1) can be computed for each temporal frequency independently. Compared to a model, where a single model matrix is computed and inverted, applying several inversions of small matrices is computationally efficient. In addition, applying an inversion allows for a simple inclusion of regularization.

6.3.1 Implementation of the Direct Inversion

While the discretization of p_m and $p_m^{(us)}$ is the same as for the clutter estimation, a direct inversion requires more effort for the computation of G_{BP} with respect to the complex conjugation in (6.1.12). In the scatter estimation model (see (6.2.3)), it is straightforward to compute both p_m and p_m^* to find a solution to $p_m^{(h)}$. However, in the inversion model in (6.3.1), the complex conjugation has to be considered in the operator $G_{(BP)}$ to be able to find an inverse to $(1 + G_{(BP)})$. Therefore, it is necessary to switch from the operator notation to a vector-matrix notation. The matrix $\underline{\underline{P_m^{(us)}}}$ is introduced, where each element (a, b) computes as:

$$P_{m\,(a,b)}^{(us)} := p_m^{(us)}(a \cdot \Delta k_x, k_t, \vartheta(b \cdot \Delta k_x^{(\vartheta)}, k_t)) \tag{6.3.2}$$

with Δk_x and $\Delta k_x^{(\vartheta)}$ denoting the lateral frequency steps of p_m and the desired $p_m^{(h)}$, respectively. The entire forward problem in vector-matrix notation reads as:

$$\underline{p_m} = \underline{p_m^{(h)}} + \underline{\underline{P_m^{(us)}}}\,\underline{p_m^{(h)*}}. \tag{6.3.3}$$

Now the fact that both the vector $\underline{p_m^{(h)}}$ and its complex conjugate $\underline{p_m^{(h)*}}$ appear in the forward relation can be considered by completely separating the real part and the imaginary part of $\underline{p_m}$ and $\underline{p_m^{(h)}}$, which increases the number of elements of the respective model matrix by a factor of four. The respective forward model reads as:

$$\begin{pmatrix} \Re\underline{p_m} \\ \Im\underline{p_m} \end{pmatrix} = \begin{pmatrix} \Re\left[\underline{\underline{I}} - \alpha\underline{\underline{P_m^{(us)}}}\right] & -\alpha\Im\underline{\underline{P_m^{(us)}}} \\ -\alpha\Im\underline{\underline{P_m^{(us)}}} & \Re\left[\underline{\underline{I}} + \alpha\underline{\underline{P_m^{(us)}}}\right] \end{pmatrix} \cdot \begin{pmatrix} \Re\underline{p_m^{(h)}} \\ \Im\underline{p_m^{(h)}} \end{pmatrix} \tag{6.3.4}$$

with $\underline{\underline{I}}$ being the unity matrix and $\mathfrak{R}$ and $\mathfrak{I}$ being the real part operator and imaginary part operator with $\mathfrak{R}x = \frac{1}{2}(x + x^*)$ and $\mathfrak{I}x = \frac{1}{2}(x - x^*)$. Now, the matrix in (6.3.4) is ready for numerical inversion. To guarantee a fast and stable computation, a least square solution is implemented to solve (6.3.4) for $\mathfrak{R}\underline{p_m^{(h)}}$ and $\mathfrak{I}\underline{p_m^{(h)}}$, which are combined to a complex vector $\underline{p_m^{(h)}}$ afterwards.

A flow chart showing how the direct inversion approach was implemented is shown in Fig. 6.3.1. The algorithms resembles the one in Fig. 6.2.1, except for the way how G_{BP} is processed to retrieve $p_m^{(h)}$ (see "numerical inversion"-block in Fig. 6.3.1).

The approach of direct inversion allows for simple integration of regularization. Tikhonov regularization is applied by adding an L_2-norm to the error functional of (6.3.1) in combination with a regularization parameter β:

$$e = \left|\left(1 + G_{(BP)}\right) p_m^{(h)} - p_m\right|^2 + \beta \left|L p_m^{(h)}\right|^2, \tag{6.3.5}$$

where L is a linear operator. Here, L is chosen as unity operator, such that the L_2 norm of $p_m^{(h)}$ is minimized. The regularization term can be integrated into the matrix notation in (6.3.4) by concatenating the matrix $\sqrt{\beta}L$ to the system matrix and concatenating a zero-vector to the vector $\underline{p_m}$ [126]. Increasing β suppresses the false amplification of noise in the returned vector as the regularization ensures small values for $p_m^{(h)}$.

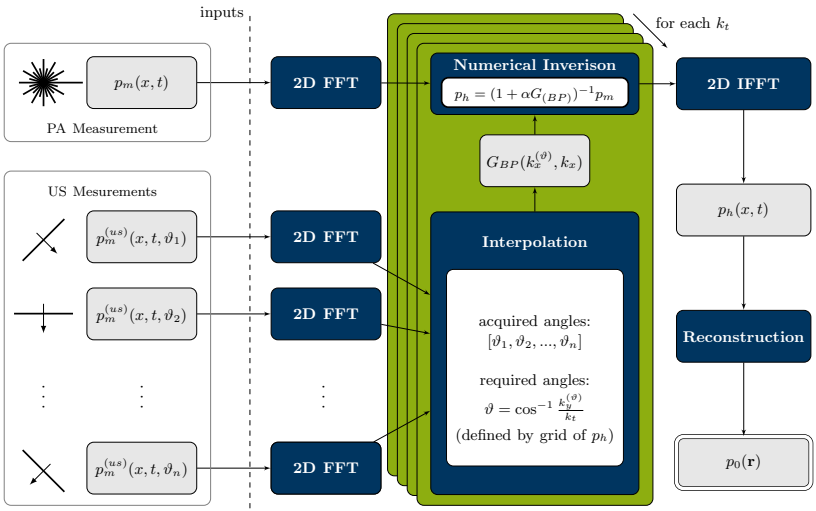

Figure 6.3.1: The clutter reduction algorithm with direct inversion: PWUS measurements from multiple transmission angles are Fourier transformed, interpolated to to match the readout grid of the PA data, then the resulting matrix is inverted using a pseudo-inverse and multiplied to the Fourier transformed PA data set. The resulting data set is inversely Fourier transformed and reconstructed, returning an image that is compensated for clutter artifacts.

6.3.2 Results Using Direct Inversion

As for the clutter reduction by scatter estimation and subtraction, the general capabilities of numerical inversion were assessed using the numerical "clutter"-phantom as well as the capabilities in a realistic scenario using the numerical "carotid-artery" phantom.

General Capabilities and Limit

The same numerical phantom as in section 6.2.2 was employed to validate the clutter reduction by direct inversion (see Fig. 6.3.2a). Here, the left artifact was reduced by 7.9 dB, according to the artifact power ratio (see section 6.2.2 for definition). The actual source beneath the artifact at the second location

has not been eliminated. The artifact power beneath the SOS scatterer at location three was damped by 4.3 dB. Again, an additional artifact of low amplitude (10.9 dB less than the sources) is introduced at location four.

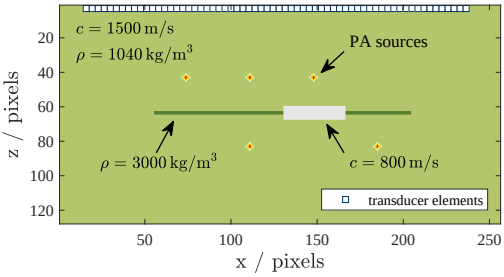

(a)

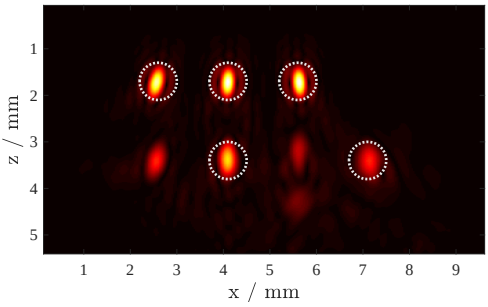

(b)

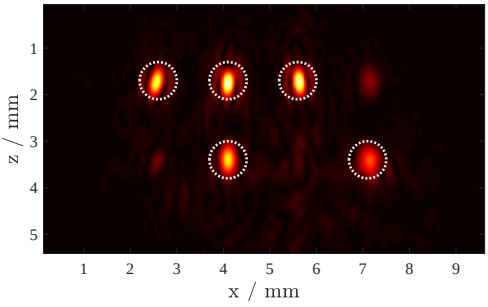

(c)

Figure 6.3.2: Numerical “clutter”-phantom and results for the direct inversion approach; Overlay image of PA sources (red), SOS distribution (gray) and density distribution (green) (a), PA image without clutter reduction (b), PA images with clutter reduction (c)

Results for Realistic Properties

As for the clutter subtraction method, the "carotid artery"-phantom (see Fig. 6.2.3) was also used to assess the direct inversion method. The same simulated measurement data with the same level of noise (SNR = 20 dB) was used as well as the same simulated PWUS measurements with 81 transmission angles between −40° and 40° in relation to the axial axis. As described in section 6.3.1, Tikhonov regularization was employed with a regularization factor of 2. The reconstruction results with and without clutter reduction are depicted in Fig. 6.3.3. Again, most clutter artifacts are sufficiently suppressed and the hemorrhage is clearly visible after clutter reduction was applied. However, the clutter reduction is less accurate in the outer regions in lateral direction.

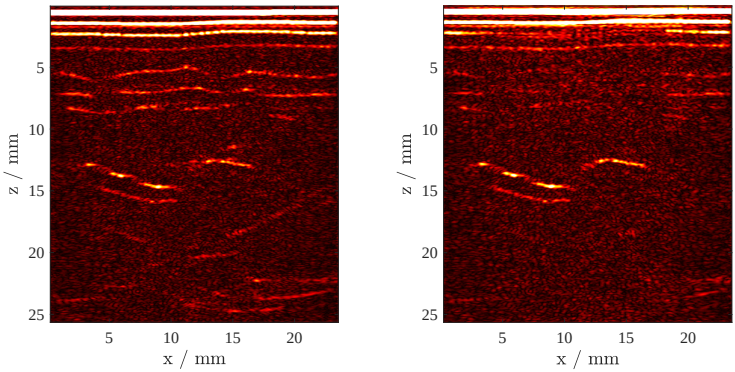

(a) uncompensated (b) compensated

Figure 6.3.3: Clutter reduction by direct inversion for numerical "carotid-artery" phantom; uncompensated PA image (a), compensated PA image (b)

6.4 Reducing the Amount of Required Transmit Angles[2]

For the clutter reduction to work properly, a high number of plane wave measurements is required. In (6.1.9), almost every combination of k_t and $k_x^{(\vartheta)}$ results in a unique value for the transmission angle $\vartheta = \cos^{-1}(k_x^{(\vartheta)}/k_t)$. This implies that the number of required transmission angles is in the order of the number of acquired data points per PA measurement. In terms of data acquisition, data storage, data transfer and data processing capacities, this is far beyond what can be expected from state-of-the-art ultrasound hardware. Therefore, the measurement data of missing angles need to be interpolated from the data provided by neighboring angles according to section 6.1.1. In the following, a new approach is introduced that performs an interpolation in the frequency domain of the US image rather than an interpolation in the domain of the measurements. By transforming the acquired data into the object space using Fourier domain diffraction theory, redundancies in the content of the data obtained from different angles can be exploited.

6.4.1 Object space Interpolation

A frequency grid of the plane wave US measurement data in the temporal and spatial frequency domain $p_m^{(us)}(k_x, k_t, \vartheta)$ is depicted in Fig. 6.4.1-a. It shows only the positive temporal side band, which, however, contains all necessary information. All frequency axes are scaled by the sampling wave number $k_t^{(s)} := 2\pi c_0^{-1} f_s$ with f_s as temporal sampling frequency. In Fig. 6.4.1-b, the conventional linear interpolation process is demonstrated, where the green grids represent the measurement data under two angles that were mapped into the object space and the blue grid represents the readout positions of measurement data under the desired angle. The following new interpolation approach can be interpreted as an ultrasound reconstruction followed by a forward ultrasound propagation of the wavefield that results from the transmission of the desired angle. Since this reconstruction and this forward propagation are executed in the frequency domain, they are computed as simple remapping operations.

[2]Some text passages in this section were published in [154] © 2016 IEEE

According to linear diffraction theory, plane wave RF data sets of different transmit angles exhibit redundancies. That is due to the fact that different combinations of an emitted and a received monofrequent plane wave can carry the same information about the scattering object. These redundancies can be exploited to deduce a plane wave measurement of a certain transmit angle by referring to the measurements from other angles. Since one pair of emitted and received monofrequent plane waves corresponds to one particular spatial frequency of the scatterer distribution, the interpolation can be carried out in the k-space of the scatterer distribution, which is hereinafter referred to as object space. Mathematically, this relation between the US measurement $p_{us}(k_y, k_t, \vartheta)$ and the scatterer distribution $\gamma(k_y, k_z)$ can be expressed in the frequency domain [48, 115, 147] by:

$$p_m^{(us)}(k_x, k_t, \vartheta) = \frac{jk_t^2}{2\kappa_z}\gamma(k_x + k_t\cos(\vartheta), \kappa_z + k_t\sin(\vartheta)). \tag{6.4.1}$$

Here, $\gamma(k_x, k_z)$ is a general scatterer distribution and thus the object to be reconstructed in ultrasound imaging. To be exact, (6.4.1) is a simplified version of the actual relation that only considers heterogeneities in the compressibility and not in the mass density of the observed object. A more precise model is presented in [147]. It should also be noted that the relation is based on the Born approximation and is hence rather valid for weakly scattering media.

Eq. (6.4.1) can be used to reconstruct an estimation of the scatterer distribution $\hat{\gamma}(\boldsymbol{r})$ from a set of plane wave measurements $\{p_m^{(us)}(\vartheta_1), ..., p_m^{(us)}(\vartheta_n)\}$. In fact, any other plane wave reconstruction algorithm can be used as well to retrieve $\hat{\gamma}(\boldsymbol{r})$. Substituting (6.4.1) into (6.1.9) and applying it to the estimated scatterer distribution $\hat{\gamma}(\boldsymbol{r})$ yields a modified scatter model:

$$p_m^{(sc)}(k_x, k_t) = -\frac{jk_t^2}{4\pi\kappa_z}\int_{-k_t}^{k_t}\hat{\gamma}(k_x + k_x^{(\vartheta)}, \kappa_z + \kappa_z^{(\vartheta)})p_m^{(h)}(-k_y^{(\vartheta)}, -k_t)\,dk_x^{(\vartheta)}, \tag{6.4.2}$$

where $\kappa_z^{(\vartheta)}$ is defined in analogy to κ_z as $\kappa_z^{(\vartheta)} = \mathrm{sgn}(k_t)\sqrt{k_t - k_x^{(\vartheta)}}$. In consequence, the acquired RF data can simply be mapped onto the grid in the object space and the required angles can be read out successively. This is illustrated in Figure 6.4.1-c, where the measurements of the two acquired angles ϑ_1 and ϑ_2 are mapped onto the grid of γ and the RF data of the angle ϑ are read out. It has to be considered that the filter term $-jk_t^2/(4\pi\kappa_z)$ needs to be multiplied with the RF data when it is mapped into the object k-space and that a respective inverse filter needs to be multiplied to the measurement data, when it is read out.

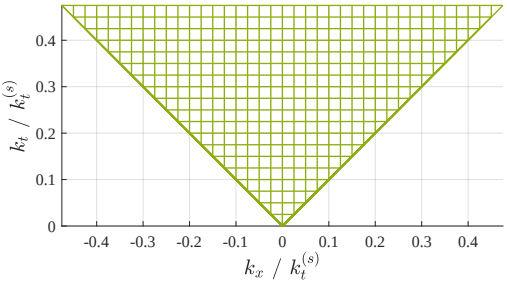

(a) Frequency grid of US measurement data $p_m^{(us)}(k_x, k_t, \vartheta)$

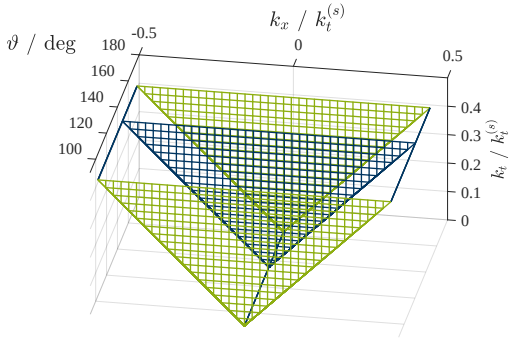

(b) Interpolation in the measurement space

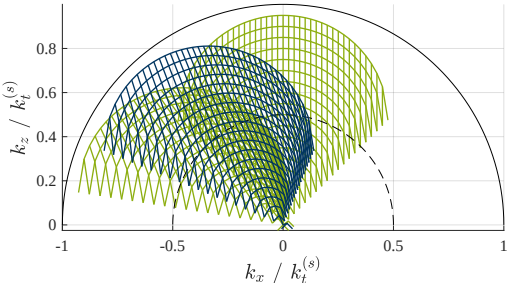

(c) Interpolation in the object space

Figure 6.4.1: Visualization of interpolation approaches; the US measurement data (a) is either interpolated by weighting the data of neighboring angles (b), or by mapping in the object space (c). All axes are scaled by the half temporal sampling wave number $k_t^{(s)}$.

6.4.2 Results using Object Space Interpolation

The object space interpolation was applied to the numerical “clutter”-phantom introduced in section 6.2.2 and section 6.3.2 (see Fig. 6.3.2-a). The results for an increasing number of considered angles are compared to the results with the same amount of angles using measurement space interpolation (see Fig. 6.4.2). For one angle, object space interpolation already returns a significant reduction of the clutter artifact, while measurement space interpolation cannot be applied at all. An artifact ratio was computed for each amount of angles as ratio of the signal powers in a region of interest (ROI) around the leftmost artifact with and without clutter reduction. The artifact ratio is plotted as an artifact reduction curve in Figure. 6.4.2-g. The curve for object space interpolation reaches a saturation level at about 7 angles, where measurement space interpolation does not yet exhibit a significant reduction (see Fig. 6.4.2-c and Fig. 6.4.2-d). At 25 angles, the reduction of measurement space interpolation outperforms object space interpolation. At 91 angles, measurement space interpolation finally reaches a reduction of 9.9 dB compared to 8.6 dB for object space interpolation (see Fig. 6.4.2e and Fig. 6.4.2f). It should be noted that an artifact power ratio of 0 is infeasible due to diffraction and reconstruction artifacts that always appear in the ROI of the artifact.

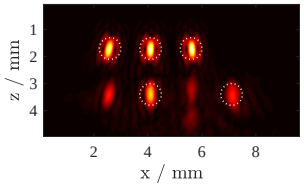

(a) meas. space - 1 angle

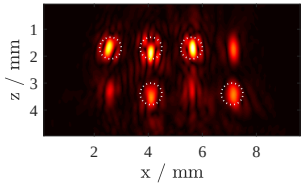

(b) obj. space - 1 angle

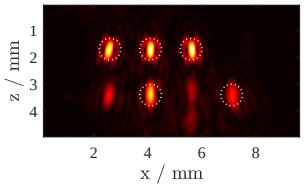

(c) meas. space - 7 angles

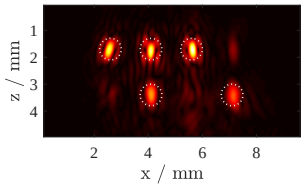

(d) obj. space - 7 angles

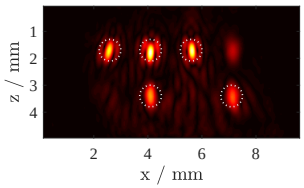

(e) meas. space - 91 angles

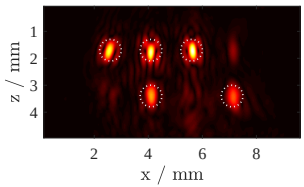

(f) obj. space - 91 angles

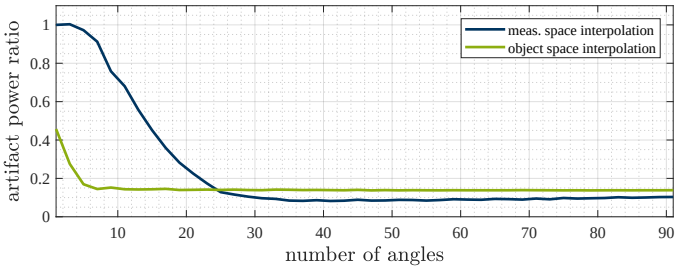

(g)

Figure 6.4.2: Comparison of clutter reduction results with interpolation in object space and measurement space where the angles were always distributed equidistandly: PA image using measurement space interpolation for 1,7 and 91 angles (a,c,e), PA image using object space interpolation for 1,7 and 91 angles (b,d,f), reduction curves for left artifact (g)

6.5 Application to Beamformed US data

Not all combined PA/US imaging systems allow for the acquisition of plane wave US images. However, the clutter reduction that has been introduced in this chapter inevitably requires ultrasound measurement data that has been acquired using plane wave excitations. While dedicated algorithms for other kinds of excitation are conceivable to be developed, an advantage of an algorithm based on plane waves is given by very direct relations in the frequency domain, as a Fourier transform resembles a decomposition of the wavefield into plane waves. Instead of deriving a dedicated algorithm for other US excitation methods, in this section, a general approach to apply the clutter reduction to US image data is introduced, which is independent on how the image data was generated. The only requirement is an access to the raw US image data before envelope detection.

6.5.1 Forward Propagation of US Image Data

A frequency domain relation between the medium heterogeneity $\gamma(\boldsymbol{r})$ and the respective plane wave measurement $p_m^{(us)}$ has already been introduced in section 6.4.1 (see (6.4.1)). Accordingly, for a given US image $\hat{\gamma}(\boldsymbol{r})$ retrieved by an arbitrary reconstruction, an approximation of the plane wave measurement data $\hat{p}_m^{(us)}$ with transmission angle ϑ computes as:

$$\hat{p}_m^{(us)}(k_y, k_t, \vartheta) = \frac{jk_t^2}{2\kappa_z}\hat{\gamma}(k_x + k_x^{(\vartheta)}, \kappa_z + \kappa_z^{(\vartheta)}), \tag{6.5.1}$$

which can be realized as a frequency domain mapping (see Fig. 6.5.1). As being the inverse process of a reconstruction, this mapping can be interpreted as a forward propagation. The resulting scatter model for clutter reduction reads exactly like the one in (6.4.2), with the only difference that $\hat{\gamma}(k_x k_z)$ is not attained by mapping plane wave data onto k-space but by a 2D Fourier transform of the given US image data. Accordingly, $\hat{p}_m^{(us)}(k_y, k_t, \vartheta)$ can be employed for the clutter reduction exactly as $p_m^{(us)}(k_y, k_t, \vartheta)$ has been employed before.

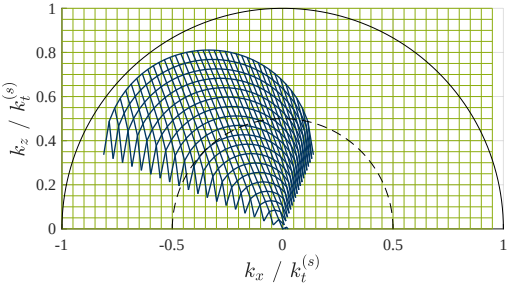

Figure 6.5.1: Visualization of forward propagation from of beamformed data (green grid) to measurement data (blue grid) by interpolation in the image space. All axes are scaled by the temporal sampling wave number $k_t^{(s)}$.

6.5.2 Results Using Beamformed US Data

The clutter reduction algorithm was applied to beamformed US data from an in vivo experiment that was planned and executed by the staff at the European Institute for Molecular Imaging (EIMI) in Münster, Germany. The respective data sets were made available for this dissertation. Like in chapter 5.5.3, photoacoustic and B-mode ultrasound images were acquired using a preclinical ultrasound system (Vevo 2100, Fujifilm VisualSonics Inc., Toronto, Canada) and a tunable (680–970 nm) OPO laser platform (Vevo LAZR, Fujifilm VisualSonics Inc., Toronto, Canada). All settings were according to the description in chapter 5.5.3, except for the ultrasound transducer (LZ-250, Fujifilm VisualSonics Inc., Toronto, Canada, center frequency: 21 MHz). The image in Figure. 6.5.2 shows the heart and the aortic arch of a C57/BL6 mouse as an overlay image with PA data on a gray scale US image, where both images are log-compressed. The dominant clutter artifacts are emphasized by a green circle and are shown to be eliminated in the reconstruction with prior clutter reduction.

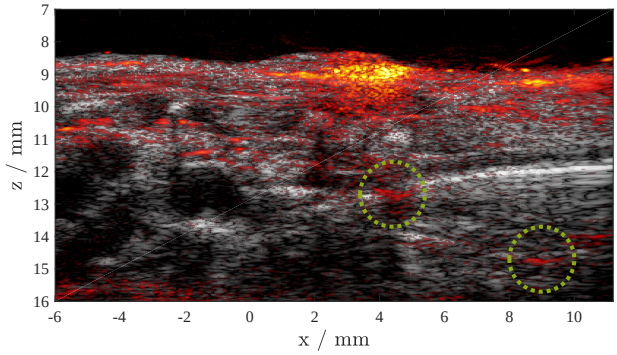

(a)

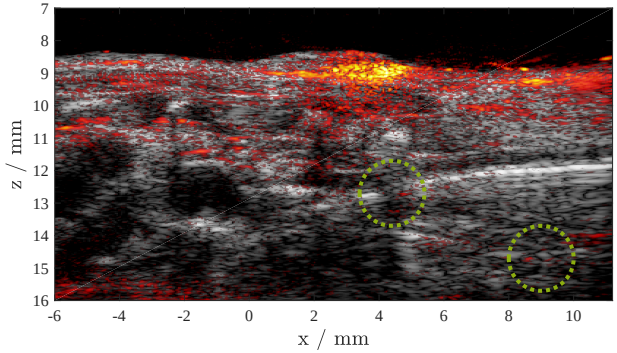

(b)

Figure 6.5.2: In vivo clutter reduction using B-mode US data as overlay image with PA data in red over US data in gray: Overlay image without clutter reduction (a), overlay image with clutter reduction (b), dominant clutter artifacts are indicated by a green circle.

In the visualization of a magnified area around the main source and the two clutter artifacts on a linear color map, the clutter suppression can be evaluated more accurately (see Fig. 6.5.3). Some areas on the lateral edges of the artifacts cannot be sufficiently suppressed. This can be attributed to the lack of lateral information in the B-mode image, which cannot reproduce PA waves being scattered under a steep angle. Some of the other structures might

also be artifacts but cannot be identified because the primary source is not within the field of view.

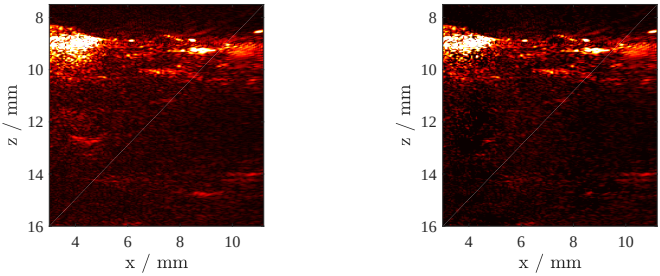

Figure 6.5.3: Magnified PA images showing in vivo clutter reduction based on B-mode US data; PA image without clutter reduction (a), PA image with clutter reduction (b), both images are displayed on a linear intensity map.

6.6 Discussion and Conclusions

In this chapter, a scatter model for PA waves was derived and two different approaches to invert this model were introduced, which allow for the computation of a scatter-free image. The method requires the acquisition of plane wave ultrasound data from various angles in addition to the PA data. The entire computation can be executed on the measurement data and no information about the acoustic properties is required. The model is not restricted to the Born approximation. It requires the primary PA sources, in which the clutter artifacts originate, to be located within the field of view. This can be assured by an illumination beneath the transducer using an acoustic stand-off. However, strongly absorbing structures that are out of view but still illuminated, such as moles, might still cause reflections that cannot be accounted for. A major challenge of the method is the consideration of the impulse response of the ultrasound measurement. As an in-phase modeling of the scattered wave is crucial to the method, neglecting the US impulse response makes an efficient clutter reduction infeasible. For the case that the impulse response can be

accurately modeled or measured, e.g. from the back reflection on a rigid wall, it can be accounted for in the clutter reduction. A filtering scheme was introduced that is meant to invert the US impulse response by simultaneously reducing the amplification of noise without sacrificing too much bandwidth (see section 6.1.1).

One approach for model inversion is based on the truncation of a Neumann series expansion (see section 6.2). Here, a scatter artifact distribution is estimated and subtracted from the actual measurement. While this approach relies on a model simplification, it does not require a numerical inversion and is therefore both robust and computationally efficient. It was shown that the method suppresses clutter artifacts for heterogeneities in both mass density and speed of sound (see Fig. 6.2.2). Also, an actual PA source being colocated with an artifact was not removed. The configuration of a scatterer being placed between PA source and transducer, an additional artifact above the scatterer was introduced by the clutter reduction (see Fig. 6.2.2). This behavior can be explained by scattering of the back propagated PA wave before it reaches the initial pressure distribution. Mathematically speaking, the Green function that was used to formulate the PA wave was a symmetrical Green function in time, even though the PA excitation is really a causal process. Unfortunately, the simplicity of the scatter model in the frequency domain strongly depends on this model deviation. A formulation in the time domain might allow for suppressing scattering during back propagation, but the comfort of the separation of the algorithm into one equation for each temporal frequency would be lost. It should be mentioned that in most cases, the skin is the primary source that generates clutter and hence, these additional artifacts might usually appear outside of the observed tissue. Also, a complete suppression of such artifacts can be easily thought of by a minimum intensity choice between compensated and uncompensated image for each pixel, as a higher value is always an artifact.

A second approach performs a numerical inversion by computing a pseudo-inverse for each temporal frequency to recover non-scattered measurement data (see section 6.3). While the online inversion demands more computational effort than the subtraction approach, it relies on a more exact model. The lack of robustness can be circumvented by the inclusion of Tikhonov regularization. In the investigated scenarios, direct inversion generated comparable results to the subtraction method, even though the achievable suppression was usually not as strong (see Fig. 6.3.2).

In both methods, a large set of US measurements is required to ensure an efficient clutter reduction. Data from missing angles can be interpolated by linear interpolation between neighboring angles. Still, an angle spacing of

about 1° is suggested, which, for an interval between ±50° already requires 91 measurements, all of which have to be acquired, transferred and processed. To reduce the amount of required angles, an alternative interpolation method was introduced that is based on linear US diffraction tomography and interpolates missing data by mapping it onto a grid representing the US object data. This interpolation relies on the Born approximation, which means that multiple scattering is not correctly accounted for in the interpolation. Comparing the two interpolation approaches, this object space interpolation generated significantly better suppression for a small number of angles. Once the number of acquired angles increased, measurement space interpolation could outperform object space interpolation (see Fig. 6.4.2).

A principle draw back of the clutter reduction method is the restriction to plane wave ultrasound data, which is not available on all PAUS systems. Therefore, an adjusted method was introduced that derives the scattering information from any high frequent US image data, regardless of how the image was obtained (see section 6.5.2). Certainly, this implies that multiple scattering cannot be considered any more. Also, many aspects of the clutter reduction are harder to control. However, it was shown that an effective clutter reduction could be performed in vivo based on B-mode ultrasound data (sse Fig. 6.5.2). Since the US impulse response could not be accurately modeled the clutter reduction relied on a subtraction of envelope data. Still, this example promises a wide rage of applicability of the algorithm.

7 Summary

In photoacoustic imaging, the waves originating in pulsed laser light absorption are scattered at heterogeneities in the acoustic medium properties. This effect is usually not considered in the image reconstruction, as simple algorithms can be derived when assuming the travel distance of a wave to be a multiple of the travel time with a constant factor. However, the assumption can cause artifacts that blur the image or generate false structures covering the image. In the frame of this dissertation, three methods were introduced that address the suppression of artifacts associated with scattering of photoacoustic waves in linear array measurements. The work is motivated by photoacoustic imaging of the carotid artery, which is considered a promising tool in the characterization of atherosclerotic plaques.

The first proposed approach is a Landweber iteration based reconstruction method that relies on a pair of a forward operator and an adjoint operator that are computed using pseudo-spectral methods. Successive computation and updating the PA source term lead to converging algorithm that accounts for medium heterogeneities when they are known. It was shown that the Landweber iteration can improve the resolution in scattering media significantly. It also performs a very accurate compensation for the imaging system's temporal impulse response that is determined by the laser pulse shape and the acousto-electric impulse response. Pieces of information that are lost due to the limited view were recovered due to the consideration of back reflection, which simultaneously reduced reflection artifacts. In the frame of simulation

data, it was also shown that a reconstruction without a priori knowledge yields good results, if the heterogeneities are estimated by a nonlinear reflection mode ultrasound reconstruction. The convergence of the method, however, is very sensitive to the accuracy of the underlying heterogeneity map. Also, for currently available computing performances, the effort of two wave simulations per iteration with several thousand iterations required is too high to be a suitable solution in a clinical context, or even in real-time. For that reason the problem of scattering of the photoacoustic wave was separated into reflections and refraction and two less model based but efficient algorithms were introduced to address the respective issues.

A back propagation algorithm that is based on a paraxial wave propagation model was proposed. The algorithm is referred to as paraxial back propagation and uses a Fourier split step approach to account for both diffraction and refraction in two successive steps during the back propagation. The method recovers the source distribution very accurately, even in strongly scattering media, where a standard reconstruction distorts the photoacoustic sources. Compared to other approaches that consider speed-of-sound variations during the back propagation, such as time reversal, the new method could be implemented much faster with comparably good results. A realistic model showed that the impact of aberrations in carotid-artery imaging is expected to be minor but the image quality could still be improved using paraxial back propagation. The method was shown to be robust in terms of inaccurate information about the speed of sound and could even improve the resolution using a fairly inaccurate speed-of-sound reconstruction or a speed-of-sound map derived from segmentation.

Besides the reconstruction method that accounts for refraction, a method that addresses reflection artifacts, also referred to as clutter artifacts, was introduced. The clutter reduction approach relies on the inversion of a scatter model, where a scatter-free measurement can be computed using the information of plane wave ultrasound measurements in reflection mode from various transmission angles. Two approaches were shown for model inversion, both of which could significantly reduce clutter artifacts for both mass density scatters and speed-of-sound scatters, while actual sources obscured by clutter artifacts were not eliminated. Additionally introduced artifacts in the clutter reduction are likely to appear mostly outside the important image regions and might be suppressed in the future by a straight-forward minimum-value computation between compensated and uncompensated image. The number of required acquisitions can be reduced using an interpolation method in the object space of the scatterers, which, for a small number of angles, provides much better

results than linear interpolation in the space of measurements. The approach was also shown to be able to reduce artifacts based on B-mode ultrasound data by using a frequency-domain mapping law based on linear diffraction theory.

In summary, it might be stated that artifacts resulting from scattering of the photoacoustic wave can be compensated for by computationally efficient model based reconstruction and that this scattering can be exploited to improve the image quality. However, for this, exact heterogeneity data is required and the computational effort is huge. Addressing aberrations and clutter in two consecutive methods, a temporally efficient artifact reduction can be attained that is only based on additionally acquired plane wave ultrasound data. As both aberrations and clutter reduce the imaging depth, the implementation of these algorithms might significantly contribute to the feasibility of real-time photoacoustic imaging of the carotid artery.

Bibliography

[1] Toshitaka Agano and Naoto Sato. Photoacoustic Imaging System using LED light source. In *Lasers and Electro-Optics (CLEO)*, pages 1–2. IEEE, 2016.

[2] Toshitaka Agano, Naoto Sato, Hitoshi Nakatsuka, Kazuo Kitagawa, Takamitsu Hanaoka, Koji Morisono, Yusuke Shigeta, and Chizuyo Tanaka. Photoacoustic imaging of clinical metal needle by a LED light source integrated transducer. In *Proc. SPIE*, volume 9708, page 97083U, 2016.

[3] Thomas J. Allen and Paul C. Beard. Light emitting diodes as an excitation source for biomedical photoacoustics. *Proc. SPIE 8581*, 8581(3):85811F, 2013.

[4] Thomas J Allen and Paul C Beard. High power visible light emitting diodes as pulsed excitation sources for biomedical photoacoustics. *Biomed. Opt. Express*, 7(4):1260–1270, apr 2016.

[5] Thomas J Allen, Andrew Hall, Amar P Dhillon, James S Owen, and Paul C Beard. Spectroscopic photoacoustic imaging of lipid-rich plaques in the human aorta in the 740 to 1400 nm wavelength range. *J. Biomed. Opt.*, 17(6):1–10, 2012.

[6] Erwin J Alles, Richard J Colchester, and Adrien E Desjardins. Adaptive Light Modulation for Improved Resolution and Efficiency in All-Optical Pulse-Echo Ultrasound. *IEEE Trans. Ultrason. Ferroelectr. Freq. Control*, 63(1):83–90, 2016.

[7] Erwin J Alles, Michael Jaeger, and Jeffrey C Bamber. Photoacoustic Clutter Reduction Using Short-Lag Spatial Coherence Weighted Imaging. In *2014 IEEE Int. Ultrason. Symp.*, pages 41–44, 2014.

[8] Derek Allman, Austin Reiter, and Muyinatu A Lediju Bell. A Machine Learning Method to Identify and Remove Reflection Artifacts in Photoacoustic Channel Data. In *IEEE Int. Ultrason. Symp.*, pages 0–3, 2017.

[9] Lea Althaus. *On acoustic tomography using paraxial approximations*. Master's thesis, TU Darmstadt, 2016.

[10] Mark Anastasio and Kun Wang. Advanced image reconstruction for ultrasound-photoacoustic computed tomography. *SPIE Newsroom*, pages 1–3, 2015.

[11] Mark A Anastasio, Jin Zhang, Xiaochuan Pan, Yu Zou, Geng Ku, and Lihong V Wang. Half-Time Image Reconstruction in Thermoacoustic Tomography. 24(2):199–210, 2005.

[12] M U Arabul, H M Heres, M C M Rutten, and M R H M Van Sambeek. Ex vivo photoacoustic imaging of atherosclerotic carotid plaques. In *IEEE Int. Ultrason. Symp. Proc.*, pages 3–6, 2015.

[13] Haim Azhari. *Basics of Biomedical Ultrasound for Engineers*. John Wiley & Sons, 2010.

[14] B. E. Treeby and B. T. Cox. k-Wave: MATLAB toolbox for the simulation and reconstruction of photoacoustic wave-fields. *Biomed. Opt.*, 15(2):021314, 2010.

[15] Natalie Baddour. A multi-dimensional transfer function approach to photo-acoustic signal analysis. *J. Franklin Inst.*, 345(7):792–818, oct 2008.

[16] Natalie Baddour. Theory and analysis of frequency-domain photoacoustic tomography. *J. Acoust. Soc. Am.*, 123(5):2577–90, may 2008.

[17] Alex H Barnett. Greens Functions for the Wave Equation, available: https://math.dartmouth.edu/˜ahb/notes/waveequation.pdf, date acessed: 2017-10-25, 2006.

[18] Alexey N Bashkatov, Elina A Genina, and Valery V Tuchin. Optical Properties of Skin , Subcutaneous, and Muscle Tissues: a Review. *J. Innov. Opt. Health Sci.*, 4(1):9–38, 2011.

[19] Paul C. Beard. Biomedical Photoacoustic Imaging: a review. *Interface Focus*, (May 2011):602–631, 2011.

[20] Martin F. Beckmann. *Optimizing a semiconductor laser based photoacoustic imaging system*. PhD thesis, Ruhr-Universität Bochum, 2016.

[21] Martin F. Beckmann, Georg Schmitz, and Hans Martin Schwab. Multispectral photoacoustic coded excitation with low PRF high power laser diodes. In *IEEE Int. Ultrason. Symp. IUS*, pages 1288–1291, 2014.

[22] Martin F. Beckmann, Hans-Martin Schwab, and Georg Schmitz. Optimized SNR simultaneous multispectral photoacoustic imaging with laser diodes. *Opt. Express*, 23(2):1816, 2015.

[23] Martin F Beckmann, Hans-Martin Schwab, and Georg Schmitz. Optimizing a Single-Sided Reflection Mode Photoacoustic Setup for Clinical Imaging. In *2015 IEEE Int. Ultrason. Symp. Proc.*, 2015.

[24] Martin F Beckmann, Hans-Martin Schwab, and Georg Schmitz. Optimizing Simultaneous Multispectral Emission Photoacoustics. In *2015 IEEE Int. Ultrason. Symp. Proc.*, number 318067, 2015.

[25] Alexander Graham Bell. *Upon the production of sound by radiant energy*. Washington, Gibson Brothers, printers, 1881.

[26] Jean-Pierre Berenger. A perfectly matched layer for the absorption of electromagnetic waves. *J. Comput. Phys.*, 114:185–200, 1994.

[27] Jonathan Blackledge. *Electromagnetic Scattering Solutions for Digital Signal Processing Jonathan Blackledge Electromagnetic Scattering Solutions for Digital Signal Processing*. PhD thesis, University of Jyväskylä, 2010.

[28] S Boonsang, J Zainal, and R J Dewhurst. Photoacoustic imaging using a frequency domain synthetic aperture focusing technique. In *Int. Conf. Adv. Laser Technol. Biomed. Opt.*, volume 5486, pages 267–273, 2004.

[29] A. Buehler, X. L. Deán-Ben, J. Claussen, V. Ntziachristos, and D. Razansky. Three-dimensional optoacoustic tomography at video rate. *Opt. Express*, 20(20):22712, 2012.

[30] Andreas Buehler, Marcin Kacprowicz, Adrian Taruttis, and Vasilis Ntziachristos. Real-time handheld multispectral optoacoustic imaging. *Opt. Lett.*, 38(9):1404–1406, 2013.

[31] Bing Cong, Kengo Kondo, Takeshi Namita, Makoto Yamakawa, and Tsuyoshi Shiina. Photoacoustic image quality enhancement by estimating mean sound speed based on optimum focusing. *Jpn. J. Appl. Phys.*, 54(7S1):07HC13, 2015.

[32] James W. Cooley and John W Tukey. An Algorithm for the Machine Calculation of Complex Fourier Series. *Math. Comput.*, 19(90):297–301, 1965.

[33] B. T. Cox and P. C. Beard. Fast calculation of pulsed photoacoustic fields in fluids using k-space methods. *J. Acoust. Soc. Am.*, 117(6):3616–3627, 2005.

[34] B. T. Cox, S. Kara, S. R. Arridge, and P. C. Beard. k-space propagation models for acoustically heterogeneous media: Application to biomedical photoacoustics. *J. Acoust. Soc. Am.*, 121(6):3453, 2007.

[35] Benjamin T Cox and Bradley E Treeby. Artifact Trapping During Time Reversal Photoacoustic Imaging for Acoustically Heterogeneous Media. *IEEE Trans. Med. Imaging*, 29(2):387–396, 2010.

[36] K Daoudi, P J Van Den Berg, O Rabot, A Kohl, S Tisserand, P Brands, and W Steenbergen. Handheld probe integrating laser diode and ultrasound transducer array for ultrasound / photoacoustic dual modality imaging. *Opt. Express*, 22(21):436–440, 2014.

[37] Khalid Daoudi, Pim van den Berg, Olivier Rabot, Andreas Kohl, Stephane Tisserand, Peter Brands, and Wiendelt Steenbergen. Handheld probe combining laser diode and ultrasound transducer array for ultrasound/photoacoustic dual modality imaging. In *SPIE Photonics West*, page 7, 2014.

[38] M J Davies, P D Richardson, N Woolf, D R Katz, and J Mann. Risk of thrombosis in human atherosclerotic plaques: role of extracellular lipid,

macrophage, and smooth muscle cell content. *Br. Heart J.*, 69(5):377–81, may 1993.

[39] Adam de la Zerda, Yannis M Paulus, Robert Teed, Sunil Bodapati, Yosh Dollberg, Butrus T Khuri-Yakub, Mark S Blumenkranz, Darius M Moshfeghi, and Sanjiv Sam. Photoacoustic ocular imaging. *Opt. Lett.*, 35(3):270–272, 2010.

[40] X Luís Deán-Ben, Rui Ma, Daniel Razansky, and Vasilis Ntziachristos. Statistical approach for optoacoustic image reconstruction in the presence of strong acoustic heterogeneities. *IEEE Trans. Med. Imaging*, 30(2):401–408, 2011.

[41] X Luís Deán-Ben, Rui Ma, Amir Rosenthal, Vasilis Ntziachristos, and Daniel Razansky. Weighted model-based optoacoustic reconstruction in acoustic scattering media. *Phys. Med. Biol.*, 58:5555–5566, 2013.

[42] X Luís Deán-Ben, Vasilis Ntziachristos, and Daniel Razansky. Statistical optoacoustic image reconstruction using a-priori knowledge on the location of acoustic distortions. *Appl. Phys. Lett.*, 98(17), 2011.

[43] X Luís Deán-Ben, Vasilis Ntziachristos, and Daniel Razansky. Acceleration of optoacoustic model-based reconstruction using angular image discretization. *IEEE Trans. Med. Imaging*, 31(5):1154–1162, 2012.

[44] X Luís Deán-Ben, Vasilis Ntziachristos, and Daniel Razansky. Effects of small variations of speed of sound in optoacoustic tomographic imaging. *Med. Phys.*, 41(7):1–12, 2014.

[45] X Luís Deán-Ben, Vasilis Ntziachristos, Daniel Razansky, and Vasilis Ntziachristos. Artefact reduction in optoacoustic tomographic imaging by estimating the distribution of acoustic scatterers. *J. Biomed. Opt.*, 17(11):110504, 2012.

[46] Xosé Luís Deán-Ben and Daniel Razansky. Functional optoacoustic human angiography with handheld video rate three dimensional scanner. *Photoacoustics*, 1(3-4):68–73, 2013.

[47] Wouter J M Derksen, Jean Paul P M De Vries, Aryan Vink, Evelyn Velema, Jan Albert Vos, Dominique De Kleijn, Frans L. Moll, and Gerard Pasterkamp. Histologic atherosclerotic plaque characteristics are associated with restenosis rates after endarterectomy of the common and superficial femoral arteries. *J. Vasc. Surg.*, 52(3):592–599, 2010.

[48] A.J. Devaney. A Filtered Backpropagation Algorithm for Diffraction Tomography. *Ultrason. Imaging*, 4:336–350, 1982.

[49] A.J. Devaney. *Mathematical Foundations of Imaging, Tomography and Wavefield Inversion*. Cambridge University Press, 2012.

[50] Alexander Dima and Vasilis Ntziachristos. Non-invasive carotid imaging using optoacoustic tomography. *Opt. Express*, 20(22):25044–25057, 2012.

[51] A. Dutt and V. Rokhlin. Fast Fourier Transforms for Nonequispaced Data. *SIAM J. Sci. Comput.*, 14(6):1368–1393, nov 1993.

[52] Sergey A Ermilov, Tuenchit Khamapirad, Andre Conjusteau, Morton H Leonard, Ron Lacewell, Ketan Mehta, Tom Miller, and Alexander A Oraevsky. Laser optoacoustic imaging system for detection of breast cancer. *J. Biomed. Opt.*, 14(2):24007–24014, 2009.

[53] Ying Fan, Andreas Mandelis, Gloria Spirou, and I Alex Vitkin. Development of a laser photothermoacoustic frequency-swept system for subsurface imaging: theory and experiment. *J. Acoust. Soc. Am.*, 116(6):3523–3533, 2004.

[54] M D Feit and J A Fleck. Light propagation in graded-index optical fibers. *Appl. Opt.*, 17(24):3990–3998, 1978.

[55] Mathias Fink and Claire Prada. Acoustic time-reversal mirrors. *Inverse Probl.*, 17(1):R1–R38, 2001.

[56] Steven J. Ford, Paul L. Bigliardi, Thomas C.P. Sardella, Alexander Urich, Neal C. Burton, Marcin Kacprowicz, Mei Bigliardi, Malini Olivo, and Daniel Razansky. Structural and Functional Analysis of IntactÂ Hair Follicles and Pilosebaceous Units by Volumetric Multispectral Optoacoustic Tomography. *J. Invest. Dermatol.*, 136(4):753–761, 2016.

[57] Martin Frenz and Michael Jaeger. Optimization of tissue irradiation in optoacoustic imaging using a linear transducer: theory and experiments. In *Photons Plus Ultrasound Imaging Sens.*, volume 6856, page 68561Y, 2008.

[58] Claus-Stefan Friedrich. *Photoakustik mit Halbleiterlasern*. PhD thesis, Ruhr Universität Bochum, 2011.

[59] Claus-Stefan Friedrich, Martin P Mienkina, Carsten Brenner, Nils C Gerhardt, Manfred Jörger, Andreas Strauß, Martin F Beckmann, Georg Schmitz, and Martin R Hofmann. Photoacoustic Blood Oxygenation Imaging Based on Semiconductor Lasers. *Photonics Optoelectron.*, 1(3):48–54, 2012.

[60] Matthew P Fronheiser, Sergey A Ermilov, Hans-Peter Brecht, Andre Conjusteau, Richard Su, Ketan Mehta, and Alexander A Oraevsky. Real-time optoacoustic monitoring and three-dimensional mapping of a human arm vasculature. *J. Biomed. Opt.*, 15(2):021305, 2010.

[61] Ekaterina I. Galanzha, Evgeny V. Shashkov, Thomas Kelly, Jin-Woo Kim, Lily Yang, and Vladimir P. Zharov. In vivo magnetic enrichment and multiplex photoacoustic detection of circulating tumour cells. *Nat. Nanotechnol.*, 4(12):855–860, 2009.

[62] John Gamelin, Anastasios Maurudis, Andres Aguirre, Fei Huang, Puyun Guo, Lihong, V. Wang, and Quing Zhu. A real-time photoacoustic tomography system for small animals. *Opt. Express*, 19(6):431–444, 2014.

[63] Hartmut Gemmeke. Wave Equation based Transmission Tomography for USCT. Technical report, Karlsruhe Institute of Technology, 2017.

[64] Hartmut Gemmeke, Lea Althaus, Koen W A Van Dongen, Herbert Egger, Jürgen Hesser, Jana Mayer, Nicole V Ruiter, Michael Zapf, and Torsten Hopp. Wave Equation Based Transmission Tomography. In *IEEE Int. Ultrason. Symp. Proc.*, pages 1309–1–4, 2016.

[65] Christopher K Glass and Joseph L Witztum. Atherosclerosis: The Road Ahead. *Cell*, 104:503–516, 2001.

[66] Sven Gottschalk, Thomas Felix Fehm, Xosé Luís Deán-Ben, and Daniel Razansky. Noninvasive Real-Time Visualization of Multiple Cerebral Hemodynamic Parameters in Whole Mouse Brains Using Five-Dimensional Optoacoustic Tomography. *J. Cereb. Blood Flow Metab.*, 35(4):531–535, 2015.

[67] T Grau and R Breitkreutz. *Ultraschall in der Anästhesie und Intensivmedizin: Lehrbuch der Ultraschalldiagnostik*. Dt. Ärzte-Verlag, 2009.

[68] Raffaele Grella. Fresnel Propagation and Diffraction and Paraxial Wave Equation. *J. Opt.*, 13(6):367–374, 1982.

[69] H. F. Trotter. On the Product of Semi-Groups of Operators. In *Proc. Am. Math. Soc.*, volume 10, pages 545–551. American Mathematical Society, 1959.

[70] Christoph Haisch, Karin Eilert-Zell, Mika M Vogel, Peter Menzenbach, and Reinhard Niessner. Combined optoacoustic/ultrasound system for tomographic absorption measurements: possibilities and limitations. *Anal. Bioanal. Chem.*, 397(4):1503–1510, jun 2010.

[71] Markus Haltmeier, Otmar Scherzer, and Gerhard Zangerl. A reconstruction algorithm for photoacoustic imaging based on the nonuniform FFT. *IEEE Trans. Med. Imaging*, 28(11):1727–1735, 2009.

[72] Michelle Heijblom, Wiendelt Steenbergen, and Srirang Manohar. Clinical photoacoustic breast imaging: The twente experience. *IEEE Pulse*, 6(3):42–46, 2015.

[73] Gerrit Held, Stefan Preisser, Sara Peeters, Michael Jaeger, and Martin Frenz. Effect of irradiation distance on image contrast in epi-optoacoustic imaging of human volunteers. *Biomed. Opt. Express*, 5(11):3765–3780, 2014.

[74] Markus C Hesse. *Nichtlineare quantitative Rekonstruktion akustischer Materialparameter in der niederfrequenten 2D/3D Ultraschall-Reflexionstomographie*. Shaker Verlag GmbH, Bochum, 2015.

[75] Markus C Hesse, Leili Salehi, and Georg Schmitz. Nonlinear simultaneous reconstruction of inhomogeneous compressibility and mass density distributions in unidirectional pulse-echo ultrasound imaging. *Phys. Med. Biol.*, 58(17):6163–6178, sep 2013.

[76] Yulia Hristova, Peter Kuchment, and Linh Nguyen. Reconstruction and time reversal in thermoacoustic tomography in acoustically homogeneous and inhomogeneous media. *Inverse Probl.*, 24(5):055006, oct 2008.

[77] Chao Huang. *Image Reconstruction in Photoacoustic Computed Tomography with Acoustically Heterogeneous Media*. PhD thesis, Washington University in St. Louis, 2014.

[78] Chao Huang, Robert W Schoonover, Carsten O Schirra, Mark A Anastasio, and Lihong V Wang. Aberration correction for transcranial photoacoustic tomography of primates employing adjunct image data. *J. Biomed. Opt.*, 17(6):0660161 – 0660167, 2012.

[79] Chao Huang, Kun Wang, Liming Nie, Lihong V Wang, and Mark A Anastasio. Full-Wave Iterative Image Reconstruction in Photoacoustic Tomography with Acoustically Inhomogeneous Media. *IEEE Trans. Med. Imaging*, 32(6):1097–1110, 2013.

[80] Chao Huang, Kun Wang, Robert W. Schoonover, Lihong V. Wang, and Mark A. Anastasio. Joint Reconstruction of Absorbed Optical Energy Density and Sound Speed Distribution in Photoacoustic Computed Tomography: A numerical Investigation. *IEEE Trans. Comput. Imaging*, 2(2):1–13, 2015.

[81] Lianjie Huang, Kenneth M Hanson, Youli Quan, Cuiping Li, Neb Duric, and Los Alamos. Globally optimized Fourier finite-difference method for ultrasound breast imaging. In *Med. Imaging 2008 Ultrason. Imaging Signal Process.*, volume 6920, pages 1–11, 2008.

[82] Lianjie Huang and Youli Quan. Ultrasound pulse-echo imaging using the split-step Fourier propagator. In *Med. Imaging 2007 Ultrason. Imaging Signal Process.*, volume 6513, pages 1–12, 2007.

[83] Q Huang and Z Zeng. A Review on Real-Time 3D Ultrasound Imaging Technology. *Biomed Res Int*, 2017:6027029, 2017.

[84] Steven L Jacques. Optical properties of biological tissues: a review. *Phys. Med. Biol.*, 58(11):R37–61, 2013.

[85] Michael Jaeger, Jeffrey C. Bamber, and Martin Frenz. Clutter elimination for deep clinical optoacoustic imaging using localised vibration tagging (LOVIT). *Photoacoustics*, 1:19–29, 2013.

[86] Michael Jaeger, David Harris-Birtill, Andreas Gertsch, Elizabeth O'Flynn, and Jeffrey Bamber. Deformation-compensated averaging for clutter reduction in epiphotoacoutic imaging in vivo. *J. Biomed. Opt.*, 17(6):066007, 2012.

[87] Michael Jaeger, Gerrit Held, Sara Peeters, Stefan Preisser, Michael Grünig, and Martin Frenz. Computed Ultrasound Tomography in Echo

Mode for Imaging Speed of Sound Using Pulse-Echo Sonography: Proof of Principle. *Ultrasound Med. Biol.*, pages 1–16, sep 2014.

[88] Michael Jaeger, Simon Schüpbach, Andreas Gertsch, Michael Kitz, and Martin Frenz. Fourier reconstruction in optoacoustic imaging using truncated regularized inverse k -space interpolation. *Inverse Probl.*, 23(6):51–63, dec 2007.

[89] Michael Jaeger, Lea Siegenthaler, Michael Kitz, and Martin Frenz. Reduction of background in optoacoustic image sequences obtained under tissue deformation. *J. Biomed. Opt.*, 14(5):054011, 2009.

[90] Krista Jansen, Antonius F W van der Steen, Heleen M M van Beusekom, J Wolter Oosterhuis, and Gijs van Soest. Intravascular photoacoustic imaging of human coronary atherosclerosis. *Opt. Lett.*, 36(5):597–599, 2011.

[91] Krista Jansen, Gijs van Soest, and Antonius F.W. van der Steen. Intravascular Photoacoustic Imaging: A New Tool for Vulnerable Plaque Identification. *Ultrasound Med. Biol.*, 40(6):1037–1048, jun 2014.

[92] Huabei Jiang. *Photoacoustic Tomography*. Taylor & Francis Group, 2015.

[93] Xing Jin and Lihong V Wang. Thermoacoustic tomography with correction for acoustic speed variations. *Phys. Med. Biol.*, 51(24):6437–6448, 2006.

[94] Jithin Jose, Rene G H Willemink, Wiendelt Steenbergen, C H Slump, Ton G van Leeuwen, and Srirang Manohar. Speed-of-sound compensated photoacoustic tomography for accurate imaging. *Med. Phys.*, 39(12):7262–71, dec 2012.

[95] Seyed Ebrahim Kassaian and Hamidreza Goodarzynejad. Carotid artery stenting, endarterectomy, or medical treatment alone: The debate is not over. *J. Tehran Univ. Hear. Cent.*, 6(1):1–13, 2011.

[96] Chulhong Kim, Todd N Erpelding, Ladislav Jankovic, Michael D Pashley, and Lihong V Wang. Deeply penetrating in vivo photoacoustic imaging using a clinical ultrasound array system. *Biomed. Opt. Express*, 1(1):278–284, 2010.

[97] Fritz K. Kneubühl and Markus Werner Sigrist. *Laser*. B. G. Teubner Stuttgart, 2 edition, 1989.

[98] Roy G Kolkman, Wiendelt Steenbergen, and Ton G Van Leeuwen. Reflection mode photoacoustic measurement of speed of sound. *Opt. Express*, 15(6):3291–3300, 2007.

[99] Roy G M Kolkman, Peter J Brands, Wiendelt Steenbergen, and Ton G van Leeuwen. Real-time photoacoustic and ultrasound imaging of human vasculature. In *Proc. Photons Plus Ultrasound*, volume 7177, pages 717704–717705, 2009.

[100] Roy G M Kolkman, Wiendelt Steenbergen, and Ton G van Leeuwen. In vivo photoacoustic imaging of blood vessels with a pulsed laser diode. *Lasers Med. Sci.*, 21(3):134–139, sep 2006.

[101] Kornel P. Köstli and Paul C. Beard. Two-Dimensional Photoacoustic Imaging by Use of Fourier-Transform Image Reconstruction and a Detector with an Anisotropic Response. *Appl. Opt.*, 42(10):1899–1908, 2003.

[102] Kornel P Köstli, Martin Frenz, Hans Bebie, and Heinz P. Weber. Temporal backward projection of optoacoustic pressure transients using Fourier transform methods. *Phys. Med. Biol.*, 46:1863–1872, 2001.

[103] R. A. Kruger. Photoacoustic ultrasound. *Med. Phys.*, 21:127–131, 1994.

[104] Pieter Kruizinga, Antonius F. W. van der Steen, Nico de Jong, Geert Springeling, Jan Lukas Robertus, Aad van der Lugt, and Gijs van Soest. Photoacoustic imaging of carotid artery atherosclerosis. *J. Biomed. Opt.*, 19(11):110504, 2014.

[105] L. Landweber. An Iteration Formula for Fredholm Integral Equations of the First Kind. *Am. J. Math.*, 73(3):615–624, 1951.

[106] Gerrit Cornelis Langhout, Diederik Johannes Grootendorst, Omgo Edo Nieweg, Michel Wilhelmus, Jacobus Maria, Jos Alexander Van Der Hage, Jithin Jose, Hester Van Boven, Wiendelt Steenbergen, Srirang Manohar, Theodoor Jacques, and Marie Ruers. Detection of Melanoma Metastases in Resected Human Lymph Nodes by Noninvasive Multispectral Photoacoustic Imaging. *Int. J. Biomed. Imaging*, 2014(163652):1–7, 2014.

[107] Jan Laufer, Clare Elwell, Dave Delpy, and Paul Beard. Quantitative spatially resolved measurement of tissue chromophore concentrations

using photoacoustic spectroscopy : application to the measurement of blood oxygenation and haemoglobin concentration. *Phys. Med. Biol.*, 52:141–168, 2007.

[108] Muyinatu A. Lediju Bell, Nathanael Kuo, Danny Y. Song, and Emad M. Boctor. Short-lag spatial coherence beamforming of photoacoustic images for enhanced visualization of prostate brachytherapy seeds. *Biomed. Opt. Express*, 4(10):1964, 2013.

[109] R T Lee and P Libby. The unstable atheroma. *Arterioscler. Thromb. Vasc. Biol.*, 17(10):1859–67, oct 1997.

[110] Changhui Li and Lihong V. Wang. Photoacoustic tomography and sensing in biomedicine. *Phys. Med. Biol.*, 54(19):1–52, 2009.

[111] Xu Li, Jiali Yang, Mingyue Ding, and Ming Yuchi. Preliminary work of real-time ultrasound imaging system for 2-D array transducer. *Biomed. Mater. Eng.*, 26:S1579–S1585, 2015.

[112] Lun-de Liao, Chin-teng Lin, Yen-yu I Shih, Timothy Q Duong, Hsin-yi Lai, Po-hsun Wang, Robby Wu, Siny Tsang, Jyh-yeong Chang, Meng-lin Li, and You-yin Chen. Transcranial imaging of functional cerebral hemodynamic changes in single blood vessels using in vivo photoacoustic microscopy. *J. Cereb. Blood Flow & Metab.*, 32(6):938–951, 2012.

[113] Wenzhong Liu and Hao F Zhang. Photoacoustics Photoacoustic imaging of the eye: A mini review. *Photoacoustics*, 4(3):112–123, 2016.

[114] Alfred Karl Louis. *Inverse und schlecht gestellte Probleme*. Vieweg+Teubner Verlag, 1989.

[115] Jian-yu Lu. Experimental Study of High Frame Rate Imaging with Limited Diffraction Beams. *IEEE Trans. Ultrason. Ferroelectr. Freq. Control*, 45(1):84–97, 1998.

[116] Aj Lusis. Atherosclerosis. *Nature*, 407(6801):233–241, 2000.

[117] Christian Lutzweiler, Reinhard Meier, Ernst Rummeny, Vasilis Ntziachristos, and Daniel Razansky. Real-time optoacoustic tomography of indocyanine green perfusion and oxygenation parameters in human finger vasculature. *Opt. Lett.*, 39(14):4061–4064, jul 2014.

[118] Friedrich M. Mahl. *Digitale Bildsignalverarbeitung*. Springer Verlag, 1989.

[119] Srirang Manohar and Daniel Razansky. Photoacoustics: a historical review. *Adv. Opt. Photonics*, 8(4):586–617, 2016.

[120] Gary F. Margrave and Robert J. Ferguson. Wavefield extrapolation by nonstationary phase shift. *Geophysics*, 64(4):1067, 1999.

[121] T D Mast, L P Souriau, D L D Liu, M Tabei, a I Nachman, and R C Waag. A k-space method for large-scale models of wave propagation in tissue. *IEEE Trans. Ultrason. Ferroelectr. Freq. Control*, 48(2):341–354, 2001.

[122] Thomas P Matthews and Mark A Anastasio. Joint Reconstruction of the Sound Speed and Initial Pressure Distributions for Ultrasound Computed Tomography and Photoacoustic Computed Tomography. In *Med. Imaging 2017 Ultrason. Imaging Tomogr.*, volume 10139, pages 1–7, 2017.

[123] Mohammad Mehrmohammadi, Soon Joon Yoon, Douglas Yeager, Stanislav Y., and Emelianov. Photoacoustic Imaging for Cancer Detection and Staging. *Curr. Mol. Imaging*, 2(1):89–105, 2013.

[124] Jan Menke. Photoacoustic breast tomography prototypes with reported human applications. *Eur. Radiol.*, 25(8):2205–2213, aug 2015.

[125] Martin P Mienkina. *Kodierte Anregung in der photoakustischen Bildgebung*. PhD thesis, Ruhr-Universität Bochum, 2010.

[126] P Mojabi and J LoVetri. Overview and Classification of Some Regularization Techniques for the Gauss-Newton Inversion Method Applied to Inverse Scattering Problems. *IEEE Trans. Antennas Propag.*, 57(9):2658–2665, 2009.

[127] Leonardo G Montilla, Ragnar Olafsson, Daniel R Bauer, and Russell S Witte. Real-time photoacoustic and ultrasound imaging: a simple solution for clinical ultrasound systems with linear arrays. *Phys. Med. Biol.*, 58(1):N1–12, 2013.

[128] Karen S Moulton, Eric Heller, Moritz A Konerding, Evelyn Flynn, Wulf Palinski, and Judah Folkman. Angiogenesis Inhibitors Endostatin or TNP-470 Reduce Intimal Neovascularization and Plaque Growth in Apolipoprotein E-Deficient Mice. *Circulation*, 99(13):1726–1732, 1999.

[129] F Natterer. Ultrasound Tomography With Fixed Linear Arrays of Transducers. In *Proc. Interdiscip. Work. Math. Methods Biomed. Imaging Intensity-Modulated Radiat. Ther.*, pages 1–16, 2006.

[130] Frank Natterer. Numerical Solution of Bilinear Inverse Problems. Technical report, Westfälische Wilhelms-Universität, 1995.

[131] Andrew Needles, Andrew Heinmiller, John Sun, Catherine Theodoropoulos, David Bates, Desmond Hirson, Melissa Yin, and F. Foster. Development and initial application of a fully integrated photoacoustic micro-ultrasound system. *IEEE Trans. Ultrason. Ferroelectr. Freq. Control*, 60(5):888–897, 2013.

[132] Todd Nicholas, Haixin Ke, and Lihong Wang. In-Place Clutter Reduction for Photoacoustic Imaging, 2014.

[133] Joël J. Niederhauser, Michael Jaeger, Robert Lemor, Peter Weber, and Martin Frenz. Combined ultrasound and optoacoustic system for real-time high-contrast vascular imaging in vivo. *IEEE Trans. Med. Imaging*, 24(4):436–440, 2005.

[134] Bornstein NM, Krajewski A, Lewis AJ, and Norris JW. Clinical significance of carotid plaque hemorrhage. *Arch. Neurol.*, 47(9):958–959, 1990.

[135] Jung-Taek Oh, Meng-Lin Li, Hao F. Zhang, Konstantin Maslov, George Stoica, and Lihong V. Wang. Three-dimensional imaging of skin melanoma in vivo by dual-wavelength photoacoustic microscopy. *J. Biomed. Opt.*, 11(3):034032, 2006.

[136] Ivan M Pelivanov, Sergej A Belov, Vladimir S Solomatin, Tanya D Khokhlova, and Aleksander A Karabutov. Direct opto-acoustic in vitro measurement of the spatial distribution of laser radiation in biological media. *Quantum Electron.*, 36(12):1089, 2006.

[137] Tigran Petrosyan, Maria Theodorou, Jeffrey Bamber, Martin Frenz, and Michael Jaeger. Fast scanning wide-field clutter elimination in epi-optoacoustic imaging using comb-LOVIT. In *IEEE Int. Ultrason. Symp.*, 2017.

[138] Adam Petschke and Patrick J. La Rivière. Comparison of intensity-modulated continuous-wave lasers with a chirped modulation frequency to pulsed lasers for photoacoustic imaging applications. *Biomed. Opt. Express*, 1(4):1188–1195, 2010.

[139] Jan-F. Pietschmann and Frank Wübbeling. Inverse und schlecht gestellte Probleme. Technical report, Westfaelische Wilhelms Universitaet Muenster, 2012.

[140] E. Pines and T. Cunningham. Dermatological photoacoustic spectroscopy. In R. Marks and P.A. Payne, editors, *Bioeng. Ski.*, pages 283–290. 1981.

[141] Behnaz Pourebrahimi, Sangpil Yoon, Dustin Dopsa, and Michael C. Kolios. Improving the quality of photoacoustic images using the short-lag spatial coherence imaging technique. In *Photons Plus Ultrasound Imaging Sens.*, volume 8581, page 85813Y, mar 2013.

[142] Scott Prahl. Optical Absorption of Hemoglobin, availible: http://omlc.ogi.edu/spectra/hemoglobin/summary.html, date accessed: 2017-12-20, 1999.

[143] Stefan Preisser, Gerrit Held, Hidayet G Akarçay, Michael Jaeger, and Martin Frenz. Study of clutter origin in in-vivo epi- optoacoustic imaging of human forearms. *J. Opt.*, 18(9):1–9, 2016.

[144] Ilona Rolfes. *Grundlagen der Hochfrequenztechnik*. Ruhr-Universität Bochum, 2011.

[145] Guy Rousseau, Jean-pierre Monchalin, Bruno Gauthier, and Alain Blouin. Non-contact biomedical photoacoustic and ultrasound imaging imaging. *J. Biomed. Opt.*, 17(6):061217–1–7, 2012.

[146] Malvin Carl Saleh, Bahaa E A and Teich. *Fundamentals of photonics; 2nd ed.* Wiley, New York, NY, 2007.

[147] Martin F Schiffner and Georg Schmitz. Plane Wave Pulse-Echo Ultrasound Diffraction Tomography With A Fixed Linear Transducer Array. *Acoust. Imaging*, 2012.

[148] Thomas Schmid. Photoacoustic spectroscopy for process analysis. *Anal. Bioanal. Chem.*, 384(5):1071–1086, 2006.

[149] Hans-Martin Schwab. *Nonlinear Reconstruction Techniques in Photoacoustic Imaging*. Master's thesis, Ruhr-Universität Bochum, 2013.

[150] Hans-Martin Schwab, Martin F Beckmann, and Georg Schmitz. Iterative Photoacoustic Reconstruction in Heterogeneous Media using the Kaczmarz Method. In *IEEE Int. Ultrason. Symp.*, pages 33–36, 2014.

[151] Hans-Martin Schwab, Martin F Beckmann, and Georg Schmitz. Photoacoustic Clutter Reduction using Plane Wave Ultrasound and a Linear Scatter Estimation Approach. In *Ultrason. Symp. (IUS), 2015 IEEE Int.*, 2015.

[152] Hans-Martin Schwab, Martin F. Beckmann, and Georg Schmitz. Photoacoustic clutter reduction by inversion of a linear scatter model using plane wave ultrasound measurements. *Biomed. Opt. Express*, 7(4):1468, 2016.

[153] Hans-Martin Schwab, Andreas Ihrig, Dominic Depke, Sven Hermann, and Michael Schäfers. Aberration Correction in Photoacoustic Imaging Using Paraxial Backpropagation. In *IEEE Int. Ultrason. Symp.*, 2017.

[154] Hans-Martin Schwab and Georg Schmitz. An Advanced Interpolation Approach for Photoacoustic Clutter Reduction Based on a Linear Plane Wave Scatter Model. In *Ultrason. Symp. (IUS), 2015 IEEE Int.*, volume 2016-Novem, pages 0–3, 2016.

[155] Jignesh Shah, Suhyun Park, Salavat Aglyamov, Timothy Larson, Li Ma, Konstantin Sokolov, Keith Johnston, Thomas Milner, and Stanislav Y. Emelianov. Photoacoustic imaging and temperature measurement for photothermal cancer therapy. *J. Biomed. Opt.*, 13(3):1–19, 2009.

[156] Yae-Lin Sheu and Pai-Chi Li. Photoacoustic Wave Propagation Simulations Using the Finite-Difference Time-Domain Method with Berenger's Perfectly Matched Layers. *J. Acoust. Soc. Am.*, 124(6), 20008.

[157] Markus W. Sigrist. Laser generation of acoustic waves in liquids and gases. *J. Appl. Phys.*, 60(7), 1986.

[158] Mithun K.A. Singh and Wiendelt Steenbergen. Photoacoustic-guided focused ultrasound (PAFUSion) for identifying reflection artifacts in photoacoustic imaging. *Photoacoustics*, 3(4):123–131, 2015.

[159] Mithun Kunil Ajith Singh. *Identification and elimination of reflection artifacts in biomedical photoacoustic imaging*. PhD thesis, University of Twente, 2016.

[160] Mithun Kunil Ajith Singh, Michael Jaeger, Martin Frenz, and Wiendelt Steenbergen. In vivo demonstration of reflection artifact reduction in photoacoustic imaging using synthetic aperture photoacoustic-guided

focused ultrasound (PAFUSion). *Biomed. Opt. Express*, 7(8):2955–2972, 2016.

[161] Kwang Hyun Song, Chulhong Kim, Konstantin Maslov, and Lihong V. Wang. Noninvasive in vivo spectroscopic nanorod-contrast photoacoustic mapping of sentinel lymph nodes. *Eur. J. Radiol.*, 70(2):227–231, may 2009.

[162] Willem M Star. Diffusion Theory of Light Transport. In Ashley J Welch and Martin J C Van Gemert, editors, *Opt. Response Laser-Irradiated Tissue*, pages 131–206. Springer US, Boston, MA, 1995.

[163] Plamen Stefanov and Gunther Uhlmann. Thermoacoustic tomography with variable sound speed. *Inverse Probl.*, 25(7):075011, jul 2009.

[164] Plamen Stefanov and Gunther Uhlmann. Instability of the linearized problem in multiwave tomography of recovery both the source and the speed. *ArXiv e-prints*, pages 1–11, 2012.

[165] Plamen Stefanov and Gunther Uhlmann. Recovery of a Source Term or a Speed with one Measurement and Applications. *Trans. Am. Math. Soc.*, 365(11):5737–5758, 2013.

[166] Ingo Stoffels, Stefan Morscher, Iris Helfrich, Uwe Hillen, Julia Leyh, Neal C Burton, Thomas C P Sardella, Jing Claussen, Thorsten D Poeppel, Hagen S Bachmann, Alexander Roesch, Klaus Griewank, Dirk Schadendorf, Matthias Gunzer, and Joachim Klode. Metastatic status of sentinel lymph nodes in melanoma determined noninvasively with multispectral optoacoustic imaging. *Sci. Transl. Med.*, 7(317):317ra199—-317ra199, 2015.

[167] Yixiong Su, Fan Zhang, Kexin Xu, Jianquan Yao, and Ruikang K Wang. A photoacoustic tomography system for imaging of biological tissues. *J. Phys. D. Appl. Phys.*, 38(15):2640, 2005.

[168] Thomas L. Szabo. *Diagnostic ultrasound imaging: inside out*. Elsevier Academic Press, 2014.

[169] Sergey Telenkov, Andreas Mandelis, Bahman Lashkari, and Michael Forcht. Frequency-domain photothermoacoustics: Alternative imaging modality of biological tissues. *J. Appl. Phys.*, 105(10), 2009.

[170] Chao Tian, Zhixing Xie, Mario L Fabiilli, Shengchun Liu, Cheng Wang, Qian Cheng, and Xueding Wang. Dual-pulse nonlinear photoacoustic technique: a practical investigation. *Biomed. Opt. Express*, 6(8):2923–2933, 2015.

[171] Chao Tian, Zhixing Xie, Mario L. Fabiilli, and Xueding Wang. Imaging and sensing based on dual-pulse nonlinear photoacoustic contrast: a preliminary study on fatty liver. *Opt. Lett.*, 40(10):2253, 2015.

[172] B. E. Treeby and B. T. Cox. K-wave User Manual - A MATLAB toolbox for the time domain simulation of acoustic wave fields. Technical report, University College London, 2012.

[173] B. E. Treeby, E Zhang, and B. T. Cox. Photoacoustic tomography in absorbing acoustic media using time reversal. *Inverse Probl.*, 26(11):115003, nov 2010.

[174] Paul Kumar Upputuri and Manojit Pramanik. Performance characterization of low-cost , high- speed , portable pulsed laser diode photoacoustic tomography (PLD-PAT) system. *Biomed. Opt. Express*, 6(10):4118–4129, 2015.

[175] Peter van Es, Samir K Biswas, Hein J Bernelot Moens, Wiendelt Steenbergen, and Srirang Manohar. Initial results of finger imaging using photoacoustic computed tomography. *J. Biomed. Opt.*, 19(6):60501, 2014.

[176] M. L. Veingerov. An optical method of gas analysis. *Nature*, 158:28–29, 1946.

[177] Lihong V. Wang. *Photoacoustic Imaging and Spectroscopy*. Taylor & Francis Group, LLC, 2009.

[178] Lihong V. Wang and Hsin-i Wu. *Biomedical Optics*. John Wiley & Sons, 2007.

[179] Tianren Wang and Yun Jing. A fast marching method based back projection algorithm for photoacoustic tomography in heterogeneous media. *ArXiv e-prints*, 27695:1–10, 2015.

[180] Xueding Wang, Geng Ku, Malgorzata A Wegiel, Darryl J Bornhop, George Stoica, and Lihong V Wang. Noninvasive photoacoustic angiography of

animal brains in vivo with near-infrared light and an optical contrast agent. *Opt. Lett.*, 29(7):730–732, apr 2004.

[181] Ashley J. Welch and Martin J.C. van Gemert, editors. *Optical-Thermal Response of Laser-Irradiated Tissue*, volume 1. Springer, 2015.

[182] Jun Xia, Chao Huang, Konstantin Maslov, Mark A. Anastasio, and Lihong V. Wang. Enhancement of photoacoustic tomography by ultrasonic computed tomography based on optical excitation of elements of a full-ring transducer array. *Opt. Lett.*, 38(16):3140–3143, 2013.

[183] Jiaying Xiao, Lei Yao, Yao Sun, Eric S Sobel, Jishan He, and Huabei Jiang. Quantitative two-dimensional photoacoustic tomography of osteoarthritis in the finger joints. *Opt. Express*, 18(14):14359–14365, jul 2010.

[184] Guan Xu, Justin R Rajian, Gandikota Girish, Mariana J Kaplan, J Brian Fowlkes, Paul L Carson, and Xueding Wang. Photoacoustic and ultrasound dual-modality imaging of human peripheral joints. *J. Biomed. Opt.*, 18(1):10502, 2012.

[185] Minghua Xu and Lihong Wang. Universal back-projection algorithm for photoacoustic computed tomography. *Phys. Rev. E*, 71(1):016706, jan 2005.

[186] Minghua Xu and Lihong V Wang. Photoacoustic imaging in biomedicine. *Rev. Sci. Instrum.*, 77(4):041101, 2006.

[187] Yuan Xu, Dazi Feng, and L.V. Wang. Exact frequency-domain reconstruction for thermoacoustic tomography. I. Planar geometry. *IEEE Trans. Med. Imaging*, 21(7):823–828, jul 2002.

[188] Yuan Xu and Lihong V. Wang. Time Reversal and Its Application to Tomography with Diffracting Sources. *Phys. Rev. Lett.*, 92(3):4, 2004.

[189] Junjie Yao, Lidai Wang, Joon-Mo Yang, Konstantin I Maslov, Terence T W Wong, Lei Li, Chih-Hsien Huang, Jun Zou, and Lihong V Wang. High-speed label-free functional photoacoustic microscopy of mouse brain in action. *Nat. Methods*, 12(5):407–410, 2015.

[190] Junjie Yao and Lihong V. Wang. Photoacoustic Microscopy. *Laser Photon. Rev.*, 7(5):1–36, 2013.

[191] Changhan Yoon, Jeeun Kang, Seunghee Han, Yangmo Yoo, Tai-Kyong Song, and Jin Ho Chang. Enhancement of photoacoustic image quality by sound speed correction: ex vivo evaluation. *Opt. Express*, 20(3):3082, 2012.

[192] Xu Yuan and V Wang Likong. Effects of Acoustic Heterogeneity in Breast Themoacoustic Tomography. *IEEE Trans. Ultrason. Ferroelectr. Freq. Control*, 50(9):1134–1146, 2003.

[193] Z. Yuan and H. Jiang. Quantitative photoacoustic tomography. *Philos. Trans. R. Soc.*, 367:3043–3054, 2009.

[194] Zhen Yuan, Qizhi Zhang, and Huabei Jiang. Simultaneous reconstruction of acoustic and optical properties of heterogeneous media by quantitative photoacoustic tomography. *Opt. Express*, 14(15):6749–6754, 2006.

[195] Roger J Zemp, Liang Song, Rachel Bitton, K Kirk Shung, and Lihong V Wang. Realtime photoacoustic microscopy in vivo with a 30-MHz ultrasound array transducer. *Opt. Express*, 16(11):7915–7928, 2008.

[196] Chi Zhang and Yuanyuan Wang. A reconstruction algorithm for thermoacoustic tomography with compensation for acoustic speed heterogeneity. *Phys. Med. Biol.*, 53(18):4971, 2008.

[197] Hao F. Zhang, Carmen A. Puliafito, and Shuliang Jiao. Photoacoustic Ophthalmoscopy for In Vivo Retinal Imaging: Current Status and Prospects. *Ophthalmic Surg Lasers Imaging*, 42(0):106–115, 2011.

[198] Jin Zhang, Kun Wang, Yongyi Yang, and Mark a. Anastasio. Simultaneous reconstruction of speed-of-sound and optical absorption properties in photoacoustic tomography via a time-domain iterative algorithm. In Alexander A. Oraevsky and Lihong V. Wang, editors, *Photons Plus Ultrasound Imaging Sens. 2008*, volume 6856, pages 68561F–68561F–8, feb 2008.